

75134065

LIDRARY Michigan State University



This is to certify that the

dissertation entitled

X-RAY STUDIES OF LAYER RIGIDITY AND C-AXIS EXPANSION IN INTERCALATED LAYERED SOLIDS

Soonil Lee

presented by

has been accepted towards fulfillment of the requirements for

Ph.D. degree in Physics

Date July 12, 1989

MSU is an Affirmative Action/Equal Opportunity Institution

0-12771

PLACE IN RETURN BOX to remove this checkout from your record. TO AVOID FINES return on or before date due.

DATE DUE	DATE DUE	DATE DUE

MSU Is An Affirmative Action/Equal Opportunity Institution

X-RAY STUDIES OF LAYER RIGIDITY AND C-AXIS EXPANSION IN INTERCALATED LAYERED SOLIDS

Ву

Soonil Lee

A DISSERTATION

Submitted to

Michigan State University

in partial fulfillment of the requirements

for the degree of

DOCTOR OF PHILOSOPHY

Department of Physics and astronomy

	!
	1

ABSTRACT

X-RAY STUDIES OF LAYER RIGIDITY AND C-AXIS EXPANSION
IN INTERCALATED LAYERED SOLIDS

By

Soonil Lee

From X-ray diffraction and Raman active torsional mode frequency studies the new synthetic vermiculite intercalation compounds, $[(CH_3)_4N^+]_{\mathbf{x}} [(CH_3)_3NH^+]_{1-\mathbf{x}} - Vm, \text{ are determined to have a solid solution type mixed gallery cation distribution.}$

The x dependence of the normalized basal spacing, $d_n(x)$, of ternary pillared vermiculite $[(CH_3)_4N^+]_x[(CH_3)_3NH^+]_{1-x}$ -Vm has been measured and compared with that of Cs_xRb_{1-x} -Vm. Both system exhibit a nonlinear $d_n(X)$ with approximate thresholds of x = 0.2 and 0.5, respectively. A model which relates $d_n(x)$ to layer rigidity and the binding energies of gallery and defect sites yields excellent fits to the basal spacing data and to monolayer simulations if collective effects are included.

We also have constructed a plot of the normalized basal spacing versus normalized torsional mode frequency for two vermiculite intercalation compounds, $\operatorname{Cs_{x}Rb_{1-x}}\text{-Vm}$ and $[(\operatorname{CH_{3}})_{4}\operatorname{N}^{+}]_{x}[(\operatorname{CH_{3}})_{3}\operatorname{NH}^{+}]_{1-x}\text{-Vm}$. This plot shows a striking "scaling-like" behavior for the two different mixed-ion systems. An attempt to understand this behavior based on the virtual crystal approximation has been made. This mode calculation

reveals a very close relationship between the basal spacing and the gallery ion-oxygen interaction.

A layer rigidity model which includes the effects of elastic deformation of the host layers is applied to a variety of layered intercalation compounds. This model can account for the composition dependence of the c-axis expansion of the three classes of layered solids. Rigidity parameters deduced from this model for each of the three classes of layered solid are reflective of structurally derived rigidity as are the healing lengths computed on the basis of discrete and continuum analyses.

Using the continuum elastic theory the attractive intralayer interaction in intercalation compounds is calculated to show the contribution of each rigidity constant and the size dependence of the intercalants. Different staging behavior among different intercalated layered solids is discussed using Safran's phase diagram.

We have constructed a novel Low Temperature X-Ray Diffraction (LTXRD) system which can be used to study the temperature dependent properties of solids (i.e. temperature dependent basal spacing variation). A closed cycle He-cryostat and 4-circle diffractometer have been modified. Instead of moving the whole cryostat to locate the sample at the center of the diffractometer as is usually done we employ a small goniometer inside of the cryostat for easy and accurate sample alignment and scanning. The combination of two small universal joints and square cross section sliding shafts makes it possible to control the inside goniometer from outside the cryostat. Use of a Kapton window allows us to visualize the inside sample and to reduce the X-ray absorption by the window.

ACKNOVLEDGMENT

With great pleasure I acknowledge my adviser Professor Stuart A. Solin for his invaluable help throughout this research. From numerous discussions and helpful criticism I have learned how to think through physics problems and refine rough ideas. His enthusiasm and intuition have been inspirational. Also I am very grateful for his hospitality to my family.

It is a pleasure to acknowledge Professor S. D. Mahanti. He has taught me much about solid state physics and statistical mechanics. He was also kind enough to answer my endless questions and he showed how to appreciate fine points in many problems.

I have greatly benefited from my collaboration with Professor H. Miyazaki in the late stage of this research. He gave me working knowledge of intercalation compounds including the staging transition and the continuum elastic theory.

Collaboration with Professor T. J. Pinnavaia and H. Kim has been a wonderful experience. In numerous cases they have guided us with solid chemistry.

Thanks are due to my fellow students. J. Wei has been a valuable collaborator. I enjoyed many interesting discussion with him. C. Huang, Y. B. Fan, X. W. Qian, T. Park and P. Zhou are appreciated for their assistance and for useful discussions. There are many others whom I cannot mention one by one.

Finally, I sincerely thank my family. My parents, brother and sister all supported me during my studies. My special thanks go to my wife and daughter who endured many hard and lonely days.

TABLE OF CONTENTS

Chapter	I.	Overview1
Chapter	II.	Structure of vermiculite13
Chapter	III.	Layer rigidity and collective effects in vermiculite
		pillared by mixed-alkyl ammonium ions18
	III.1	Introduction18
	III.2	Experiment and results20
	III.3	Discussion35
	III.4	Summary and concluding remarks60
Chapter	IV.	Elastic effects in intercalated layered compounds63
	IV.1	Introduction
	IV.2	Composition dependent C-axis expansion70
	IV.3	Layer rigidity and staging83
	IV.4	Summary and concluding remarks88
Chapter	v.	A variable-temperature X-ray cryostat with an
		externally adjustable internal goniometer90
	V.1	Introduction90
	V.2	Apparatus92
	V.3	Experiment97
List of	referen	nces102
Appendio	ces	

LIST OF TABLES

<u>Table</u>		Page
III.1	Intercalant size effect on encapsulation	32
IV.1	Important parameters for several ternary layered	
	intercalation compounds	74
IV.2	Four types of basal spacing variation of layered	
	solids	75
V.1	Basal spacing of HOPG as a function of temperature	99

LIST OF FIGURES

<u>Figure</u>		Page
1.1	Three classes of layered solids	3
I.2	Illustration of staging phenomenon	5
I.3	(00L) X-ray pattern and rocking-curve of vermiculite	7
I.4	The transverse layer distortions and corresponding	
	basal spacing variations	9
1.5	Four functional forms of basal spacing variations	11
II.1	Structure of 2:1 layered silicate	14
II.2	The Kagome lattice of oxygen atoms	16
II.3	Schematic view of the basal plane distortion	17
III.1	Torsional mode eigenvector	21
III.2	Room-temperature (00L) x-ray diffraction patterns	
	of [(CH ₃) ₄ N ⁺] _x [(CH ₃) ₃ NH ⁺] _{1-x} -Vm	24
III.3	A rocking curve and a Q-plot of	
	[(CH ₃) ₄ N ⁺] _x [(CH ₃) ₃ NH ⁺] _{1-x} -Vm	25
III.4	The composition dependence of the normalized	
	basal spacing	27
111.5	The composition dependence of the Raman frequency	
	of the torsional mode shown together with $d_n(x)$	29
III.6	Schematic illustration of encapsulation	30
III.7	The normalized torsional mode frequency vs. d_n	34
III.8	A schematic diagram for a (OOL) scan	37
III.9	A plot of the relative intensity	38

III.10	A comparison of the observed (00L) reflections with	
	computer generated reflections for	
	[(CH ₃) ₄ N ⁺] _{.63} [(CH ₃) ₃ NH ⁺] _{.37} -Vm	42
III.11	The computer generated Hendricks-Teller X-ray	
	diffraction patterns	43
III.12	A patterson synthesis	46
III.13	The composition dependence of FWHM and $L_{_{\hbox{\scriptsize C}}}$	47
III.14	Monolayer triangular lattice computer simulations of	
	the normalized basal spacing	50
III.15	A bright-field scanning-tunneling electron micrograph	
	of [(CH ₃) ₃ NH ⁺]-Vm	52
III.16	The gallery concentration, x_g , versus x	54
III.17	The configuration of the host layer and guest ions	58
III.18	The normalized values of A_{M-O} versus $\mathbf{x}_{\mathbf{g}}$	61
IV.1	Safran's phase diagram as a function of T and x	66
IV.2	The rigid layer model used by Dahn et al.	68
IV.3	The normalized basal spacing versus x	71
IV.4	The ζ dependence of $Z(\zeta)$	78
IV.5	The phonon dispersion of pyrolytic graphite	79
IV.6	The normalized basal spacing vs. composition for	
	$Va_{1-x}(R_2)KC_{24}$ where R = H or D	82
IV.7	Attractive intralayer interaction and repulsive	
	interlayer interaction from an elastic origin	85
V.1	An overall view of the LTXRD system	93
V.2	An cut-away view of the home-made interconnection parts	94
V.3	Thermal expansion of HOPG	100

I. Overview

The term intercalation describes the reversible insertion of guest species into a host structure with maintenance of the structural features of the host. Even though the term can equally be applied to one- and three-dimensional solids, it is usually applied to lamellar solids because of their intrinsic anisotropy. For example in graphite carbon atoms are covalently bonded into a hexagonal lattice plane with a carbon-carbon distance of 1.42Å, and the carbon planes are then bound by the Van der Walls interaction with an interplane distance of 3.35Å along the c-axis. The weak Van der Walls bond can be easily broken by charge transfer to or from the graphite carbon layer with the resultant formation of the so called graphite intercalation compounds (GIC's). 2,3

Layered intercalation compounds have been the subjects of much historical and current interest among scientists in many varied disciplines. The origin of the intense interest is twofold; layered solids provide a natural arena for the exploration of quasi-two-dimensional physical phenomena, yet they also exhibit properties which are of significant practical value. Two dimensional (2D) melting, the 2D metal-insulator transition, binary alloy formation in 2D, anisotropic order-disorder phenomena, and unusual phase transitions and composition dependent unit cell volume changes are a few examples of the topics studied using layered intercalation compounds. Among the practical applications of layered intercalation compounds are hydrogen storage, batteries and catalysis, which have been studied widely. Recent advances in the intercalation chemistry of pillared clays have lead to the realization that these materials are the most promising precursors to new families of microporous adsorbents

and shape selective catalysts since the advent of synthetic Zeolites several decades ago.

There are a vast number of layered solids which exhibit a high degree of anisotropy in their physical properties and for which the interaction forces within layers of atoms are much stronger than the forces between layers. 2,12 There are several ways these layered materials can be classified but it is most convenient to classify such materials qualitatively according to the rigidity of their layers with respect to distortions involving atomic displacements transverse to the layer plane. Such a classification scheme is shown in Figure I.1 (a) which depicts schematically the three general classes. 13 Class I contains only two compounds, graphite and boron nitride, which are the only layered solids that are composed of monatomically thin planes of atoms. As a result of this unusual structure, the individual layers of class I solids are "floppy" and can easily sustain long wavelength deformation which are transverse to the layer planes. Examples of class II materials are layer dichalcogenides such as TiS, and HfS, FeOCl-type compounds and metal chlorides such as FeCl, and CoCl, etc. 14 The layers in class II materials are often composed of three distinct planes of strongly bonded atoms and present a stiffer structure than the layers of class I solids. Therefore they are more resistive to transverse distortions. The prototypical examples of class III materials are the layered silicate clays 15 (e.g. Vermiculite). Because the clay layers can be many atoms thick (Vermiculite has seven atomic-plane thick layers), they will be quite "rigid" against transverse layer distortions. In fact the clay layers are so rigid that they can be propped apart or pillared by widely-spaced intercalants without sagging. 11

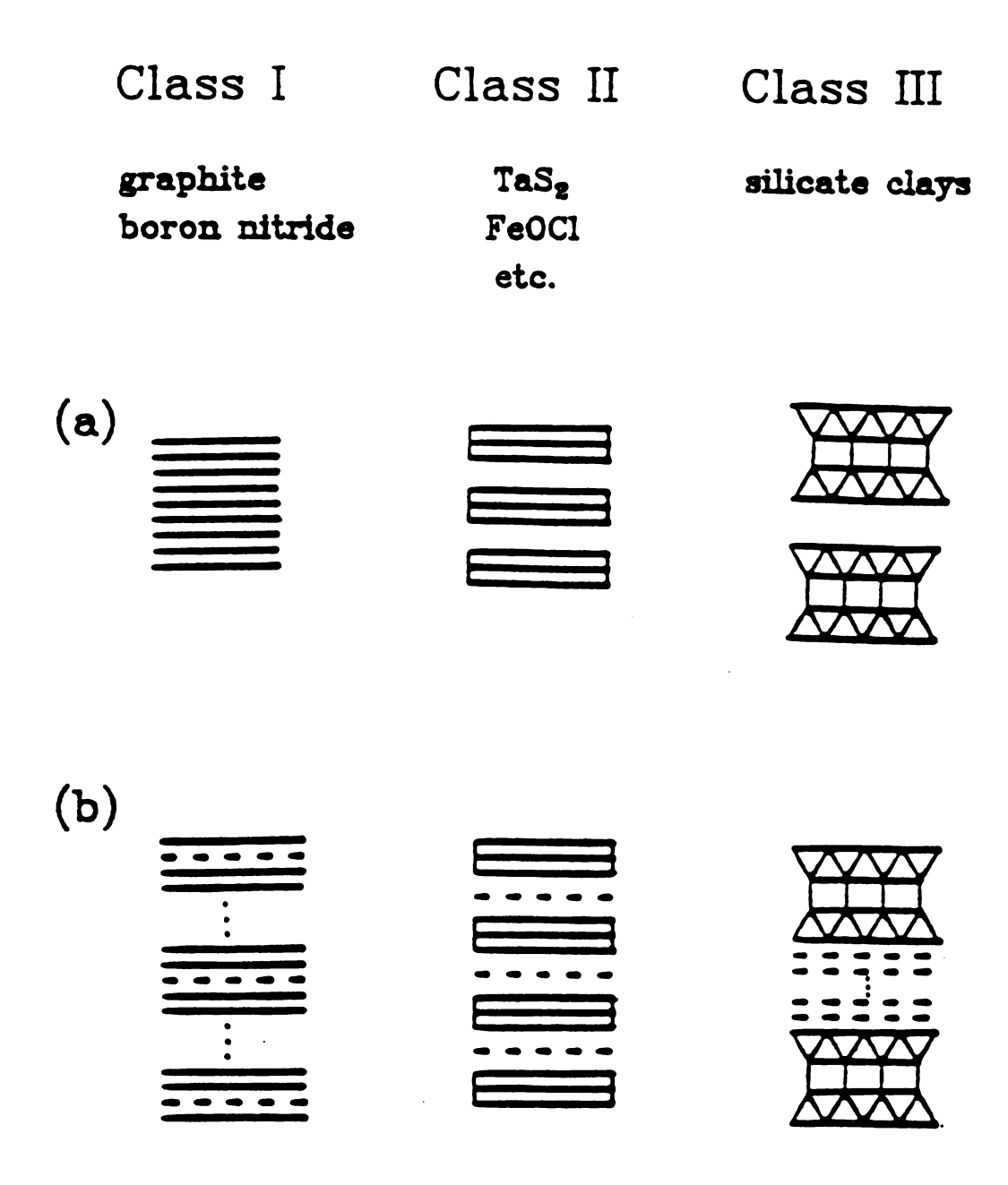


Figure I.1 Schematic classifications of (a) pristine layered solids and (b) the intercalated forms of (a). In (b) the dashed (solid) lines represent guest (host) layers.

A wide variety of physical properties seen in lamellar solids are in large part determined by the transverse rigidity of the host layers. For example, graphite whose monatomic layers are "floppy" does not form gel structures in any liquid while layered alumino-silicates whose multi-atomic layers are "rigid" are excellent gel formers. 16 One of the most interesting phenomena observed in intercalation compounds is the existence of a long-period one dimensional modulated structure along the c-axis, namely staging. The staging phenomena is characterized by a stage number n which refers to the number of host layers separating two adjacent intercalant layers as shown in Figure I.2. In Figure I.1 (b) are illustrated typical staging behavior for each class of layered solids. The class I layered solids and particularly graphite intercalation compounds exhibit many different stages including high stages up to n = 10.3

Note that class I graphite intercalation compounds contain as their key identifying feature multilayers of host between monolayers of guest. In class II, certain intercalation compounds of transition metal dichalcogenides have been shown to form low stages 17,18,53,54 (mostly stage 1 and 2). In class III, compounds such as vermiculite have been found only in a stage 1 state. However clay intercalation compounds have the unique ability to sustain multilayers of guest between monolayers of host. 13 It is currently understood 19 that the competition between repulsive interplanar interactions and attractive intraplanar interactions is responsible for staging. However because elastic interactions in addition to the long-range electrostatic interactions contribute to the interatomic forces, 19,20 one can expect to understand quite distinctive staging behavior among these three different classes

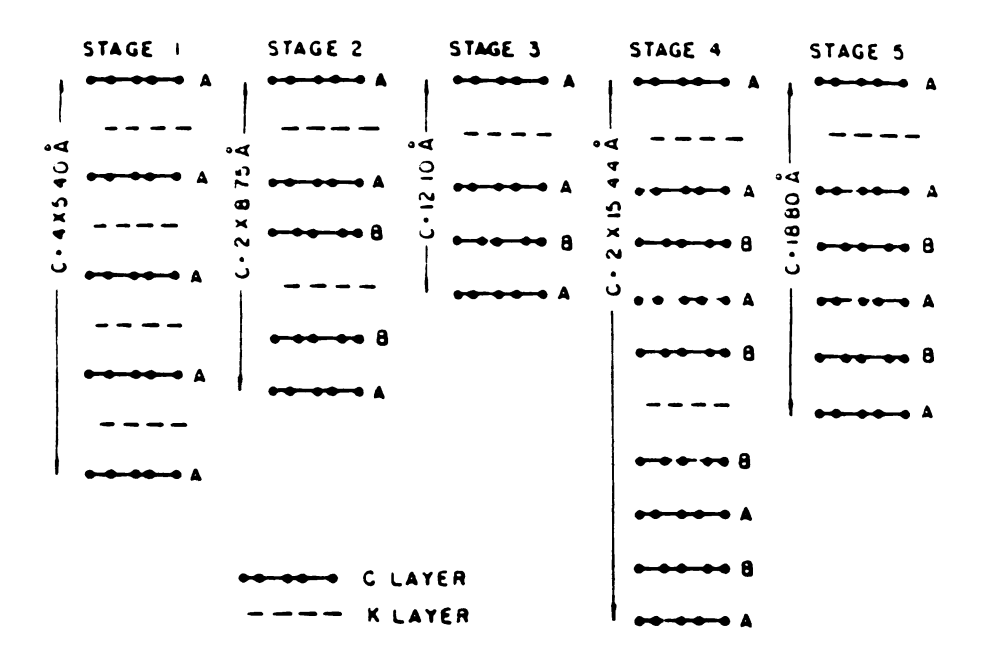


Figure I.2 Schematic diagram illustrating the staging phenomenon in graphite-potassium compounds for stages 1-5. Dashed and solid lines represent, respectively, the potassium layers and the carbon layers.

of layered solids only after the layer rigidity of these materials is understood.

While the physics of type I and type II materials, especially graphite and graphite intercalation compounds has been and continues to be heavily studied by many researchers, 2,18 the physics of class III materials, layered silicate clays and clay intercalation compounds has, to date, received less attention. However if we are to develop a sound understanding of layered solids, this major extreme subclass cannot be ignored. Much of the reason that hindered the solid state physics community from extending its horizon to the class III material lies in the common misconception about clay. The very name of clay reminds most solid state physicists of something very messy and disordered. But it is well known to inorganic chemists, soil scientists, geologists, and mineralogists that some clays actually have a very well defined structure. The structure is so well defined that it has been used to study a particular type of stacking sequence disorder known as interstratification which is an intrinsically interesting phenomena. 15,21

As an example of the excellent crystalline form of some clay, the (00L) X-ray diffraction pattern of vermiculite is shown in Figure I.3 together with its mosaic spread and a schematic diagram of its stacking structure. The reflections shown have widths which are instrument-resolution-limited, and correspond to c-axis correlation ranges in excess of 5000Å. Of equal importance to the study of physical phenomena in clay intercalation compounds is the mosaic spread in the degree of alignment of the crystalline c-axes. The rocking curve shown in Figure I. 3 indicates a mosaic spread of approximately 5° which is considerably higher than that of highly oriented pyrolytic graphite

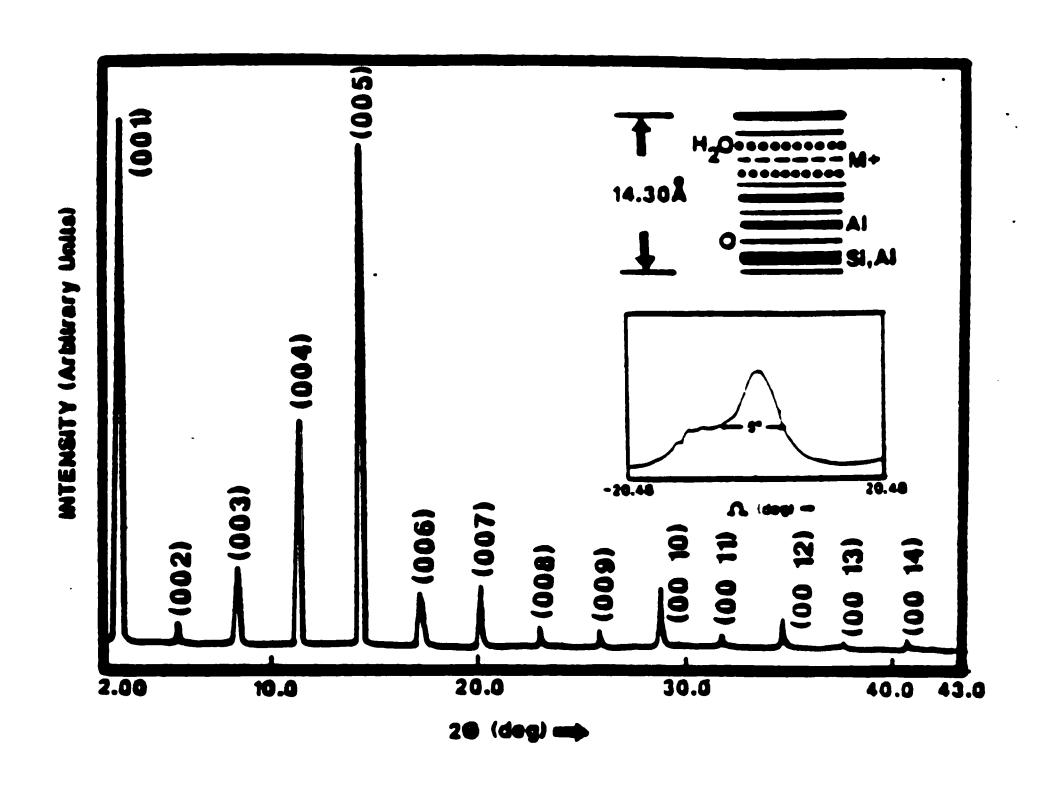


Figure 3. Room temperature (00L) X-ray diffraction pattern of vermiculite recorded using Mo Kα radiation. Inset shows rocking-curve of the (007) reflection. The diagram at the upper right of the figure represents the c-axis structure.

(HOPG)²³ but comparable to that of graphoil²⁴ a material with which much excellent solid-state physics has been carried out.²⁵

X-ray diffraction is a very suitable tool for the study of intercalated lamellar solids. First, if there are any structural phase transitions, such as implane melting of the intercalant layers or staging transitions between them which involves a long range c-axis modulation, they can be very easily observed either by implane scattering or by (00L) scattering, 2,3 respectively. Second, we can study the layer rigidity of the host layered solids from measurements of the basal spacing d (= unit-cell length along the c-axis) of the intercalated layered solids with 2D homogeneous solid solution type intercalants.

As an example of the latter consider the mixed ion layered solids of the type $M_{1-x}M'_{x}L$, $0 \le x \le 1$ where M and M' represent cations of different size and L represents the host layers, for example Vermiculite(= Vm) or Graphite(= C). If we adopt the simplified model in which the graphite layers are very floppy with respect to transverse distortions while the vermiculite layers are infinitely rigid, as illustrated in Figure I.4, then the composition dependence d(x) vs x of the X-ray derived basal plane spacing of the layers would have the functional form shown in that Figure. The non-Vegard's law 56,27,30 (i.e. non linear) form of d(x) for graphite is a consequence of the limited ability of the carbon layers to wrap or pucker around the large ion in the gallery. In contrast the step-function-like behavior which would be predicted for d(x) in the vermiculite case reflects the assumption that as few as three noncolinear large ions could fully prop the clay layers apart if they were infinitely rigid. The super-linear basal spacing variation observed in graphite intercalation compounds is the most

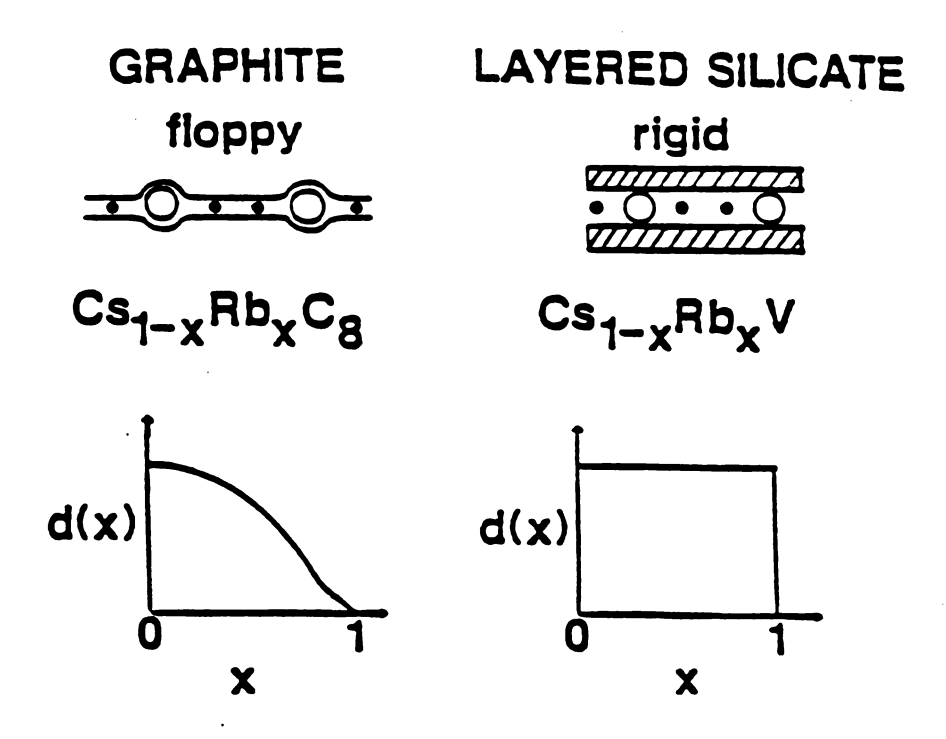


Figure I.4 Schematic illustration of the transverse layer distortions in the mixed layer intercalation compounds Cs-Rb-graphite, the layers of which are "floppy" and Cs-Rb-vermiculite, the layer of which are "rigid". Also shown are the composition dependences of the corresponding basal spacings, d(x) vs x.

common in intercalated layered compounds and it can serve as a starting point for the understanding of various basal spacing composition dependencies. 26 For example, a linear basal spacing variation (so called Vegard's law) and step function variations can be interpreted as two limiting cases of a super-linear basal spacing variation. 27 Also it becomes possible to quantify layer rigidity from the experimentally measured basal spacing after the super-linear basal spacing variation due to local deformation is studied. 26 Real systems are more complicated than these simplified pictures and in many cases sigmoidal shaped basal spacing variations have been observed. 27,30 The understanding of the sigmoidal shape basal spacing variations requires more than a simple monolayer model. 27 Also one can imagine sublinear basal spacing variations to complete the list of possible functional forms of basal spacing variations, but this hasn't been observed yet. The four types of basal spacing variations are illustrated in Figure I.5.

Finally the study of class III vermiculite intercalation compound can be very useful for the following reasons. First because it belongs to the important extreme subclass of layered solids 13 with "rigid" layers we can gain a global understanding of lamellar solids in general from a comparison of Vermiculite with graphite intercalation compounds and transition metal dichalcogenide compounds. Second only class III materials have a fixed layer charge density 15,21 that does not vary during intercalation (More appropriately called ion exchange). This allows us to concentrate mainly on the elastic effects. In contrast graphite is amphoteric and the physical properties of its intercalation compounds are greatly influenced by the charge transfer from and to the carbon layers. 2,3 Third in the vermiculite intercalation compounds there is a particularly revealing Raman active torsional mode due to the

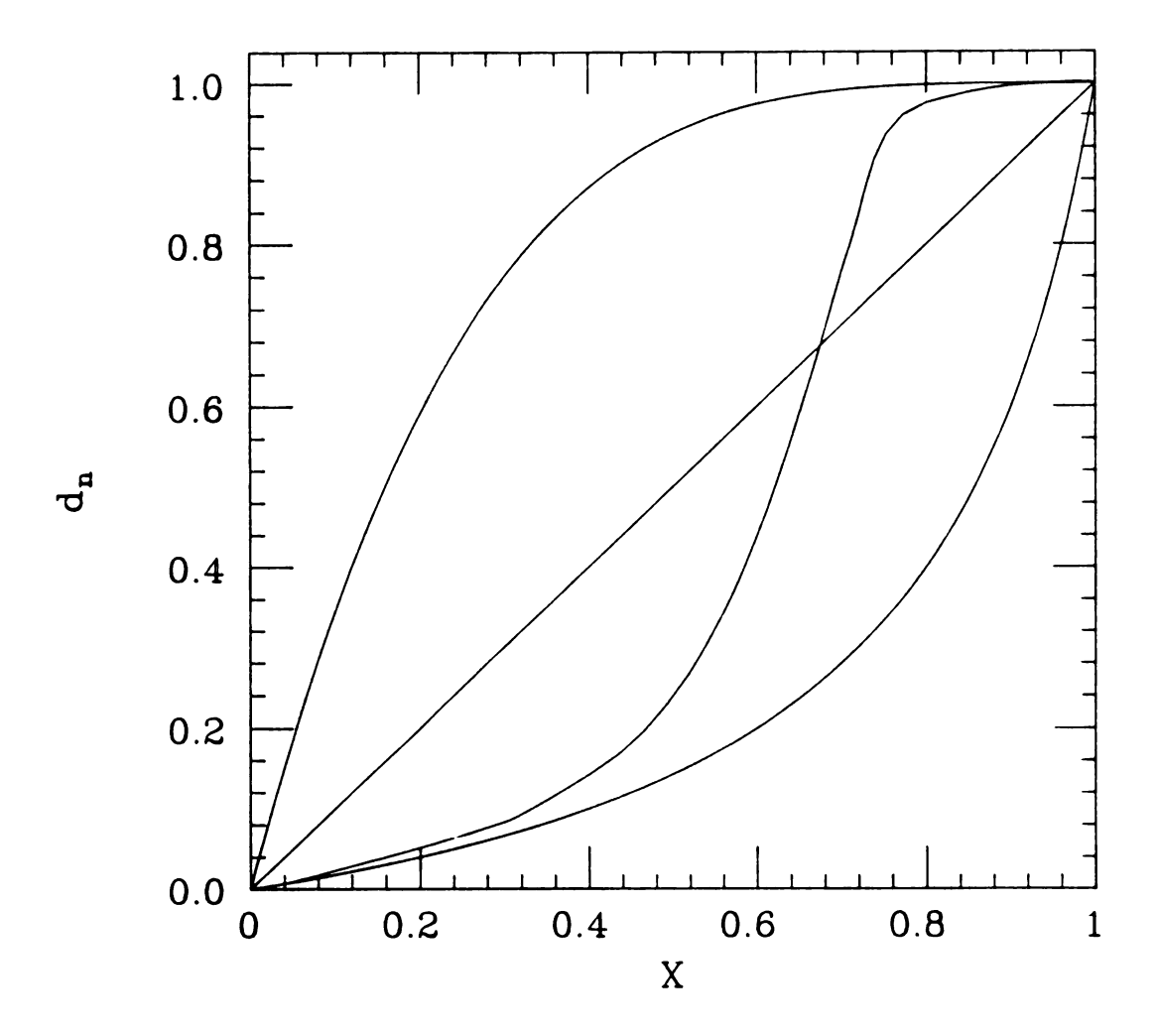


Figure I.5 Four functional forms of basal spacing variation in intercalated layered solids. Superlinear, linear (Vegard's law), sigmoidal, and sublinear variations, top to bottom, respectively.

interaction between the intercalant and the terminating oxygen plane. 29,30 This mode enables us to have insight into the guest-guest and guest-host interactions in clay intercalation compounds. Fourth, an understanding of the clay layer rigidity can lead to the improved synthesis of pillared clays. 11,16 Pillared clays are a recently developed class of microporous compounds with novel properties as shape-selective adsorbents and catalysts. The distinguishing feature of pillared clays is that the gallery cations are robust three-dimensional species which function in the water free interlayer space as molecular props. These props pillar the silicate layers and prevent their collapse in the absence of a swelling solvent. Because the silicate layers are not infinitely rigid, there must be some limit beyond which increasing pillar separation causes layer distortions akin to "sagging". Hence the synthetic design of pillared clay sorbents and catalysts could be greatly stimulated by the predictive power of a quantitative layer rigidity model.

II. Structure of Vermiculite

The building blocks of clay structures 15,21 are MO₄ tetrahedra and M'O₆ octahedra where M is most commonly Si⁴⁺ and occasionally Al³⁺ or Fe³⁺ and M' is a metal ion such as Al³⁺,Fe³⁺,Mg²⁺ or Li⁺. Also a number of the oxygen atoms in the M'O₆ building blocks are frequently replaced by hydroxyl groups. The replacement of oxygen by hydroxyl in the MO₄ building blocks occurs only rarely. The lamellar structure of clay minerals in general is a manifestation of the ability of MO₄ units and M'O₆ units to form tetrahedral and octahedral sheets respectively, and the ability of these sheets to link through a common oxygen plane to form layers.

Vermiculite is a specific example of a trioctahedral 2:1 layered silicate. 15,21 Its layers are formed from a sheet of edge connected octahedra which is symmetrically bound to two sheets of corner connected tetrahedra, thereby the name 2:1, as shown in Figure II.1. Unlike talc 21 in which the total positive charge of the tetrahedral and octahedral cations is exactly balanced by the total anion charge of the 0_{20} (OH) 4 framework, vermiculite bears some amount of net negative charges on the layer that results from the isomorphic substitutions of the cations by other lower charged cations. For example, the Si4+ ion of the tetrahedral sheet is often replaced by Al3+. The charge density of vermiculite is between 1.2e - 1.8e per unit formula. This net negative charge of the clay layer is balanced by the gallery cations which are Mg 2+ in natural Llano vermiculite. Note that unlike graphite which is amphoteric, the clay layers have a fixed negative charge, and the intercalation process in these compounds is equivalent to ion exchange and does not involve charge transfer between the guest and host species.

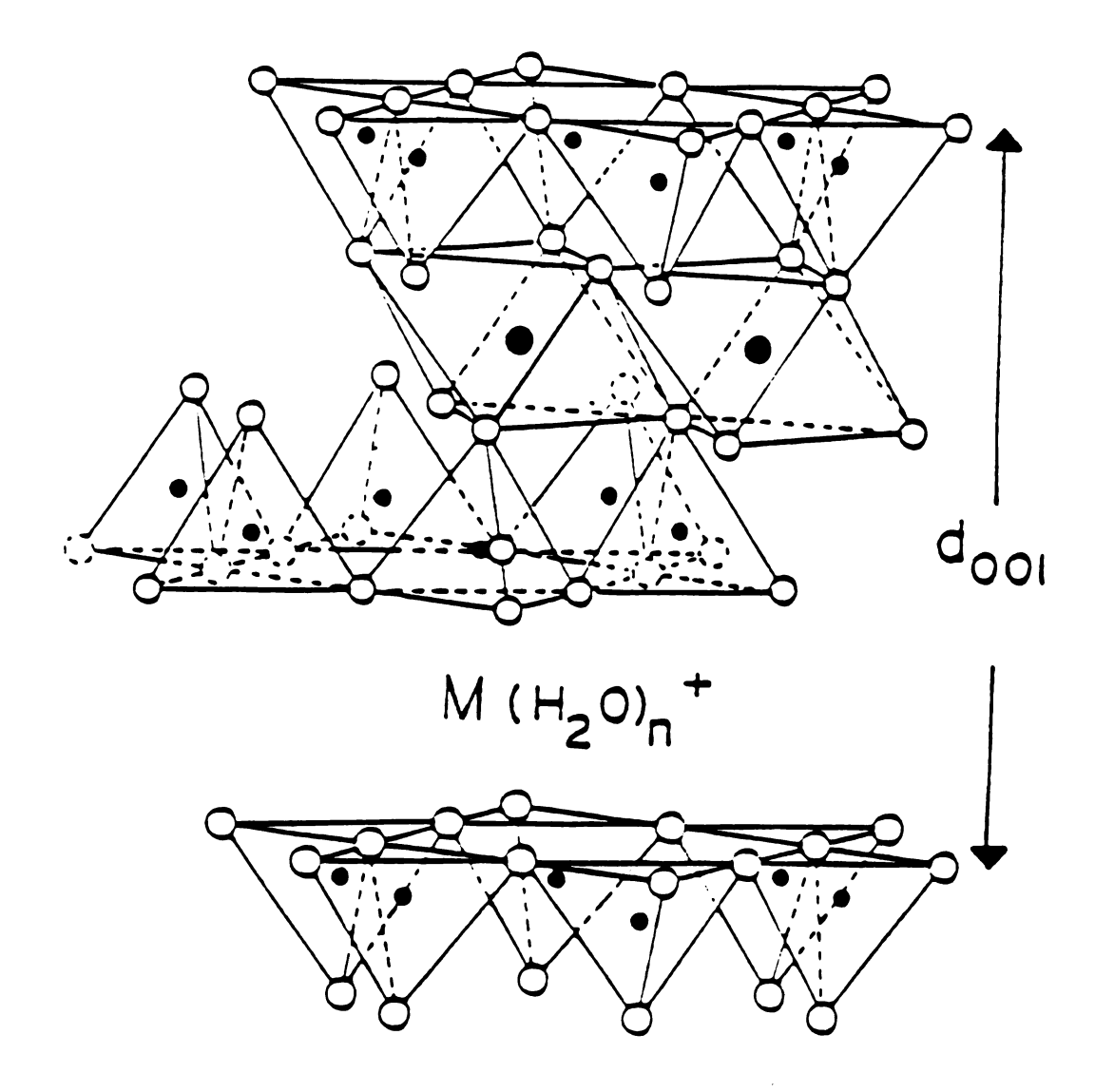


Figure II.1 Schematic illustration of the tetrahedral and octahedral sites in a 2:1 layered silicate. Open circles are oxygen, closed circles are cations in tetrahedral (Si, Al) and octahedral (Al, Fe, Mg, Li) positions. Hydroxyl groups (not distinguished from oxygen in the figure) are located in the second and third basal planes of oxygens.

The layers of oxygen atoms which terminate the clay layers are arranged in a Kagome lattice (See Figure II.2) whose hexagonal pockets form a triangular lattice of gallery sites that are occupied by guest cations. There are two gallery sites (hexagonal pockets) and almost two equivalents of charge per $O_{20}(OH)_4$ unit cell in vermiculite. This means that when the interlayer Mg^{2+} ions of the pristine compound are replaced by monovalent cations, every hexagonal cavity is occupied. This stoichiometric relationship forces the triangular lattice defined by the monovalent exchange cations to be commensurate with the lattice of the oxygen layers.

If the tetrahedral and octahedral sheets in typical clays were separated, the sheets would not have identical in-plane oxygen to oxygen distances. This mismatch in the common oxygen oxygen plane is accommodated in the 2:1 layer structure by alternating clockwise and counter-clockwise rotations of adjacent tetrahedra within the tetrahedral sheets. ²¹ This rotation is illustrated in Figure II.3, where arrows indicate the direction of rotation. The rotation angle, α , can depend on the interlayer cation and these effects can show up in the cation concentration dependence of the basal spacing and of the torsional mode frequency.

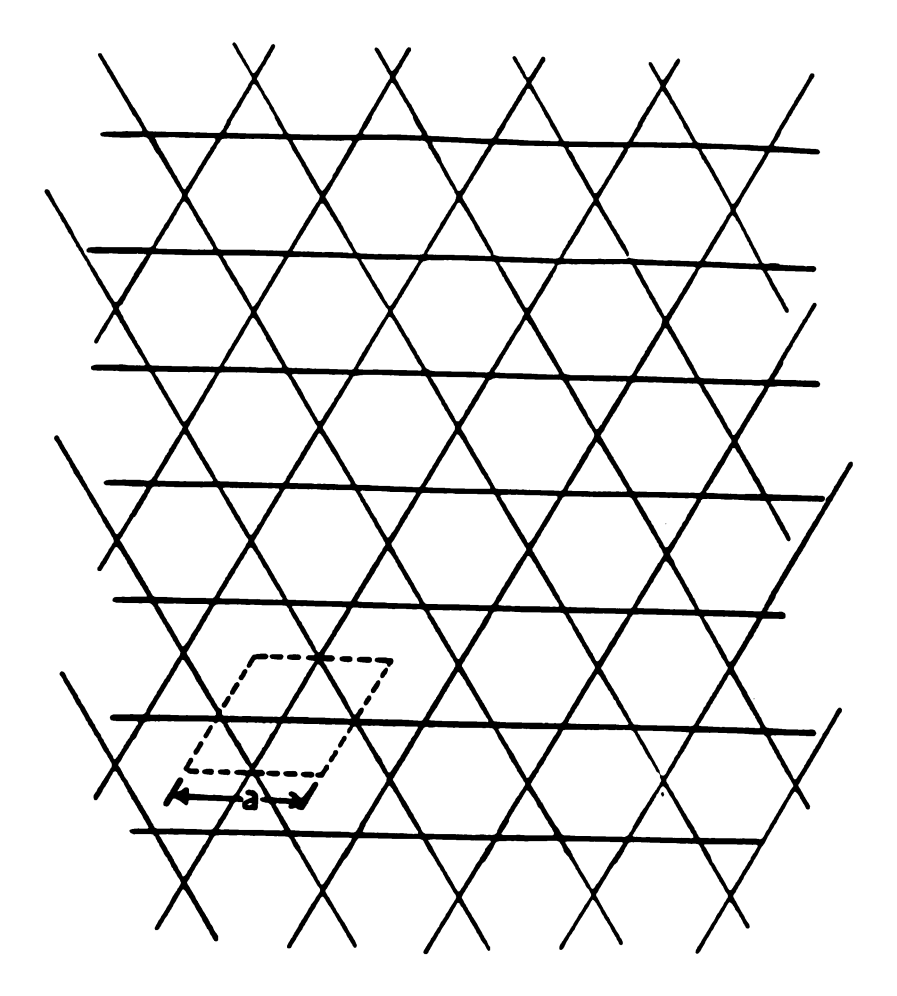


Figure II.2 The Kagome lattice of oxygen atoms (nodes) which form the basal planes of the tetrahedral sheets. The primitive cell (---) and lattice parameter, a = 5.34Å, of the undistorted lattice are shown.

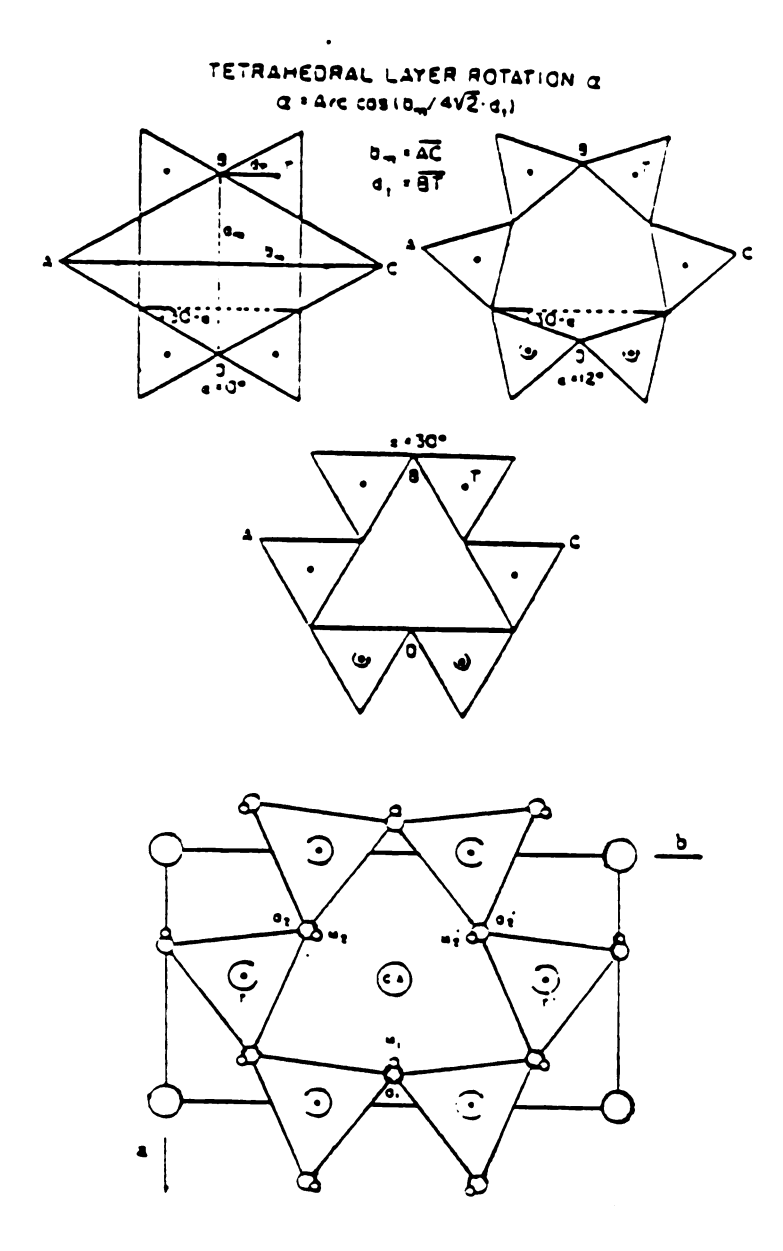


Figure II.3 Schematic view of the basal plane showing the distortion due to alternating clockwise and counter-clockwise rotations of adjacent tetrahedra. The rotation angle is given as $\alpha = \cos^{-1}(b_m/4\sqrt{2}d_T)$ where b_m and d_T are the distances defined in the figure.

III. Layer Rigidity and Collective Effects in Vermiculite Pillared by
Mixed-Alkyl Ammonium Ions

III.1 Introduction

Layered alumino-silicates 15 which are commonly referred as "clay" are unique among lamellar solids in their ability to be pillared 11 by robust intercalated guest ions which occupy specific lattice sites in the lamellar lattices. The resultant pillared clay is characterized by widely spaced host layers that are propped apart by sparsely distributed guest species whose interlayer separation can be many times their diameter. The enormous free volume of accessible interior space that is derived from such an open structure has significant practical implications in the field of catalysis and sieving. 31 In addition the microporous structure of pillared clays provides a natural arena for the exploration of 2D percolation 32 processes. "Access" is one of the most important issues in the application of pillared clay as a catalyst. Here access refers to the general process by which the species to be catalyzed traverse the host medium to the chemically active catalytic site. The concepts of 2D percolation theory are central features of the access phenomenon in clay intercalation compounds. There are four major factors influencing access in pillared ions. These are: layer rigidity. gallery ion distribution, size of the pillaring ions, and the size(shape) of the species to be catalyzed. Among these four factors, the first three determine the basal spacing which can characterize the pore size and shape.

Although it is obvious that layer rigidity and pillaring, which is a special example of the more general phenomena of intercalation, are

interrelated, the pillaring mechanism has, to date, been poorly understood. For instance, rigid layer elastic models 34,35 constitute the only available theory of the composition dependence of the c-axis repeat distance in intercalated layered solids. It is not surprising that such models fail when applied to floppy or moderately rigid hosts such as graphite 36 and layer dichalcogenides. 35 But they are qualitatively inconsistent with data derived from clay hosts to which rigid layer models should be most applicable. In this thesis we report the first successful attempt to quantify and parameterize the relation between pillaring and layer rigidity. To accomplish this we have carried out Xray diffraction studies and computer simulations of the x-dependence of the basal spacing, d(x), of mixed layer vermiculite (Vm) clays $A_{L}B_{1-x}$ -Vm, $0 \le x \le 1$ where A and B are cations (assume A is larger than B) that are judiciously chosen to elucidate the physics of pillaring. In a previous study 30 we examined the $Cs_{\mathbf{x}}Rb_{1-\mathbf{x}}$ -Vm system for which the alkali intercalate species are best characterized as "puny" pillars. Here we focus on the more robust mixed pillar system tetramethyl ammonium-trimethyl ammonium -vermiculite; $[(CH_3)_4N^+]_x[(CH_3)_3NH^+]_{1-x}-Vm$. We find that the pillaring process is a collective phenomena which introduces an intrinsic nonlinearity in d(x). While our layer rigidity model is deduced for clay intercalation compounds it is applicable to other types of intercalated lamellar solids. The extension of this model to other lamellar solids and a discussion of elastic theory on which it is based will be given in Chapter IV.

In ternary clay intercalation compounds many interesting physical properties which include layer rigidity, structure (such as basal spacing), and the distribution of intercalant ions in the galleries are all heavily influenced by the guest-guest and guest-host interactions.

Extensive work on graphite intercalation compounds^{2,33} and other layered solids has shown that Raman spectroscopy is an effective tool with which to study these interactions.

Among the many Raman-active modes in the clay systems we have concentrated on the torsional mode 29 which consists of collective rotational motion of SiO, tetrahedra about vertical Si-O bonds (See Figure III.1.) in Si₂0₅sheet. The torsional mode²⁹ frequency shift which is very sensitive to subtle in-plane structural distortions of the vermiculite host layer is a typical example of the dynamic aspects of layer rigidity. This mode is easier to study than the other phonon modes because it does not include bond bending or bond stretching in tetrahedral and octahedral sheets. Moreover in the torsional mode the intercalants are silent ("at rest"). 29,30 Since the gallery cation is at rest in the torsional mode, the composition dependent frequency shift in this mode can be attributed mainly to the effective force constant changes which result from a contact interaction between the gallery ions and the basal plane oxygens that define its hexagonal pocket. 30 The magnitude of contact (or envelopment) which is affected by host layer "sagging" and gallery ion size can be determined from the basal spacing measurements and we can show the correlation between these dynamic and static effects of layer rigidity.

III.2 Experiment and Results

A naturally occurring single crystal Llano Vermiculite with unit cell formula ${\rm Mg_{0.86}}^{2+}$ [Al $_{0.48}{\rm Mg_{5.52}}$] (Si $_{5.87}{\rm Al}_{2.13}$) O $_{20}$ (OH) $_4$ which is determined from independent chemical analysis is used as the starting material for the synthesis of our mixed alkylammonium ion clays. 16

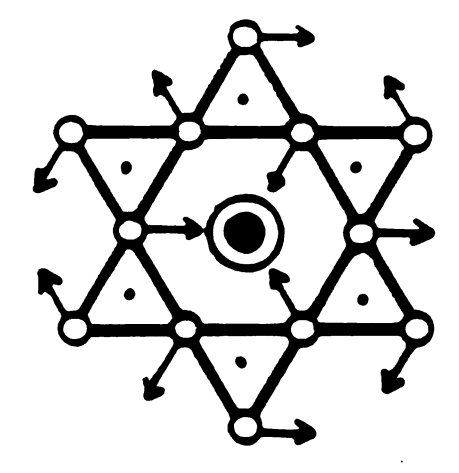


Figure III.1 C-axis view of the vermiculite structure where the eigenvector of the torsional mode is depicted by the arrows. The gallery cation in the middle is shown with oxygens (open circle) and tetrahedral cations (dot).

To synthesize the specimens studied here the ${\rm Mg}^{2+}$ gallery cations which link the layers of natural Llano vermiculite were exchanged for trimethyl ammonium ions using ethylene diamene tetraacetate (EDTA) as a solvent. Subsequent exposure of the pure $[({\rm CH}_3)_3{\rm NH}^+]$ -Vm to the proper amount of $[({\rm CH}_3)_4{\rm N}^+]$ yields a solid solution pillared $[({\rm CH}_3)_4{\rm N}^+]_{\rm x}[({\rm CH}_3)_3{\rm NH}^+]_{\rm 1-x}$ -Vm. Values of the gallery ion composition parameter x were determined from the amount of trimethylamine released upon dispersing known amounts of mixed ion clay products in 1:1 methanol water solutions containing 0.05M NaOH. 16

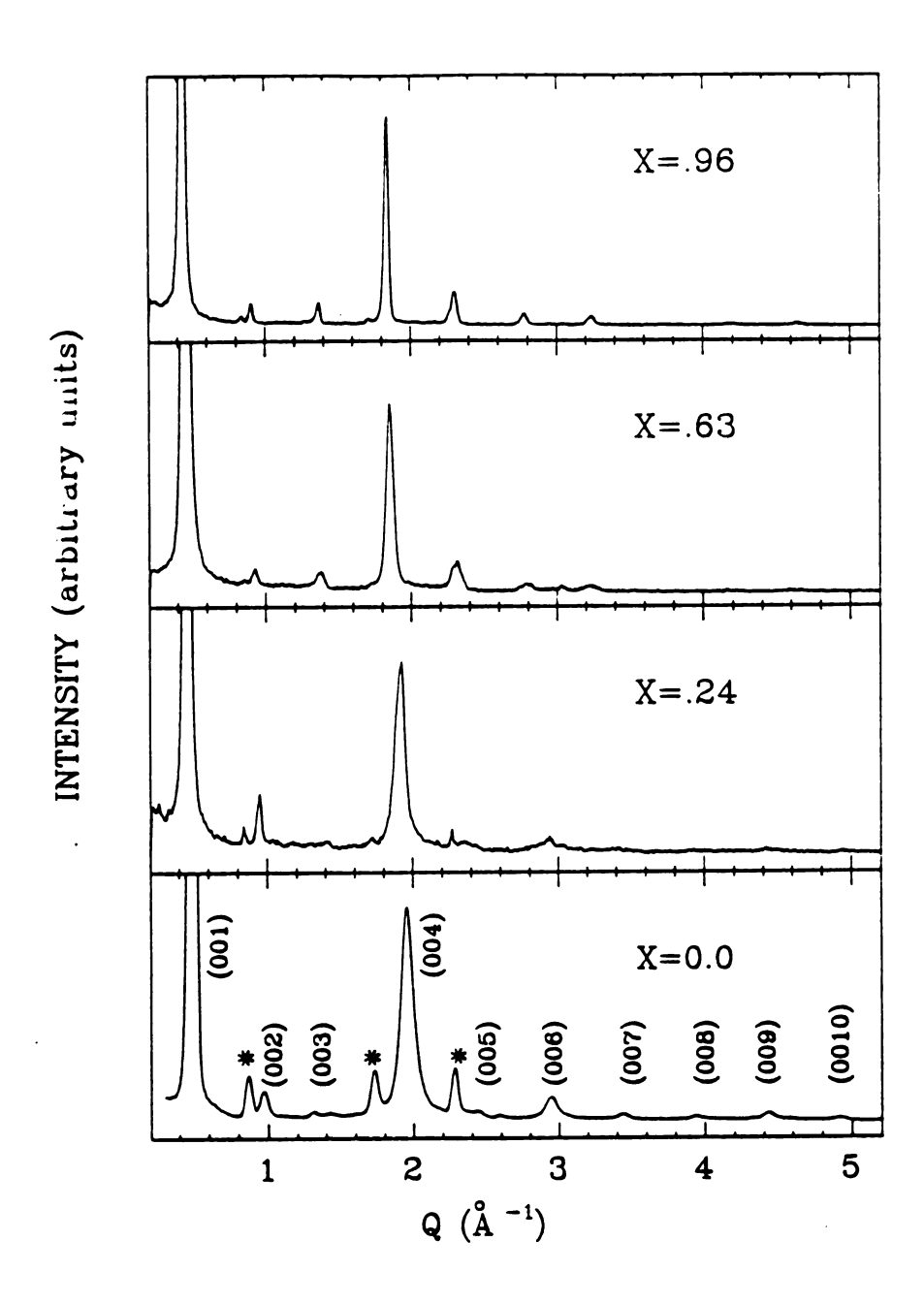
Oriented film samples for X-ray diffraction analysis were prepared by drying approximately 1 ml of a lwt% clay suspension on glass slides. The drying process has been done in two steps. First samples are dried in air at room temperature and then at 100°C in an oven. The air-dried sample exhibits broad (00L) reflections indicative of an interstratified system containing a range of basal spacings due to the mixed hydration state. Upon heating to 100°C, the pattern sharpens dramatically and multiple orders of reflection are observed. An infrared absorption band at 1630cm indicated the presence of water in the interstratified sample dried at room temperature. However, this water affirmation band was absent in the oven-dried sample. 16 The oven-dried sample which was exposed to the ambient atmosphere for prolonged periods of several days did not re-adsorb a considerable amount of water. Free standing clay samples can be obtained by peeling off clay films from the glass substrate. Some of the X-ray diffraction studies reported here are all performed on free standing oven dried samples.

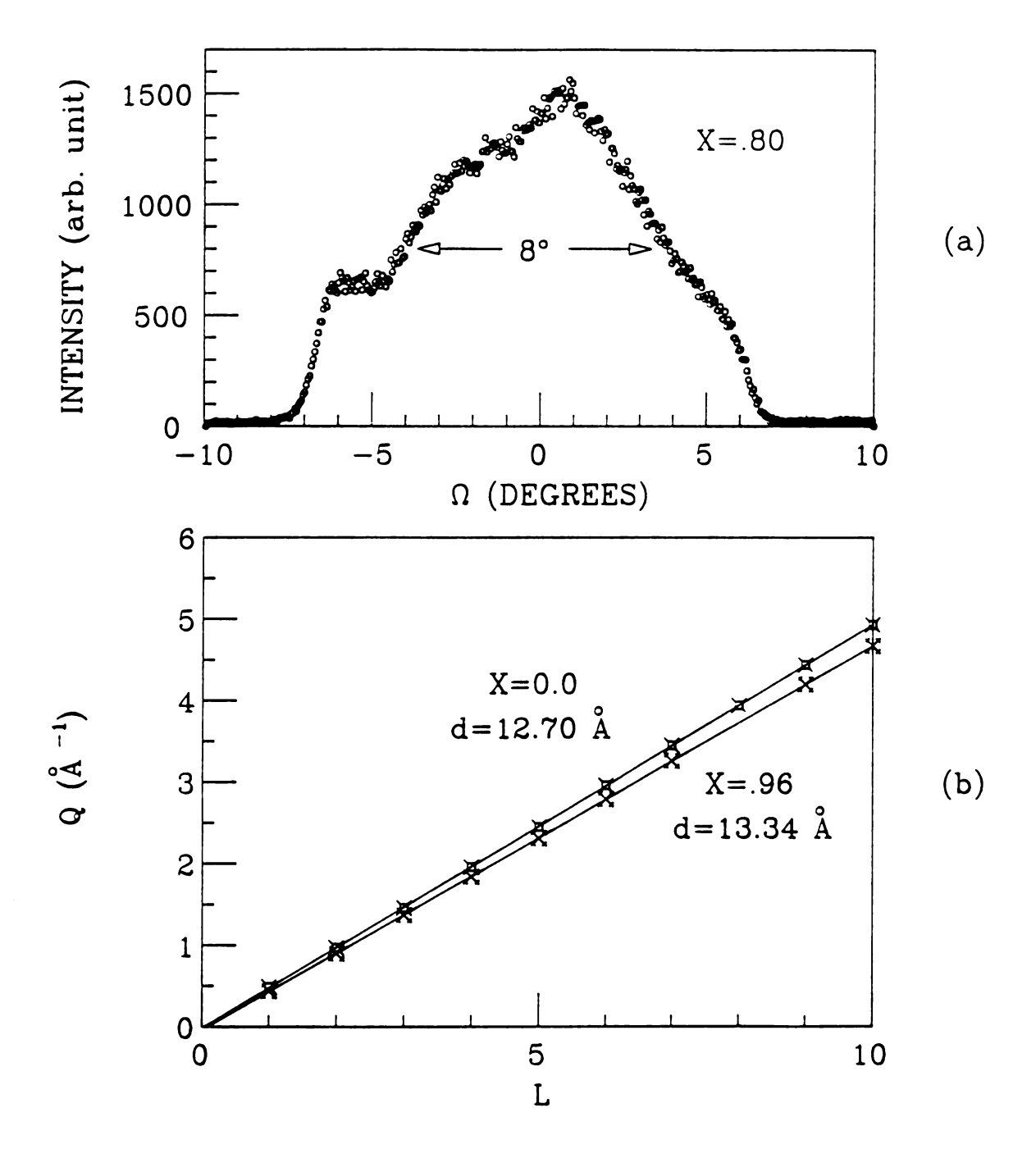
The diffraction patterns reported here were recorded using a 12 KW Rigaku rotating anode X-ray generator, a molybdenum target, and a computer controlled Huber 430-440-512 four circle diffractometer

equipped with a vertically bent graphite monochromator. The (004) reflection of graphite from the ${\rm MoK}_{\alpha}$ radiation was used as the incident X-ray beam for the sample.

The x-dependence of the (00L) X-ray diffraction patterns of $[(CH_3)_4N^+]_x[(CH_3)_3NH^+]_{1-x}$ -Vm is shown in Figure III.2. The starred reflections in that figure are from a small concentration of impurity phase whose 14.48Å basal spacing is x-independent as evidenced by the constant position of the (002) * reflection. Self supporting sedimented films formed on a glass slide exhibited a mosaic 22 spread of $5^{\circ} \leq \Omega \leq 9^{\circ}$ indicating an oriented morphology with the silicate layers parallel to to the slide surface (Figure III.3 (a)). Although the multiple orders of reflection present in the patterns of Figure III.2 provide evidence for a high degree of c-axis crystalline order relative to typical clay intercalation compounds, the reflections are far from resolution limited in width and indicate the effects of limited correlation length along the c-axis. In addition, the evolution in FWHM (Full Width at Half Maximum) reflects the differences in the solvation properties of alkyl ammonium ions in the gallery of the host clay. (See discussion given in section III.3)

Plots of the order, L, versus the momentum transfer $Q = \frac{4 \pi}{\lambda} \sin \theta$ of the reflections of the pillared clays present in Figure III.2 are shown in Figure III.3 (b). To eliminate zero-point calibration errors, the basal spacing d is determined by making a chi-square, χ^2 , minimization of $Q = (\frac{2\pi}{d})$ L + B, which is called a Q-plot. We have obtained d = 12.70Å and d = 13.34Å for x=0.0 and x=.96 respectively. From the fact that we have a linear Q-plot with a well defined slope which corresponds to the basal spacing ~13Å, we can exclude the presence of two demixed heteroionic structures among three possible demixed ion





structures as a candidate for our sample. If the sample consisted of completely phase-separated (AAAA....; BBBB....) compounds one should have been able to distinguish two sets of peaks which can contribute two separate straight lines in a Q-plot. The slope of each of these lines would be composition independent with corresponding basal spacings of 12.70Å and 13.34Å, respectively. If demixed heteroionic clays are ordered in a heterostructure form analogous to the synthetic super lattices (ABABAB.... or AAABBAAABBAAABB..., etc.) there should have been peaks which correspond to a basal spacing larger than 25Å. Such peaks are not observed. The only demixed heteroionic structure that requires more careful discussion is the randomly interstratified (ABBAABABBBABAB....) compounds. 21,37,38 Å detailed discussion of this possibility will be given in the next chapter.

From a series of Q-plots such as shown in Figure III.3 (b), we have determined the composition dependence of the normalized basal spacing, $d_n(x)$, (or normalized c-axis repeat distance) of $[(CH_3)_4N^{\dagger}]_x[(CH_3)_3NH^{\dagger}]_{1-x}-Vm \text{ which is shown in Figure III.4 as open circles. Here the normalized basal spacing, <math>d_n$, is defined as

$$d_{n}(x) = \frac{[d(x) - d(0)]}{[d(1) - d(0)]}$$
 (III.1)

where d(x) is the observed basal spacing. Also shown in Figure III.4 for comparison are corresponding results for Cs_xRb_{1-x} -Vm (open diamonds). ³⁰ Both the Cs-Rb and tetramethyl-trimethyl systems exhibit a sigmoidal shape rise in $d_n(x)$ with increasing x, but the rapid increase in basal spacing occurs at "threshold" values of x_+ = 0.5 and 0.2, respectively.

B. R. York and coworkers have reported the qualitative resemblance of the x-dependent shift in the torsional mode frequency to the corresponding x-dependence of $d_n(x)$ in $Cs_xRb_{1-x}-Vm$. The same resemblance has been observed in the $[(CH_3)_4N^+]_x[(CH_3)_3NH^+]_{1-x}-Vm$ (See

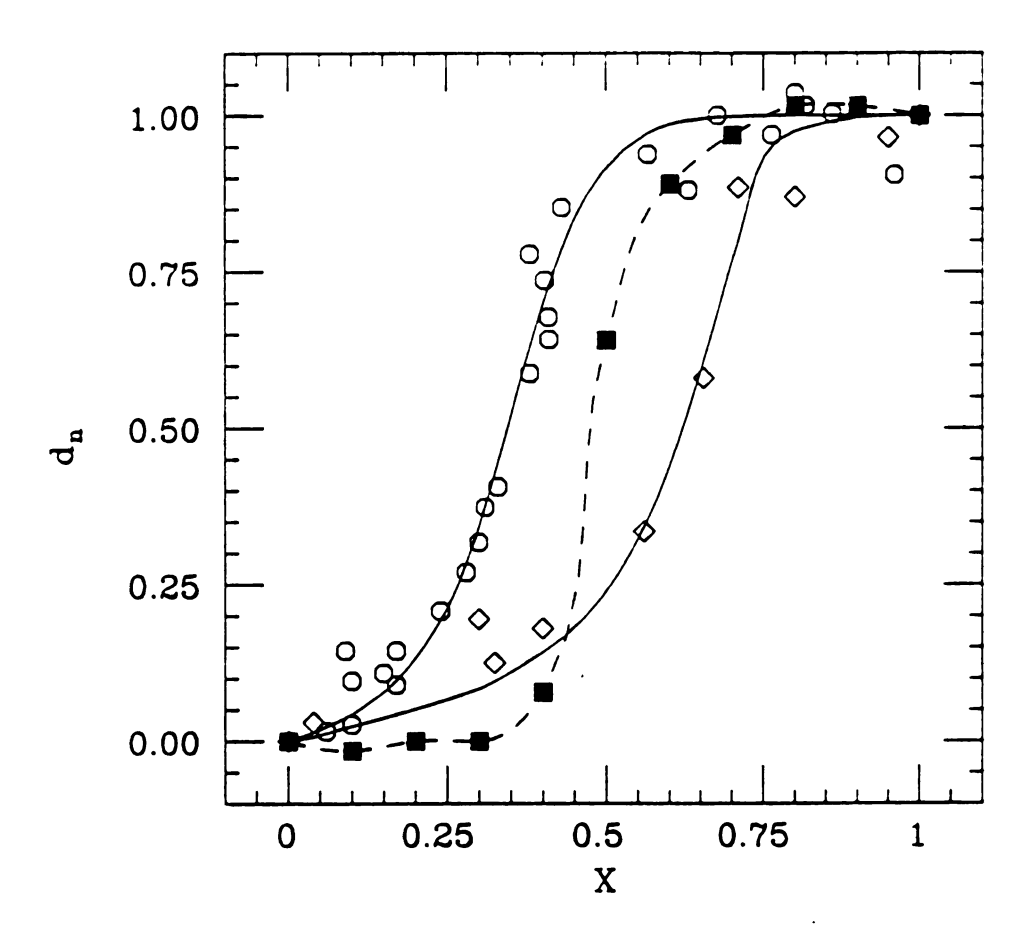


Figure III.4 The composition dependence of the normalized basal spacing of $[(CH_3)_4N^+]_x[(CH_3)_3NH^+]_{1-x}$ -Vm (open circles) and Cs_xRb_{1-x} -Vm (open diamonds). The results of a Hendricks-Teller simulation which will be discussed in the next section is given as solid squares. The solid lines are fits to the data using eq. (III.20) (See the discussion in III.3). The dashed line is a guide to the eye.

Figure III.5). Both the Cs-Rb and $[(CH_3)_4N]-[(CH_3)_3NH]$ systems exhibit a one-mode behavior and a sigmoidal variation of frequency with composition. However comparing with $Cs_xRb_{1-x}-Vm$, 30 whose typical torsional mode frequency is $106~cm^{-1}$, the torsional mode frequency of alkyl ammonium vermiculite shifts to higher energy, $118~cm^{-1}$. This shift suggests that the interactions between alkyl ammonium ions and the basal oxygens of the host silicate layers are stronger than that of Cs^+ and Rb^+ .

The observed shift of the torsional mode to higher energy with increasing x can be interpreted qualitatively by invoking the same encapsulation argument suggested by York and coworkers. Note that although the masses of the large ions (Cs⁺ and [(CH₃)₄N⁺]) are greater than the masses of smaller ions (Rb⁺ and [(CH₃)₃NH⁺]), the x = 1.0 end-members have higher torsional mode frequencies than the x = 0.0 end-members. This is consistent with the fact that the intercalants are "at rest" in the torsional mode so that its frequency does not depend on the intercalant mass, but rather on the effective force constant which must necessarily be greater for Cs⁺ and [(CH₃)₄N⁺] than for Rb⁺ and [(CH₃)₃NH⁺].

For the similar ion sets, $\{Cs^+ \text{ and } Rb^+\}$ or $\{[(CH_3)_4N^+] \text{ and } [(CH_3)_3NH^+]\}$, the difference in the effective force constants can be understood in terms of the encapsulation parameter δ where

$$\delta = (T+H)-d \qquad (III.2)$$

is a measure of the degree to which the cation is enveloped by the bounding oxygen ions. Here d is the d-spacing corresponding to an interlayer cation of ionic height H, and T is the thickness of the silicate layer (See Figure III.6). The larger is δ , the tighter is the encapsulation of the ion and the larger is its effective force constant

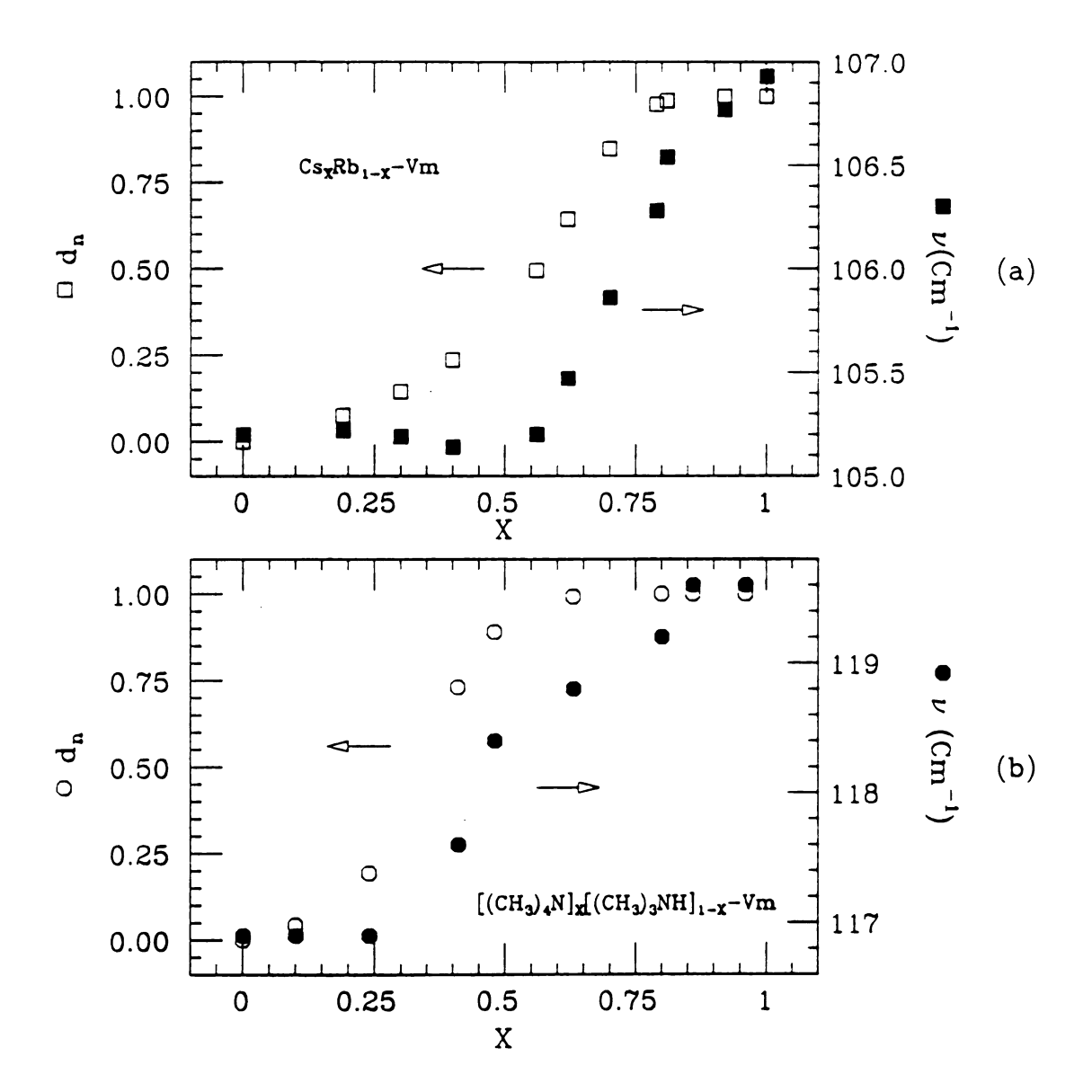


Figure III.5 The composition dependence of the Raman frequency shift of the torsional mode of $\operatorname{Cs_xRb_{1-x}^{-Vm}}$ (solid squares in panel (a)) and $[(\operatorname{CH_3})_4\operatorname{N}^+]_x[(\operatorname{CH_3})_3\operatorname{NH}^+]_{1-x}^-\operatorname{Vm}$ (solid circles in panel (b)) are compared with the x-dependence of the normalized basal spacings of the corresponding compounds (open squares for $\operatorname{Cs_xRb_{1-x}^{-Vm}}$ and open circles for $[(\operatorname{CH_3})_4\operatorname{N}^+]_x[(\operatorname{CH_3})_3\operatorname{NH}^+]_{1-x}^-\operatorname{Vm})$.

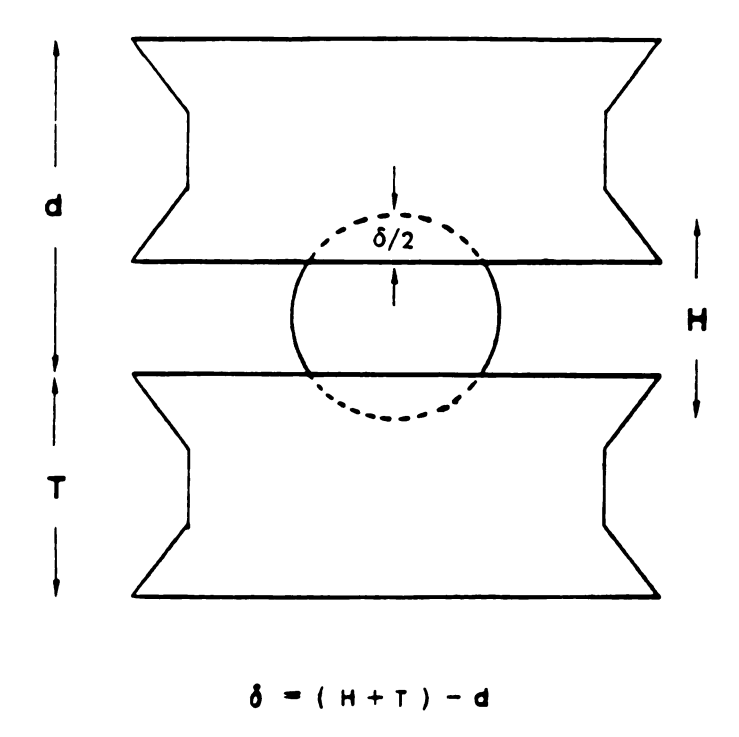


Figure III.6 Schematic illustration of encapsulation. Part of the gallery cation which is encapsulated by the bounding oxygen planes is depicted by broken lines. T is the thickness of the pristine host layer.

of interaction with its oxygen neighbors. From the measured values of basal spacings, the known values of ion sizes, and the known value of silicate layer thickness T = 9.34Å, we find $\delta_{\text{Cs-Vm}}$ = 2.15Å, $\delta_{\text{Rb-Vm}}$ = 2.07Å, and $\delta_{\text{[(CH}_3)_4\text{N]-Vm}}$ = 0.20Å. Notice that $\delta_{\text{[(CH}_3)_3\text{NH]-Vm}}$ < 0; This means [(CH₃)₃NH⁺]-Vm has no encapsulation (See Table III.1.).

The marked difference in the encapsulation between Cs+Rb+1-r-Vm and alkyl ammonium vermiculite can be attributed to the size effects of the intercalant ions. In clay intercalation compounds the intercalants are sitting on the the hexagonal pockets of an oxygen kagome lattice and as is well known these oxygen planes are capable of performing torsional distortions. 21 The hexagonal pockets have an edge length of 5.34A which defines the opening after the diameter, 2.67Å, of the constitute oxygen is considered. For the cations which have lateral dimensions that are less than or comparable to the pocket size these oxygen layers would have a torsional distortion which increases δ . By increasing δ the quasi-rigid silicate host layers can accomodate cations with minimum generation of transverse distortions. But if the cations become too large, the host layer cannot provide sufficient torsional distortion to accomodate them. Hence the basal spacing change from that of the pristine sample is far less sensitive to the ion size with the smaller ion set than with the larger ion set. From the first column of Table III.1 we find $\Delta d_{Cs-Vm} = 1.23\text{\AA}$, $\Delta d_{Rb-Vm} = 0.89\text{\AA}$, $\Delta d_{[(CH_3)_4N]-Vm} = 4.0\text{\AA}$, and $\Delta d_{[(CH_3)_3NH]-Vm} = 3.36\text{Å}$ where Δd is the net basal spacing increase; Δd = d - T. The last column of Table III.1 shows δ/H which is a measure for relative encapsulation. In the case of "puny" pillars such as Cs, Rb and Na, almost 70% of gallery cation size is enveloped by the bounding

Table III.1 Intercalant size effect on encapsulation

Intercalants	d(Å)	H(Å)	D(A)	δ(Å)	δ/H(Z)
[Me ₄ N ⁺]	13.34	4.2	4.8	0.20	4.76
[Me3NH+]	12.70	3.2	4.0	< 0	
Cs ⁺	10.57	3.38	3.38	2.15	63.6
Rb ⁺	10.23	2.96	2.96	2.07	69.9
Na ⁺ (*)	9.75	1.96	1.96	1.55	79.1

^{*:} from D. R. Hines, N. Wada and M. Suzuki, Bull. Am. Phys. Soc. 32, 559 (1987).

d is the basal spacing of M^+ -V, H and D are the height and diameter of cation, and the encapsulation parameter is defined as $\delta = (T+H)-d$ where T=9.34(Å) is the thickness of the silicate layer.

cf. $D(Li^{+})=1.36(\text{Å})$ and $D(Mg^{+2})=1.30(\text{Å})$

Kagome oxygen layers but envelopment of the more robust pillars such as tetramethyl ammonium and trimethyl ammonium is negligible.

This static torsional distortion, not accidently, is identical to the eigenvector of the torsional interlayer phonon mode. Thus, we expect this mode in particular to be sensitive to the composition of the interlayer cations. This expectation is confirmed by Figure III.5 which shows an x-dependent shift in the frequency of the torsional mode that qualitatively mimics the corresponding x-dependence of $d_n(x)$.

The correlation between the static deformation and the dynamic torsional mode frequency is more vividly illustrated in Figure III.7, in which we have plotted the normalized basal spacing, $\mathbf{d_n}$, versus the normalized torsional mode frequency, $\mathbf{v_n}$, to compare data between two different sets of mixed cation compounds. The normalized Raman torsional frequency shift, $\mathbf{v_n}$, is defined as

$$v_{n}(x) = \frac{[v(x) - v(0)]}{[v(1) - v(0)]}$$
 (III.3)

Figure III.7 shows striking "scaling-like" behavior in which the data for two very different mixed-ion vermiculite clays, Cs_xRb_{1-x} -Vm and $[(CH_3)_4N]_x[(CH_3)_3NH]_{1-x}$ -Vm, fall on the same curve. Also the plot clearly shows three characteristic regimes whose underlying physics could be drastically different. In the first regime, ν_n does not change with d_n , in the intermediate regime ν_n increases almost linearly with d_n , and in the third regime ν_n increase but d_n does not change.

This scaling-like behavior and the qualitative resemblance between $d_n(x)$ and $v_n(x)$, all lead to one point; much of the physics in vermiculite intercalation compounds is governed by a common source, namely host layer rigidity and the interaction between intercalants and the host layer. This very important idea will be incorporated into our discussion of an elastic model of layer rigidity in chapter IV.

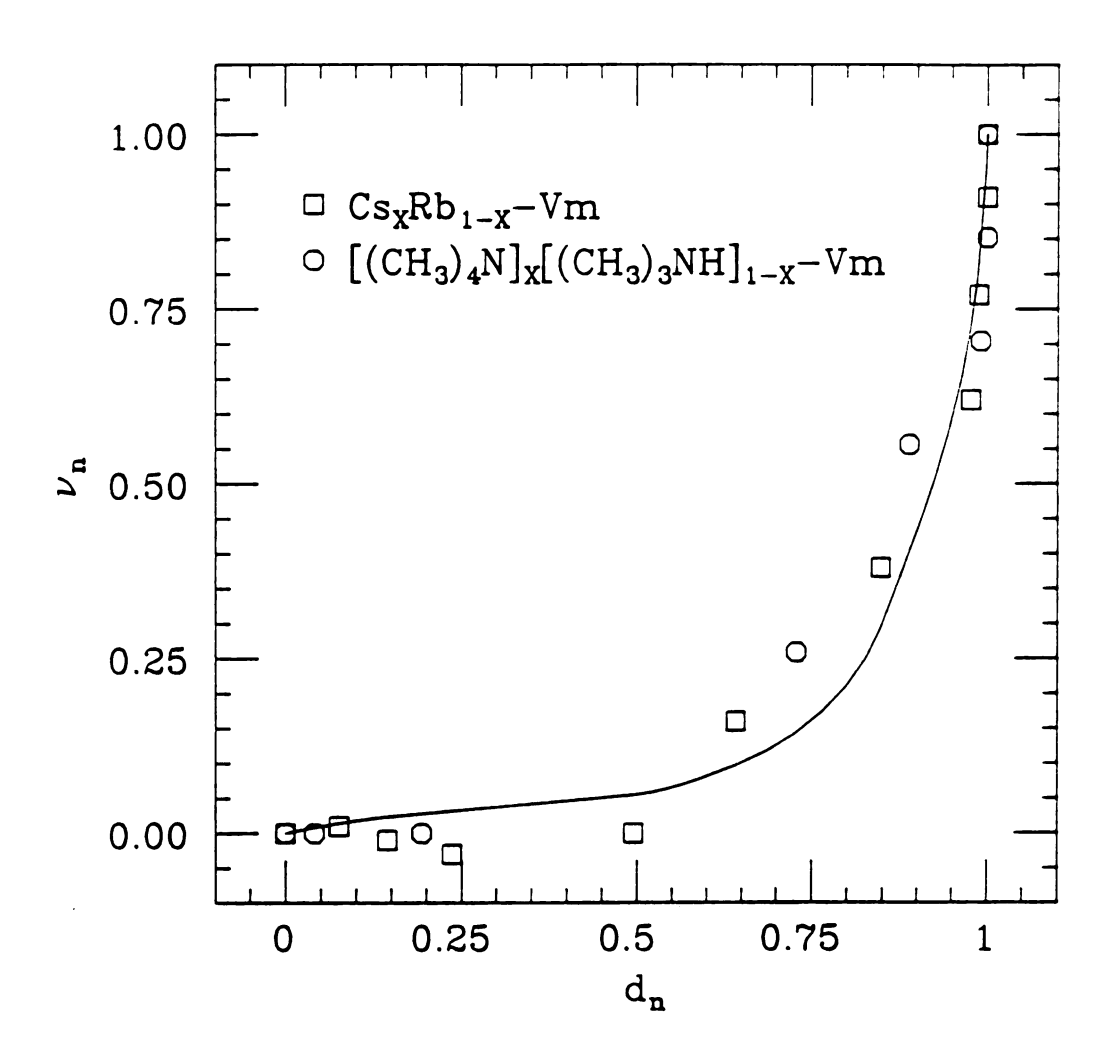


Figure III.7 The normalized torsional mode frequency, $\nu_{\rm n}$, plotted versus normalized basal spacing, ${\rm d_n}$, of ${\rm Cs_xRb_{1-x}}$ -Vm (open squares) and ${\rm [(CH_3)_4N^+]_x[(CH_3)_3NH^+]_{1-x}}$ (open circles). The solid line is a fit using the function discussed in the section III.3.

It is important to establish that the $[(CH_3)_4N]_x[(CH_3)_3NH]_{1-x}$ -Vm mixed ion system is indeed homogeneous and that the individual type of guest ion did not segregate into islands in the same gallery or into separate galleries to form an interstratified structure. Many arguments which can confirm the homogeniety of the admixture of gallery ions in the $[(CH_3)_4N]_x[(CH_3)_3NH]_{1-x}$ -Vm system require use of the X-ray structure factor G_{001} , which contains c-axis structural information.

In general the structure factor for a given (HKL) reflection G_{HKL} is obtained by the addition of contributions from each of the atoms in the unit cell. ⁴⁰ In particular the layer structure factor for the (00L) reflections of a layered solid like $[(CH_3)_4]_x[(CH_3)_3NH]_{1-x}$ -Vm can be written as

$$G_{00L}(Q) = \sum_{j} n_{j} f_{j} \cos(QZ_{j}) + i \sum_{j} n_{j} f_{j} \sin(QZ_{j})$$
 (III.4)

The summations are taken over all atoms in the unit cell and n_j refers to the number of atoms of type j that are located parallel to the ab-plane. The distance Z_j is the height of an atomic plane above the plane that has been selected as the origin of the structure. The symbol f_j is the amplitude scattered by the jth atom and Q is the momentum transfer along the c-axis, while $Q_{OOL} = \frac{2 \pi}{d}$ L are reciprocal lattice vectors. The atomic scattering factors include corrections for temperature according to

$$f_j = f_j^0 e^{-W_j(Q/4\pi)^2}$$
 (III.5)

where the W_j 's are the Debye-Waller factors.⁴⁰ For centrosymmetric systems like vermiculite intercalation compounds,²¹ the sin-terms in eq. (III.4) vanish and we are left with

$$G(Q) = 2 \sum_{i} n_{i} f_{i} \cos(QZ_{i})$$
 (III.6)

G is then a positive or negative number and the sign can be determined from a model calculation. The observed integrated intensity \mathbf{I}_{00L} can be directly related to the scattering factor $\mathbf{G}_{00L}(\mathbf{Q})$ after corrections for the unequal contributions from the two polarization components of the X-ray beam and geometric effects (Lorenz-Polarization factor) are made

$$G_{OOL} = [SI_{OOL}/LP]^{1/2}$$
 (III.7)

where S is a scaling factor and LP is the combined Lorentz-polarization factor.

For our scattering configuration shown in Figure III.8 the LP factor is given by

$$LP(Q) = \frac{1 + \cos^2 2\phi \cos^2 2\theta}{(1 + \cos^2 2\phi) \sin 2\theta}$$
 (III.8)

where ϕ is the (004) Bragg angle setting of the graphite monochromator ⁴¹ and $\theta = \sin^{-1}(Q\lambda/4\pi)$. Using eqs. (III.6) and (III.7), the measured integrated intensities can be fitted to yield the structure factors for the two end-member compounds of mixed alkylammonium ion vermiculite, x = 0.0 and x = 0.96. In Figure III.9 the calculated relative intensities (solid lines) are shown with the experimentally measured relative intensities (open circles and squares) for the two end-member compounds. The fits are very good and the residual ⁴² which is the standard measure used to assess the agreement.

$$R = \frac{\Sigma ||G^{obs}| - |G^{cal}||}{\Sigma |G^{obs}|}, \qquad (III.9)$$

is $R \approx 0.05$ for x = 0.0 and $R \approx 0.06$ for x = 0.96 respectively. In this fitting, the silicate host layer chemical composition was fixed and the

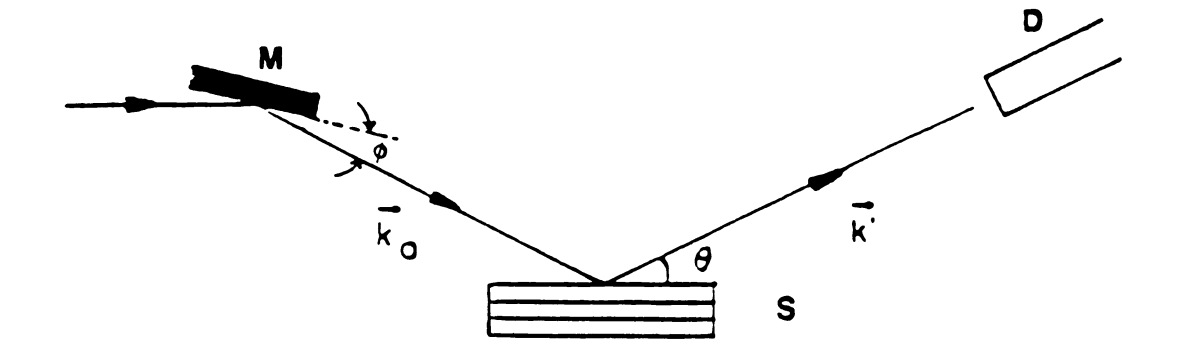


Figure III.8 A schematic diagram for a (00L) X-ray scan where M is a graphite monochromator, S is the sample, and D is the detector. \vec{k}_0 and \vec{k} are incoming and outgoing X-ray wavevectors, respectively.

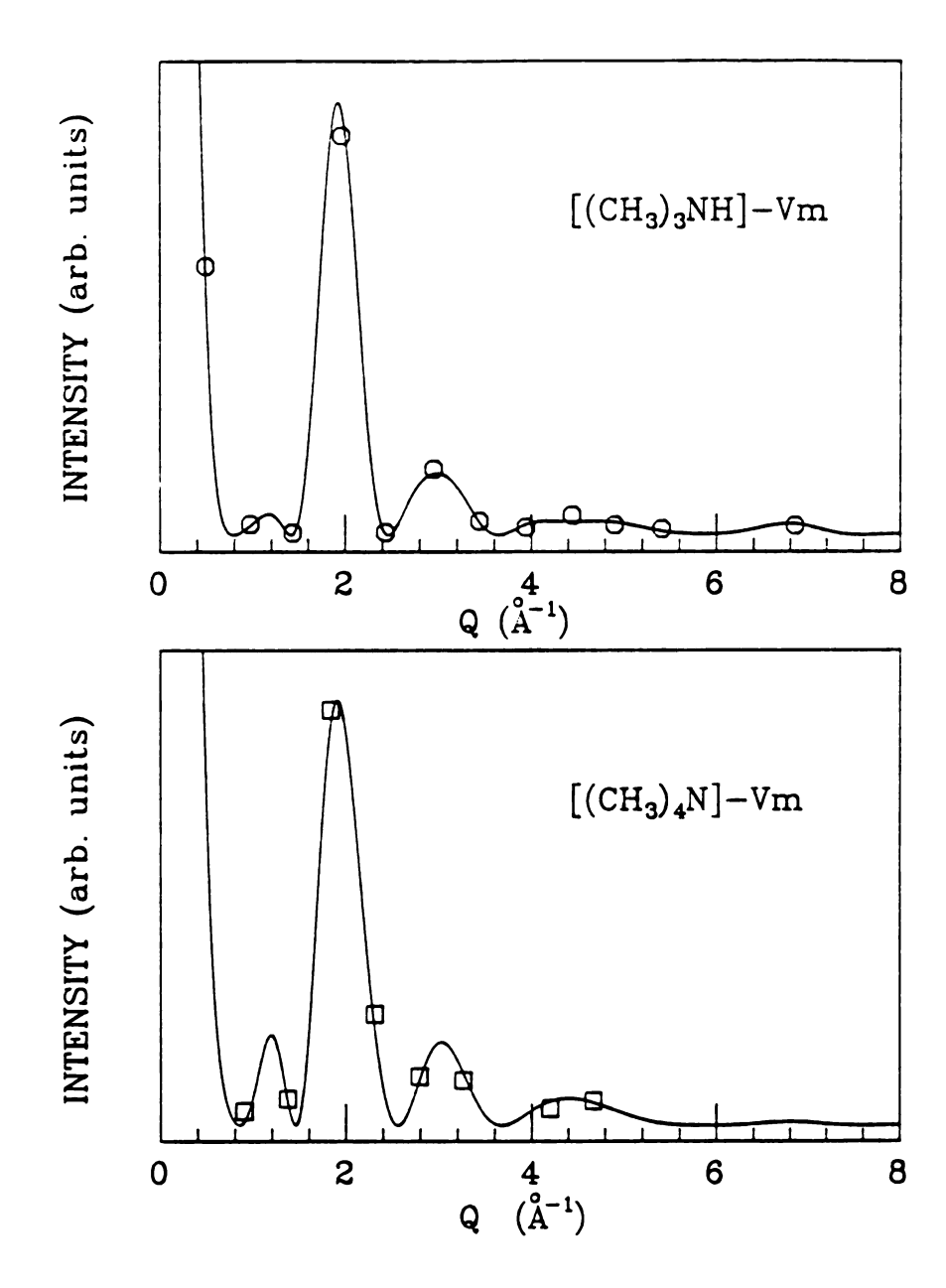


Figure III.9 A plot of the calculated and measured relative integrated intensities of the X-ray reflections from $[(CH_3)_3NH]-Vm$ and $[(CH_3)_4N]-Vm$. The open circles and open squares represent experimentally measured (00L) integrated intensities of $[(CH_3)_3NH^+]-Vm$ and $[(CH_3)_4N^+]-Vm$, respectively. The calculated curves are obtained from a least square fit to the experimental data using eqs. (III.6) and (III.7) of the text.

atomic plane height, \mathbf{Z}_{j} , and Debye-Waller factor \mathbf{W}_{j} were allowed to change.

For the intercalants, instead of using a molecular form factor we simply summed the atomic form factors of the constituents and used a single Debye-Waller factor. The best fit of integrated intensity is obtained when the gallery occupation number $(n_{[(CH_3)_4N]} \text{ or } n_{[(CH_3)_3NH]})$ is about 1.2 and the Debye-Waller factors for the intercalants are respectively W = 30 for x = 0.0 and W = 59 for x = 0.96. Note that the gallery occupation number of 1.2 is consistent with the known vermiculite layer charge density, ²¹ even though an independent layer charge density determination yields a higher charge density. The large Debye-Waller factor for organic intercalants in clay intercalation compounds is not uncommon. ⁴³ Alkyl ammonium ions in vermiculite intercalation compounds are known to exhibit a fast spinning top like motion from inelastic neutron scattering. ⁴⁴ Hence the Debye-Waller factor which depends on atomic displacements about their equilibrium positions will be larger for the alkyl ammonium ions.

In addition to the above mentioned scattering factor and Lorentz-polarization factor, the one dimensional diffraction profile of a mixed alkylammonium ion vermiculite system also depends on the interference function which is a broadening factor that accounts for finite size effects and stacking irregularities. 21

$$I(Q) = S|G(Q)|^{2}LP(Q)\Phi(Q) \qquad (III.10)$$

where I is the intensity, S is a scale factor, $|G|^2$ is the squared scattering factor from the unit cell, and Φ is an interference function. For the solid solution type mixed intercalants the interference function is given by the Bragg expression 45

$$\Phi(Q) = \frac{\sin^2(NQd/2)}{\sin^2(Qd/2)} = \Sigma N^2 \exp[-(Q-Q_L)^2/(\Gamma^2/4\ln 2)]$$
 (III.11)

where Γ can be determined from the full width of a (00L) reflection through the relation 40

$$\Gamma = 4 \times 1.4 / L_{C}$$
 (III.12)

here L_c = Nd is the correlation length along the c-axis.

The first quantitative mathematical treatment of diffraction processes by interstratified systems was carried out by Hendricks and Teller. 46 Random interstratification is a process in which two species A and B of basal spacing \mathbf{d}_{A} and \mathbf{d}_{B} are randomly distributed. 21 The interference function for random interstratification is given by

$$\Phi(Q) = \frac{2P_{A}P_{B}\sin^{2}(Q(d_{B}-d_{A})/2)}{1-2P_{A}P_{B}\sin^{2}(Q(d_{B}-d_{A})/2)-P_{A}\cos(Qd_{A})-P_{R}\cos(Qd_{B})}$$
(III.13)

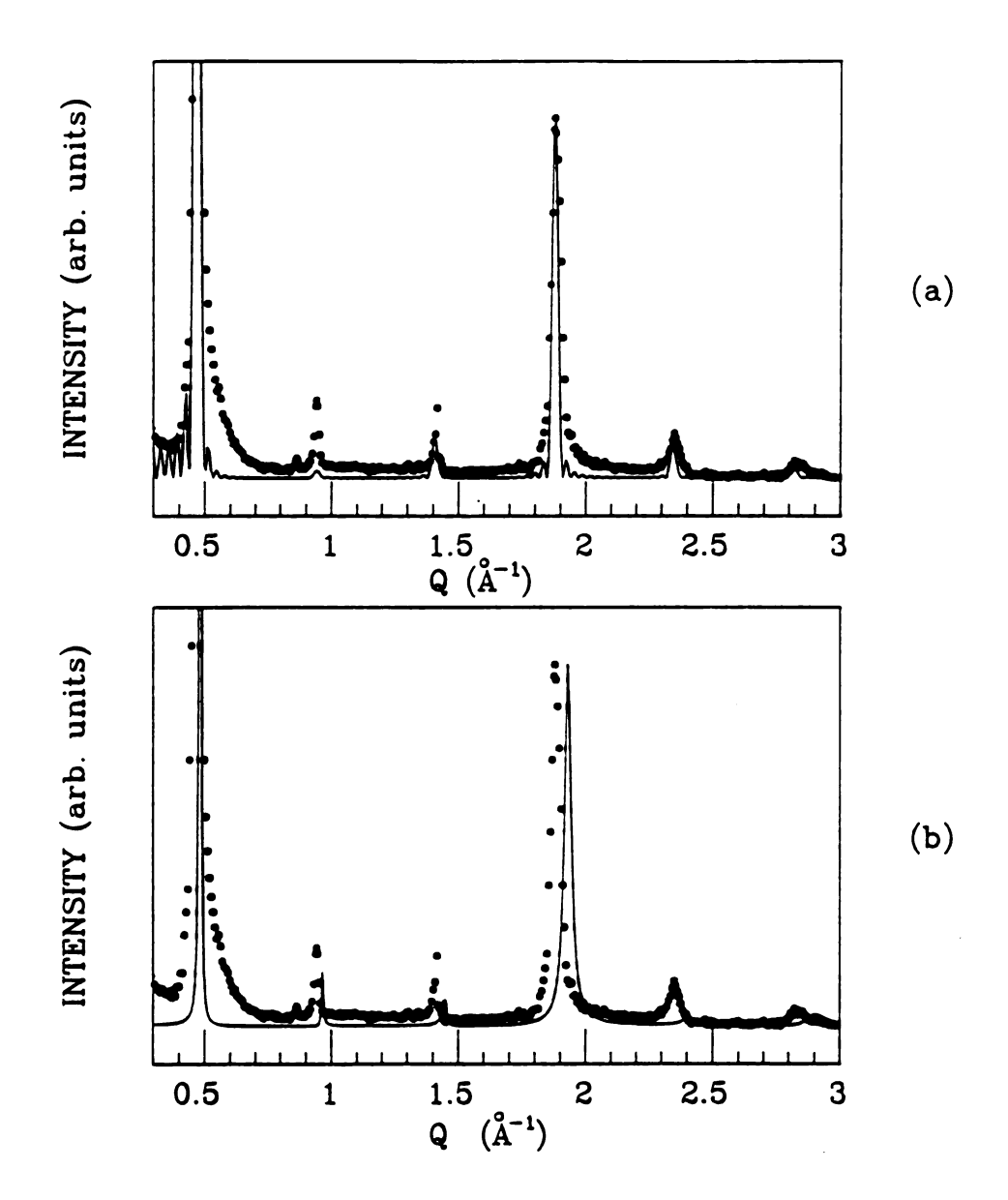
where P_A and P_B refer to the proportion of species A and B of basal spacing d_A and d_B respectively, such that $P_A + P_B = 1$.

To investigate possible interstratification we have carried out a series of computer simulations of the X-ray diffraction patterns of the mixed alkylammonium ion vermiculite system using both of the above mentioned interference functions and compared them with the corresponding experimental (00L) X-ray diffraction patterns. For the Bragg interference function which is suitable for a solid solution arrangement of ions for all galleries, a single basal spacing d(x) measured in the experiment using the Q-plot is used. For the Hendricks-Teller (HT) interference function, the experimentally measured end-member basal spacings d(0) and d(1) are used. Following MacEwan's suggestion²¹ the "effective" layer scattering factor, given by

$$|G|_{eff}^2 = [|G_A|^{P_A}|G_B|^{P_B}]^2$$
 (III.14)

is used with the end-member layer scattering factors determined from the fitting of the integrated intensity of the experimental X-ray pattern. Lorentz-polarization corrections were also included. For the Bragg reflections, a finite sized sample containing 15 clay layers was assumed. This contributed to the broadening of the calculated Bragg reflections. For the HT model, an infinite number of layers were assumed and the broadening of the reflections is intrinsic to the model itself (i.e. the random demixing of ions into galleries of two different heights). In Figure III.10 (a) we compare the observed (00L) reflections with the computer generated Bragg X-ray reflections for x = 0.63. As can be seen from that figure reasonable agreement is obtained for both the peak positions and relative intensities. The lower panel illustrates the comparison between the same observed reflections, x = 0.63, and the simulated HT X-ray reflections. Clearly, the HT simulations yields an inferior result. This result strongly suggests a solid solution arrangement of the ions in mixed alkylammonium ion vermiculite and in which all galleries have the same height.

In Figure III.11 a series of simulated HT reflections are shown. We have treated the computer generated (00L) X-ray diffraction pattern exactly the same way as we have treated the experimental pattern to determine the x-dependent basal spacing variation. Unlike the experimental pattern which exhibits a high degree of linearity in its corresponding Q-plot, the Q-plot derived from the HT simulation exhibits a periodic oscillation around the best linear least square fit. The x-dependent basal spacing of the HT simulation is illustrated in Figure III.4. In comparison with the experimental x-dependent basal spacing of $[(CH_3)_4N^+]_x[(CH_3)_3NH^+]_{1-x}$, it is not at all similar. For example its characteristic symmetric step-like change about x = 0.5 with over- $(d_n > 1)_{n-1}$



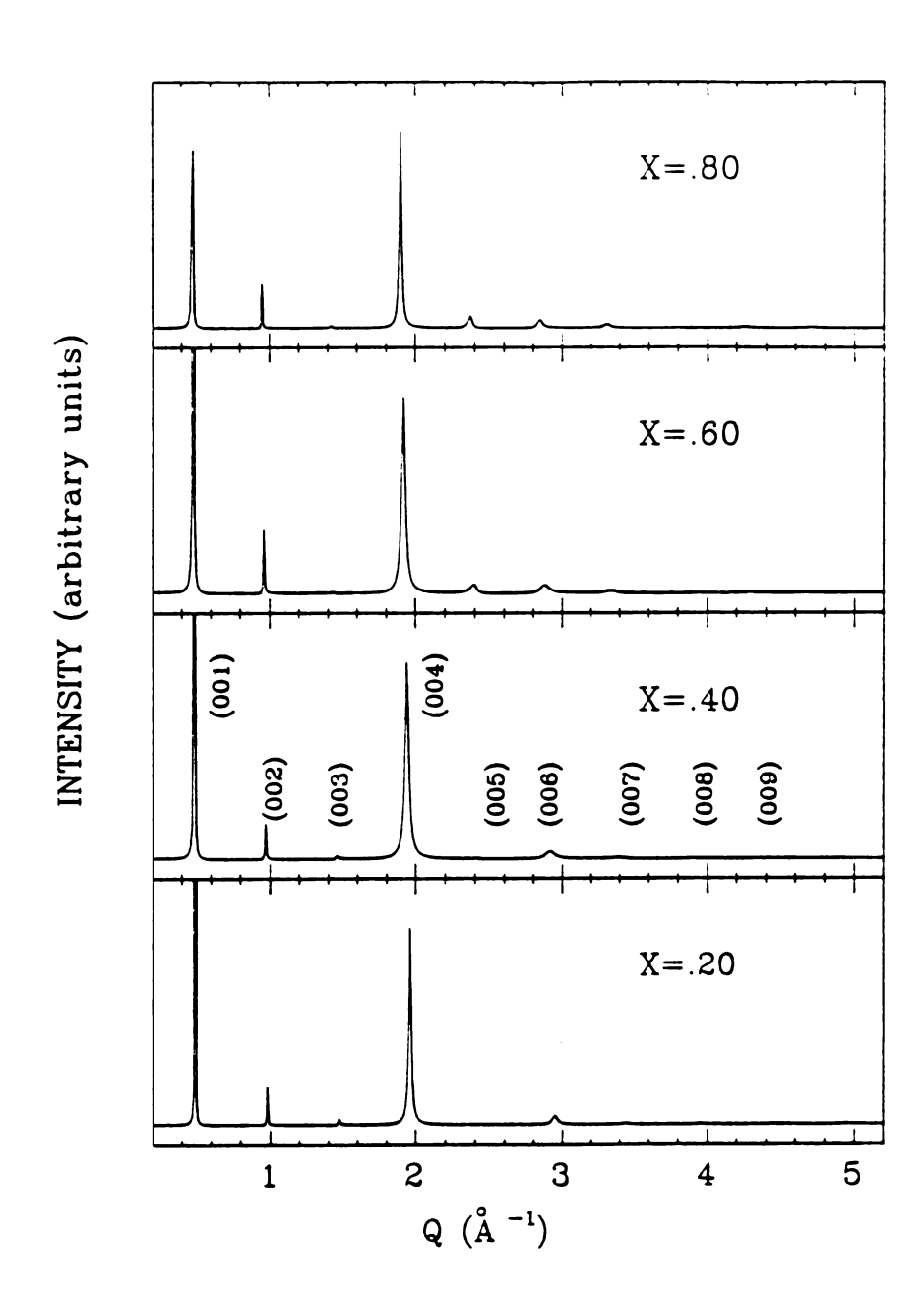


Figure III.11 The computer generated Hendricks-Teller X-ray diffraction patterns for a randomly interstratified array of two gallery heights $d_{A}=13.34 \text{\AA}$ and $d_{B}=12.70 \text{\AA}$. An infinite number of layers were assumed

1.0) and under-shooting $(d_n<0.0)$ regions are not observed in the experimental basal spacing variations. Also unlike the experimental X-ray patterns, the FWHM of the (004) peaks are wider in the intermediate x range and narrow as x approaches the x = 0.0 or x = 1.0 limits. This is further strong evidence against interstratification.

Yet additional evidence against interstratification can be obtained using the so called Patterson function which is the direct Fourier transformation method of the observed X-ray pattern developed by A. L. Patterson. 40,47 The Patterson function which is a Fourier series whose coefficients are $|G|^2$ is a correlation function giving the position of every atom relative to every other atom, but not relative to a fixed origin. The quantity $|G|^2$ which is a squared structure factor is directly obtainable from the measured integrated intensities without knowledge of the phase. The peaks in the patterson function do not represent the positions of atoms, but are the terminal points of a set of vectors, each of which represents the displacement of some atom from some other atom. As a variation of the Patterson function, MacEwan 48,49 defined the function W(R) as the probability of finding a given layer to layer distance R in a crystal space. The function is given by

$$W(R) = \Sigma \frac{I(Q_{00L})}{LP(Q_{00L})|G(Q_{00L})|^2} \cos (Q_{00L}R)$$
 (III.15)

where the inter-layer distance R is systematically varied typically from 0\AA to 50\AA and the sum is taken over all diffraction peaks. By dividing I by LP and $|G|^2$ we can extract the effects of the Lorentz-polarization factor, and reduce the layer transforms to unity. The result is, ideally, the interference function Φ , which is the quantity of interest. Summation over all the peaks produces a Fourier series, the components of which are waves of amplitude $I/(LP|G|^2)$, and whose phase angles with

respect to R = 0 are all zero. For the layer scattering factor, the effective scattering factor defined in eq. (III.14) is used. The function W(R) has peaks at values of R that denote the relative abundance W(R) of different inter-layer distances, R. Omission of the (000) diffraction, which is equal to the total number of electrons per unit cell, causes the appearance of negative values²¹ in the transform, and complicates a quantitative analysis. However qualitatively this approach still represents a good way to identify interstratification.

The Patterson functions of interstratified compounds have quite distinctive features. For example interstratified $[(CH_3)_4N^+]_{0.63}[(CH_3)_3NH^+]_{0.37}$ -Vm would show peaks at R = 12.70Å, R = 13.34Å, R = 25.40Å, R = 26.04Å, R = 26.68Å, etc. with relative heights which are roughly proportional to 0.63, 0.37, 0.14, 0.23, 0.39, etc. respectively. But for all values of x investigated, only a single vector distribution corresponding to a unique d(x) value was observed, and neither peaks corresponding to two different end-member basal spacings nor the sum of these d values were observed. In Figure III.12, the Patterson functions of $[(CH_3)_4N^+]_x[(CH_3)_3NH^+]_{1-x}$ -Vm are shown for x = 0.96, x = 0.63, x = 0.24 and x = 0.0. None of these shows the signs of interstratification discussed above and all the peaks are at a distance that is an integer multiple of d(x). Thus interstratification of two kinds of layers with basal spacings of 13.34Å and 12.70Å is precluded.

Once interstratification is precluded, the observed line width of the (00L) reflections can be attributed to the finite correlation length along the c-axis. From a Gaussian fit to the observed reflections (see eq. (III.11)), we can determine the FWHM Γ . The x-dependent FWHM's obtained using the (004) reflections are shown in Figure III.13 (a). In determining the correlation length L_c experimentally one must account

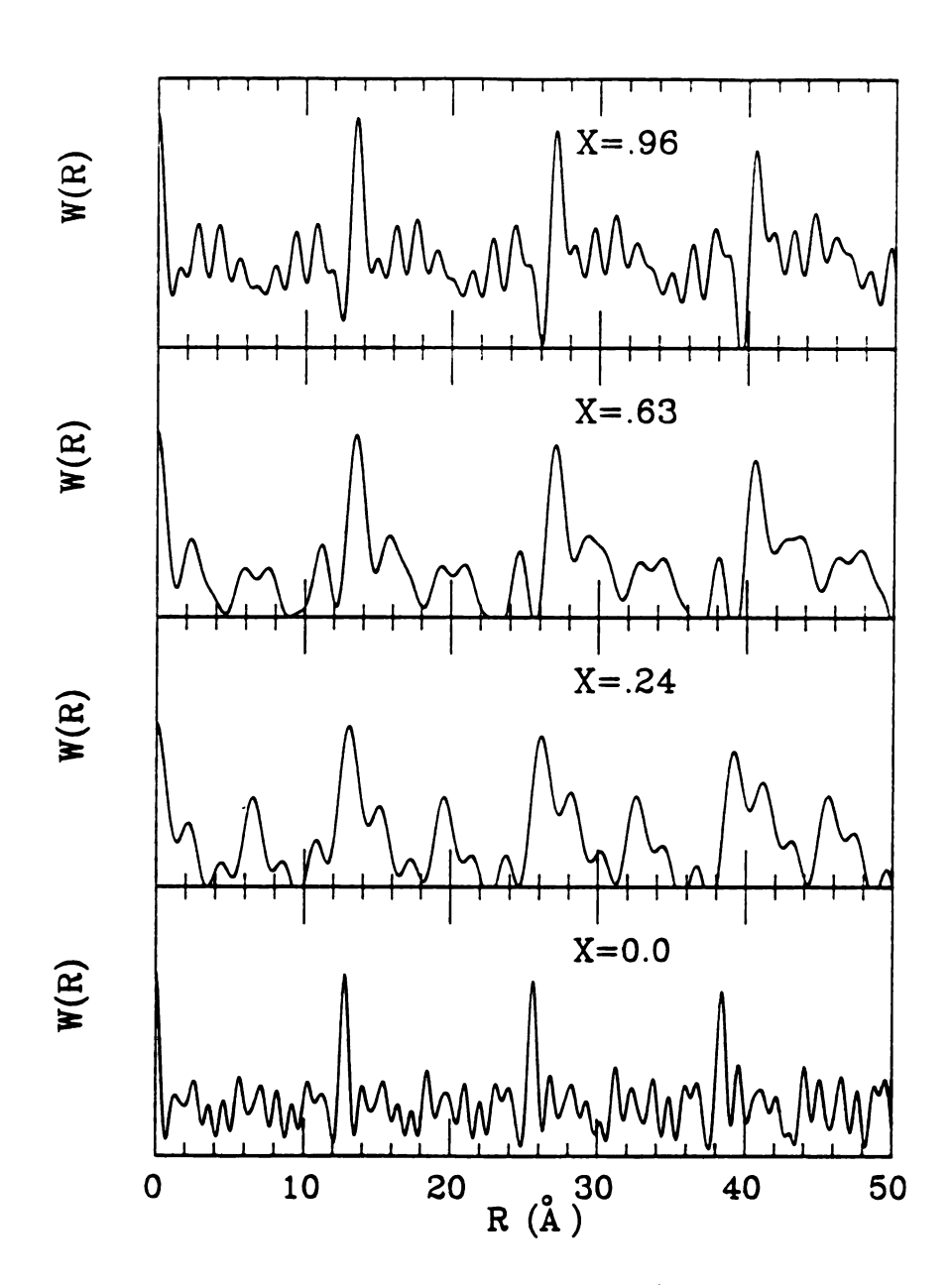


Figure III.12 A Patterson Synthesis. Only a single vector distribution corresponding to a unique d(x) value was observed. Thus, segregation of the two ions into separate galleries with heights $d_{\hat{A}}$ = 13.34Å and $d_{\hat{B}}$ = 12.70Å can be precluded.

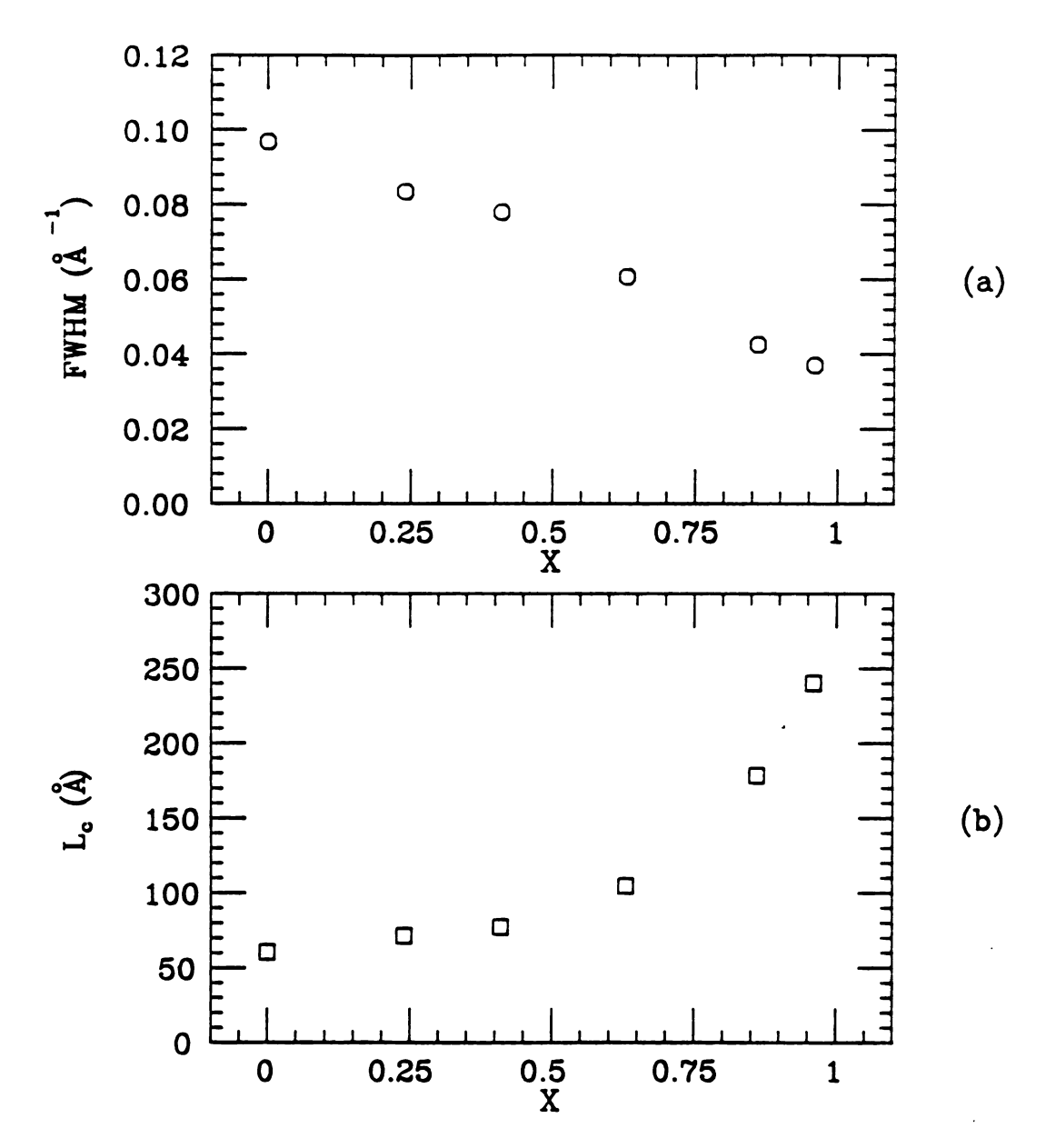


Figure III.13 The composition dependence of (a) FWHM obtained using the (004) peak of $[(CH_3)_4N]_x$ -Vm $[(CH_3)_3NH]_{1-x}$ -Vm and (b) the corresponding correlation lengths along the c-axis after correction for the instrumental broadening.

for the instrumental contribution to the observed width. We do this by making the gaussian deconvolution $^{50}\,$

$$\Gamma^2 = \Gamma_{\text{observed}}^2 - \Gamma_{\text{instrument}}^2$$
 (III.16)

where $\Gamma_{\rm instrument}$ is measured using the (220) reflection of Si as a standard. The correlation length $L_{\rm C}$ determined after applying the correction given by eq. (III.16) is illustrated as a function of x in Figure III.13 (b). Note the dramatic increase of correlation length with increasing x.

This x-dependent correlation length can be understood in terms of the differences in the solvation properties of the trimethyl ammonium and tetramethyl ammonium cations in the galleries of the host clay which provided the key to the successful synthesis of the mixed ion compounds. 16 The [(CH3)3NH+] and [(CH3)N+] exchange forms of the clay exhibit very different swelling behavior when water enters the intercrystalline gallery regions. In the [(CH₂)₂NH⁺] exchange form of the clay swelling is extensive and can be observed through gel formation at a concentration of 10wt% clay. In contrast the swelling in the $[(CH_3)_{L}N^{+}]$ exchange form of the clay is negligible due to the lack of hydration within the clay galleries. Even the wetting of [(CH $_{\rm q}$) $_{\rm A}$ N $^{+}$]-Vm with liquid water does not produce any basal spacing change. The extensive swelling and associated layer exfoliation may result in the further reduction of the clay platelet's size in [(CH₃)₃NH⁺]-rich clay. Because the exchange rates of $[(CH_3)_4N^+]$ ions are very slow with or without EDTA, mixed ion clays are synthesized by adding controlled amounts of the larger size $[(CH_3)_4N^+]$ ions to a $[(CH_3)_3NH^+]-Vm$ suspension. The addition of $[(CH_3)_L N^+]$ ions resulted in the immediate flocculation of the suspension and the concurrent replacement of some $[(CH_3)_3NH^{\dagger}]$ ions by the desired $[(CH_3)_4N^{\dagger}]$ ions. Flocculation is so

rapid that the segregation of the exchange cations into separate galleries is impeded and the mixed ions become entrapped in the same gallery. Pinnavaia has noted that in this synthesis procedure the ion exchange reaction is under kinetic control rather than thermodynamic control.

To understand the physical origin of the observed $d_n(x)$, we have simulated a model monolayer system with finite transverse layer rigidity. For simplicity we assumed that the intercalate ions are hard spheres. Starting from a two-dimensional triangular lattice of lattice constant \mathbf{a}_0 representing a single gallery with each lattice site occupied by a B ion of height $d_{\rm R}$, we randomly replace the B ions with A ions of height $d_A > d_R$. The height of a cell within a healing length λ , which is defined as the distance required to relax the local deformation of the A ion is also increased to $d_{\underline{A}}$. A second A ion in this region does not affect already expanded cells but expands unexpanded cells within λ of its location. The process of random replacement of the B ions continues to saturation. If we define $\alpha(x)$ as the fraction of cells with height d_A , then $d_n(x) = \alpha(x)$. The simulation results for $d_n(x)$ are shown in Figure III.14 for several different healing lengths. Clearly, in the floppy-layer limit λ = 0, a Vegard's-law behavior obtains whereas the initial slope $[d_n(x)]_{x=0}$ approaches infinity as λ approaches infinity. As can be seen from Figure III.14, there is no percolation threshold even for finite λ because $d_n(x)$ depends upon all of the large ions, not only on those belonging to the infinite percolation cluster. Note that the nonlineality in $d_n(x)$ for $\lambda > 0$ is a collective effect associated with the individual interaction between the larger ions through their distortion fields.

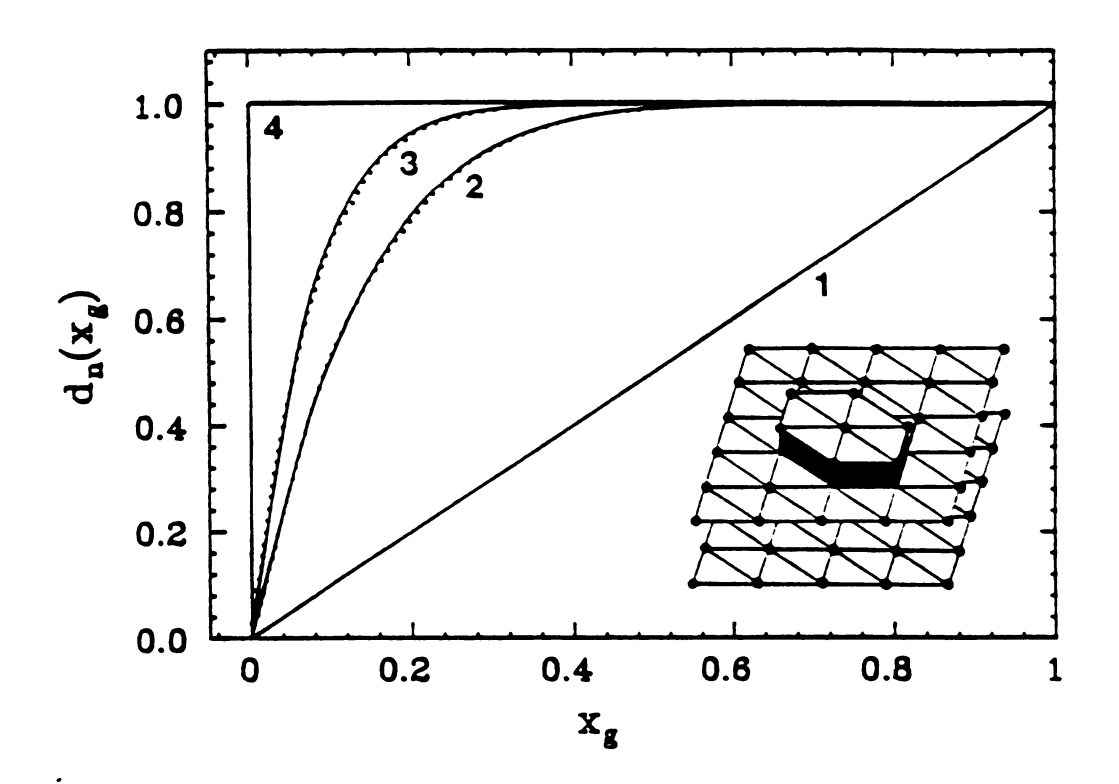


Figure III.14 Monolayer triangular lattice computer simulations (dotted lines) of the composition dependence of the normalized basal spacing of a ternary intercalation compound for several values of the healing length, λ , and rigidity parameter, p. The solid lines are from eq. (III.19) of the text with (1) p = 1, λ = 0; (2) p = 7, λ = a_0 ; (3) p = 13, λ = $\sqrt{3}a_0$; and (4) p = ∞ , λ = ∞ . Inset: The puckered region of a triangular lattice with λ = a_0 . Here the number of expanded sites is p = 2 + 1 = 7 where 2 is the number of nearest neighbors.

The sublinear x dependence and the rapid rise in $d_n(x)$ near x_t is outside the monolayer model. Several mechanisms including the relative magnitude of host-guest and host-host interactions, interlayer correlations, and the presence of the defect (d) sites can produce sublinear behavior in $d_n(x)$ but only the latter two can generate threshold effects. Since the ions of interest here are relatively incompressible we treat the guest species as hard spheres as noted above. The interlayer correlation hechanism is one in which large ions locally pucker the bounding layers so that at low x they adopt staggered lateral positions, i.e. no line joining the centers of any pair of large ions in adjacent galleries is perpendicular to the silicate layer. This mechanism is relevant to host materials with low transverse layer rigidity such as graphite while the defect-site mechanism is more appropriate to the more rigid layers of clays.

The source of defect sites in our specimens is shown in Figure III.15 which is an electron micrograph of $(CH_3)_3NH^+$ -Vm acquired with a Vacuum Generators model HB501 field-emission scanning transmission electron microscope. The region imaged consists of homogeneously intercalated areas (g sites) which are bounded laterally by layer edge dislocations and are capped by free surfaces (d-sites) that bind guest species without inducing c-axis expansion. Since the clay grains have typical basal dimensions of a few micrometers, it is clear from the scale of the micrograph that these free surfaces can represent a significant fraction of the total surface available to guest species. Additional minor sources of d sites are the microcracks and folds that are visible in the micrograph.

We have explored the d-site mechanism by constructing a two site model in which the basal spacing is assumed to depend upon the gallery



Figure III.15 A bright-field scanning-tunneling electron micrograph of

[(CH₃)₃NH⁺]-Vm acquired at T = -135°C with the electron beam normal to the layers. Note the free surface between layer edge dislocations (outline-headed arrows), the folded region (lozenges), and the microcrack (open headed arrows). The small dotted grid is an instrumental artifact.

A-ion concentration x_g which itself is a function of the total A-ion concentration x. The definitions of x and x_g are $x = (N_g^A + N_d^A) / (N_g + N_d)$ and $x_g = N_g^A / N_g$ where $N_{d(g)}^A$ and $N_{d(g)}$ are number of A-ions in the d(g)-sites and number of total ions in the d(g)-sites respectively. For simplicity we assume only one type of d-site. The functional dependence of x_g on x is determined by two parameters, f and A/kT, where $f = N_d/N_g$ is the fraction of ions in d-sites relative to those in g-sites and A is the effective binding-energy difference between these sites, the d-sites have a lower binding energy. For example at T = 0, $x_g = 0$ for $x < x_t = f/(1+f)$ because we assumed preferential exchange of A-ions with B-ions in defect sites and $x_g = (1+f)x-f$ for $x > x_t$. A statistical mechanics calculation gives

$$x_g = 1/(z+1)$$
 (III.17)

$$x = [1/(1+f)]x_{g} + [f/(1+f)]\{1/[zexp(-\Delta/kT)+1]\}$$
 (III.18)

where $z = \exp[(\epsilon_g - \mu)/kT]$ is related to the fugacity and the binding energy ϵ_g of the g-sites. Equation (III.17) and (III.18) can be solved to obtain $x_g = \phi(x, f, \Delta/kT)$ for different values of f and Δ/kT . In Figure III.16 the gallery concentration x_g is plotted versus x for $\{p = 7.0 ; f = 2.2\}$ and $\{p = 8.0 ; f = 0.5\}$, respectively. The threshold is quite pronounced at low temperature and x_g becomes more and more linear with respect to x as the temperature is increased. The temperature dependence of x_g versus x may induce a temperature dependent basal spacing variation. Physically then for $x < x_t$, the A ions first preferentially displace the B ions from the d-sites. This reduces the gallery A-ion concentration for a given x and yields a sublinear increase in $d_n(x)$. For $x > x_t$ additionally ingested A ions enter the g-sites. The result is a rapid increase in $d_n(x)$.

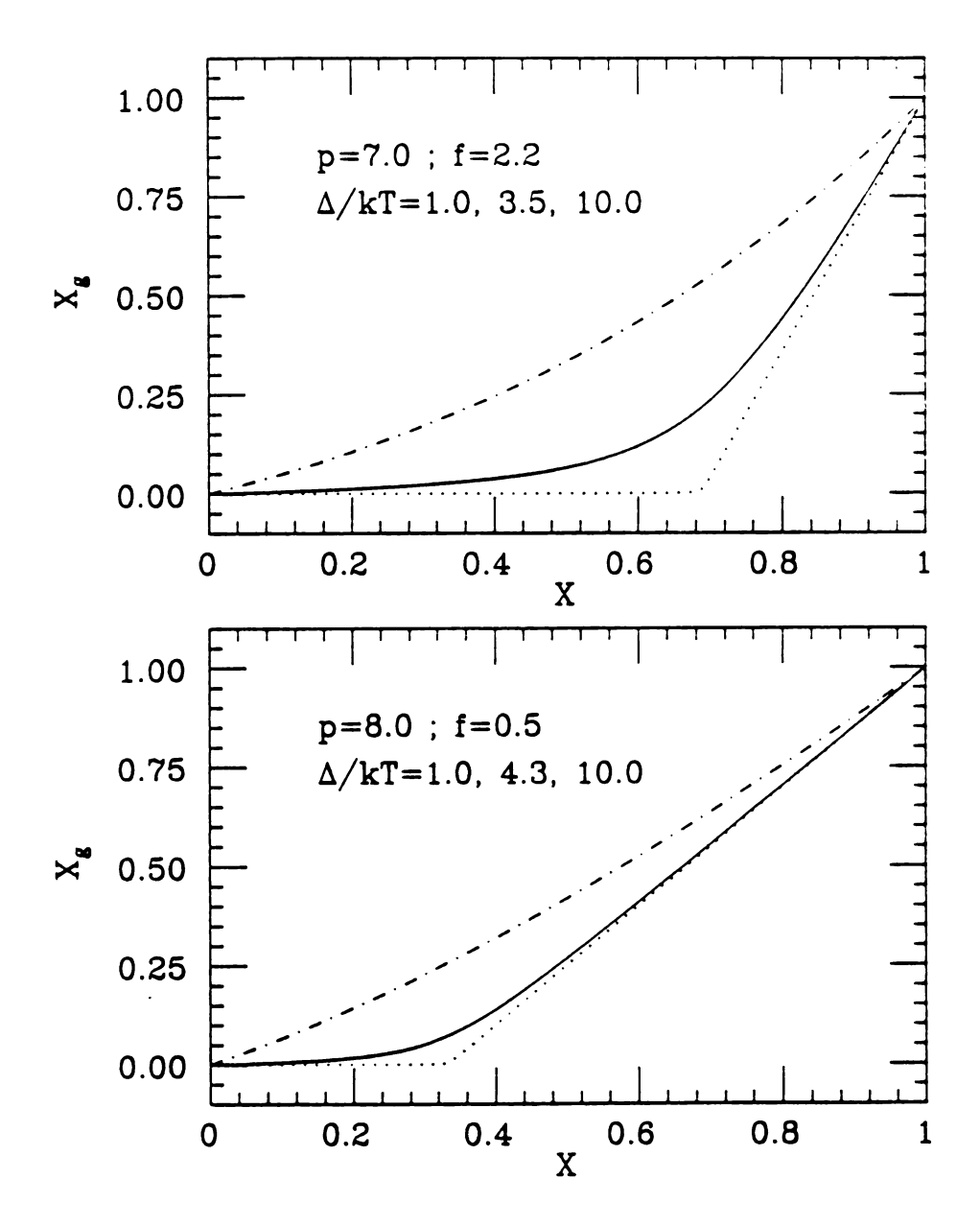


Figure III.16 The gallery concentration, x_g , plotted versus x for p=7, f=2.2; and p=8, f=0.5. Temperature increases from bottom to top: the dotted lines are for $\Delta/kT=10.0$, the dot dashed lines are for $\Delta/kT=1.0$ and solid lines are for $\Delta/kT=3.5$ and 4.3, respectively.

Using methods developed by Xia and Thorpe 51 one can obtain the following analytic solution for our monolayer simulation:

$$d_n(x_g)=1-(1-x_g)^p$$
, $0 \le x_g \le 1$ (III.19)

where p is a layer rigidity parameter. This equation fits the simulation data extremely well as shown by the dotted lines in Figure III.14. For our lattice-gas simulation, p = Z+1 where Z is the number of neighboring sites that are puckered by the insertion of an isolated A ion (see insert Figure III.14). In the continuum limit ($\lambda >> r_A$ where r_A is a radius of intercalant A), p is proportional to $(\lambda/r_A)^2$. In equation (III.19), the $(1-x_g)^p$ term means that a certain site can have a height d_B only when it and also its p neighboring sites are occupied by B-ions. Hence the layer rigidity parameter p is determined by both the healing length λ and the connectivity of the gallery sites. For example when λ is the same with the lattice parameter a_0 , p = 7 in a triangular lattice but in a honeycomb lattice p=4. Using eq. (III.19) and $x_g = \phi(x, f, \Delta/kT)$, we obtain

$$d_n(x) = 1 - \{1 - \phi(x, f, \Delta/kT)\}^p$$
 (III.20)

Note that the slope of $d_n(x)$ at $x \ge x_t$ is governed by a combination of p and Δ/kT while x_t is determined primarily by f for large Δ/kT .

We have used eq. (III.20) to obtain a nonlinear least square fits to the data of Figure III.4. The parameter values which give very good fits (solid lines in Figure III.4) for the two clay intercalation systems $[(CH_3)_4N^+]_x[(CH_3)_3NH^+]_{1-x}$ -Vm and Cs_xRb_{1-x} -Vm are {p=8.0, f=0.5, $\Delta/kT=4.3$ } and {p=7.0, f=2.2, $\Delta/kT=4.1$ }, respectively. The smaller value of the rigidity parameter in the Cs-Rb system is consistent with the fact that alkali ions in clay intercalation compounds can have a large encapsulation (See Table III.1). The encapsulation of the intercalants by the host silicate layers causes a reduction of the apparent healing

length. But the alkyl ammonium ions are much too large and the encapsulation effect is very small. Thus one expects the {Cs-Rb}-Vm system to exhibit a lower value of the rigidity parameter p. The f values deduced for the two systems also reveal interesting properties of the clay structure. For singly ionized guest species $N_{ij} = \sigma A_{ij}$ where σ is the layer charge density and $\mathbf{A}_{\mathbf{i}}$ is the surface area associated with \mathbf{j} sites, j = d,g. If A = A_d + A_g then A_d = [f/(1+f)]A and $(A_d)_{Cs-Rb}/(A_d)_{[(CH_3)_4N]-[(CH_3)_3NH]} = 2$. Thus of the surface which provides d-sites for small Cs-Rb ions only about half (the portion not adjacent to edge dislocations, or derived microcracks or folds) can also accomodate the robust (CH₃) N+-(CH₃) NH+ ions without inducing basal spacing expansion. Finally, the difference in the Δ/kT values for the two pairs indicates that the d sites are more attractive for the larger ions. This makes physical sense because the more spatially demanding ions prefer the less constrained defect environment to the more restrictive gallery. We have assumed that the site binding energies in our model are independent of concentration. This assumption might be relaxed if the binding energy of the g-sites drops once the galleries are initially expanded. The resultant transfer of ions from d to g sites would then contribute to the rapid increases in $d_n(x)$ for $x \ge x_t$.

The layer rigidity model which we have developed here should be directly applicable to other lamellar solids such as zirconium phosphates and layered niobates which have relatively rigid layers. It can also give insight into the behavior of intercalation compounds whose host layers have low or moderate rigidity. For example $\operatorname{Li}_{\mathbf{x}}^{\mathbf{C}_{6}}^{\mathbf{36}}$ and $\operatorname{Li}_{\mathbf{x}}^{\mathbf{T}_{1}}$ so exhibit no threshold in $d_{\mathbf{n}}(\mathbf{x})$, and therefore contain few if any defect sites.

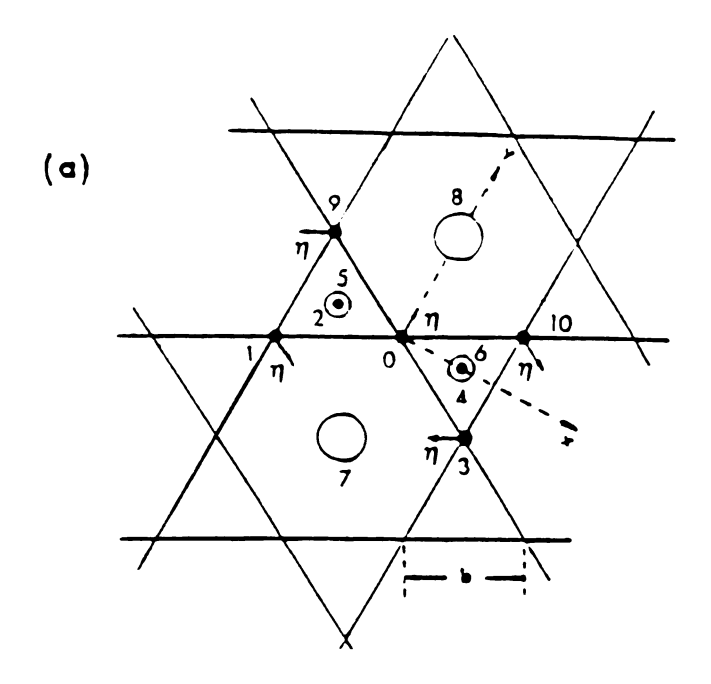
Now let us consider again the Raman active torsional mode frequency data of Figure III.5. The x-dependence of Raman torsional mode gives additional strong evidence against interstratification. If we have a system with segregated gallery ions, instead of a continuous frequency shift depicted in Figure III.5 we might observe only distinctive frequencies which correspond to the two end-members, {Cs-Vm and Rb-Vm} or {[(CH₃)₄N]-Vm and [(CH₃)₃NH]-Vm}.

For a mixed ion system, the x-dependence of the guest-host interaction is of much interest. Usually a vibrational mode can be treated as a harmonic oscillation about the equilibrium position so the structure of the solid (e.g. the basal spacing) determines the static equilibrium conditions of the interaction between constituents. Hence a study of the torsional mode using a harmonic expansion around the potential minimum is especially attractive because we already know the composition dependence of the basal spacing. The following calculation has been done using the virtual crystal approximation in which we have neglected the actual cation distribution and have instead assumed a uniform average basal spacing with an average guest-host interaction. In addition we have assumed that in the torsional modes the SiO₄ tetrahedra are undistorted. We have considered only nearest neighbor interactions with a Lennard-Jones type two-body potential

$$U_{i}(r) = -\frac{A_{i}}{r^{6}} + \frac{B_{i}}{r^{1}2}$$
 (III.21)

where i = 0-0, Si-0, and M-0 (intercalant-oxygen).

In Figure III.17 we showed the configuration of the clay host and guest ions viewed in the direction (a) along and (b) perpendicular to the c-axis. The oxygen atom labeled as "0" has ten nearest neighbors and an equilibrium potential energy given by



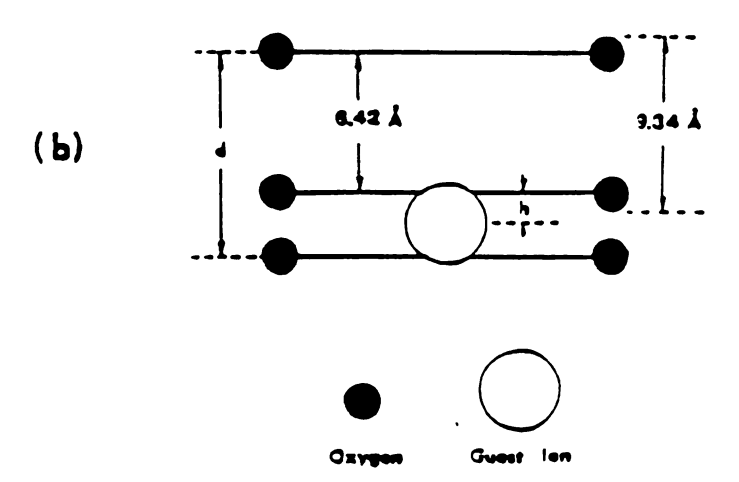


Figure III.17 The configuration of the host layer and guest ions viewed in the direction (a) along and (b) perpendicular to the c-axis. The arrows indicates the displacements in the torsional mode.

$$v_{\text{eq}}^{0} = v_{0-0}(1) + v_{0-0}(3) + v_{0-0}(3) + v_{0-0}(4) + v_{\text{Si-0}}(5) + v_{\text{Si-0}}(6) + v_{\text{M-0}}(7) + v_{\text{M-0}}(8) + v_{0-0}(9) + v_{0-0}(10) \quad \text{(III.22)}$$

where the integers represent equilibrium positions. In the torsional mode indicated by the arrows in Figure III.17 (a) there is a rotation of the SiO₄ tetrahedra about the Si-O axis such that the atoms are displaced from their equilibrium positions by the vector $\vec{\eta}$. The linear combination of these vectors shown in Figure III.17 (a) is then the eigenvector of the torsional mode. For this mode the potential energy is given by

$$V^{0} = V_{eq}^{0} + \Delta U_{M-O}(7, -\eta) + \Delta U_{M-O}(8, \eta)$$

$$= V_{eq}^{0} + \left[6A_{M-O} \frac{(h^{2} - 7b^{2})}{(b^{2} + h^{2})^{5}} - 12 B_{M-O} \frac{(h^{2} - 13b^{2})}{(b^{2} + h^{2})^{8}} \right] \eta^{2} + O(\eta^{4})$$

$$= V_{eq}^{0} + \frac{1}{2}k\eta^{2} + O(\eta^{4})$$
(III.23)

where h = (d - 6.42)/2 (Å) is the distance along the c-axis between the center of the guest ion and the basal plane and b = 2.67 Å is one of the inplane lattice parameters (See Figure III.17). With the assumption that the intercalant species reside at the center of the hexagonal pocket and from $\frac{\partial V}{\partial h}|_{dexp} = 0$ we find

$$B_{M-0} = A_{M-0}(b^2 + h^2)^3/2$$
 (III.24)

Then

$$\Delta U_{M-O}(7,-\eta) + \Delta U_{M-O}(8,\eta) = \frac{1}{2}k\eta^2 + O(\eta^4)$$

$$= 36A_{M-O} \frac{b^2}{(b^2+h^2)^5} \eta^2 + O(\eta^4)$$
 (III.25)

Hence the torsional mode frequency ν is given as

$$v = \left(\frac{72b^2}{4\pi^2 mc^2}\right)^{1/2} \left[\frac{A_{M-0}}{(b^2+h^2)^5}\right]^{1/2}$$
 (III.26)

$$A_{M-0} = 4\pi^2 mc^2 \frac{(b^2 + h^2)^5}{72b^2} v^2$$
 (III.27)

where m is the mass of the oxygen atom and c is the speed of light. In Figure III.18 the normalized values of A_{M-O} calculated from eq. (III.27) using the experimentally measured torsional frequencies ν and basal spacings d are plotted as a function of $\mathbf{x}_{\mathbf{g}}$ for two vermiculite intercalation compounds. The variation of the normalized $\mathbf{A}_{\mathbf{M}=\mathbf{O}}$ is quite similar to the variation of d_n (See Figure III.14). Thus we can fit the normalized A_{M-0} with the same functional form; $1-(1-x_g)^q$, even though the exponents q are different from the exponent obtained from fits to $d_n(x_q)$. From such a fitting we have obtained q = 5.38 for the Cs-Rb system (open squares) and q = 5.39 for the alkylammonium system (open circles). The solid line in Figure III.7 is a fit to the experimental data using q = 5.39 for Cs_Rb_{1-x} -Vm which is the more appropriate system for our virtual crystal approximation because of its small size and small polarizability differences in the questions. The close relationship between the composition dependence of the basal spacing and of the gallery ion-oxygen interaction coefficient ($A_{M-\Omega}$) is very interesting and clearly indicates the importance of the guest-host interaction in determination of layer rigidity in the intercalated layered compounds.

III.4 Summary and Concluding Remarks

In this chapter we have discussed the cation distribution state of new synthetic vermiculite intercalation compounds. From much evidence including the continuous x-dependent shift of the torsional mode, a Patterson synthesis, the evolution of the FWHM, the sigmoidal shape of

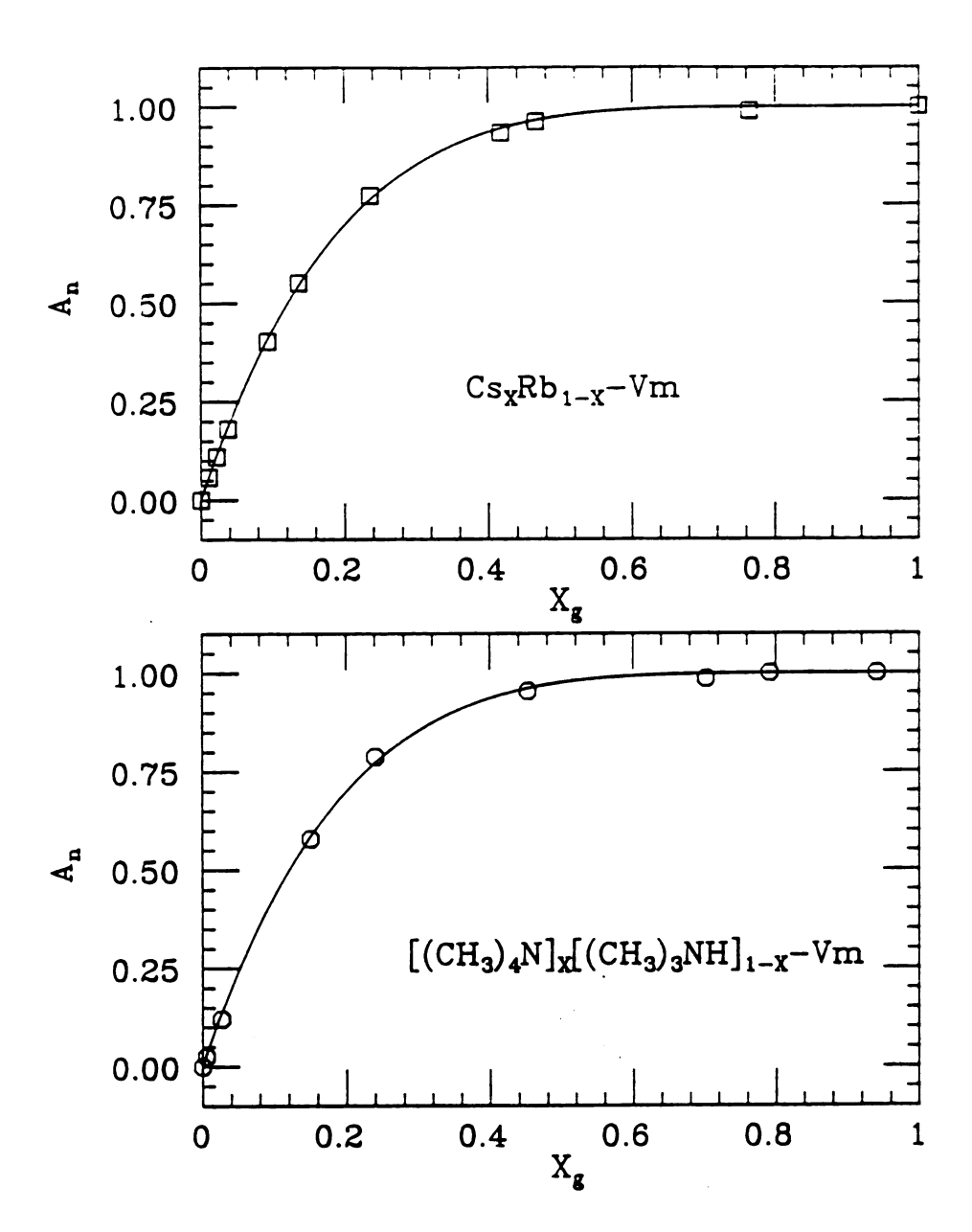


Figure III.18 The normalized values of A_{M-O} of Cs_xRb_{1-x} -Vm (open squares) and $[(CH_3)_4N^+]_x[(CH_3)_3NH^+]_{1-x}$ -Vm (open circles), calculated from eq. (III.27) using the experimentally measured torsional mode frequencies and basal spacings, are plotted versus x_g . The solid lines are fits to the data using the function $1 - (1 - x_g)^q$ with q = 5.38 (upper panel) and 5.39 (lower panel), respectively.

the basal spacing variation, the Q-plot, and a direct comparison of a computer generated Hendricks-Teller diffraction pattern with experimental results, we have excluded the possibility of interstratification. All available evidence supports the solid solution type of mixed ion distribution in these new compounds.

From the pill-box model computer simulation we have shown step-like, superlinear, and Vegard's-law type basal spacing variation for the different limits of healing length λ which is the distance required to relax a local deformation. With the introduction of a rigidity parameter p we can quantify layer rigidity in terms of the experimentally measured basal spacing for many different layered compounds. The application of this layer rigidity model to nonclay layered compounds will be discussed in the next chapter.

Because of the fixed layer charge density of the silicate layer in clay intercalation compounds and their high transverse layer rigidity we suggest that defect sites are the source of sigmoidally shaped basal spacing change exhibited by the guest species (in vermiculite) discussed here. Using field emission scanning transmission electron microscopy we have shown direct evidence of the presence of such defect sites. From the two site model we have calculated $\mathbf{x}_{\mathbf{g}}$, the concentration of A-ions contributing to the expansion of the basal spacing, as a function of \mathbf{x} , and $\mathbf{\Delta}/\mathbf{k}T$

Finally under the virtual crystal approximation, we have calculated the guest ion-oxygen interaction coefficients, \mathbf{A}_{M-O} , in the Lennard-Jones type potential. The similar \mathbf{x}_g dependence of the normalized values $\mathbf{A}_{M-O}(\mathbf{x}_g)$ and $\mathbf{d}_n(\mathbf{x}_g)$ suggest the importance of the gallery ion-host interaction in dynamic and static properties of intercalated layered compounds.

IV. Elastic Effects in Intercalated Layered Compounds.

IV.1. Introduction

In layered solids many physical properties are determined by the rigidity of the pristine layers. One typical example is a composition-dependent basal spacing variation. All crystalline solid solutions exhibit a composition-dependent unit cell volume which generally increases with the concentration of the large constituent. 55 When this variation is linear the system is said to obey Vegard's law. 56 Most solid solutions exhibit a more complex nonlinear behavior 57 which has been accounted for empirically by augmenting Vegard's law with a polynomial that represents a composition-dependent mixing volume. In order to gain a more fundamental understanding of the origin of non-vegard's law behavior several authors 35,36,61 have found it advantageous to address systems which contain crystalline solid solutions of reduced dimensionality. For instance, there are a variety of ternary layered intercalation compounds of the form $A_{1-x_g} B_x L$, $0 \le$ x_{σ}^{\leq} 1, where B is the larger ion and $x_{\sigma}^{}$ defines the composition of the ions which actually reside in the gallery and contribute to c-axis expansion. The guest species, A and B form a 2D commensurate but compositionally disordered solid solution between the host layers, L. 58,59,60 Note that A can represent a vacancy (i.e. A = Va). Because of the highly anisotropic structural and physical properties of ternary layered intercalation compounds, 58,59,60 the dominant change in their cell volume with intercalate composition results from c-axis expansion. The one dimensional form of Vegard's law is then

$$c(x_g) = (1 - x_g)c_A + x_gc_B$$
 (IV.1)

where c, c_A , and c_B are the c-axis repeat distances of the mixed and end-member compounds. But most ternary intercalation compounds exhibit a superlinear (concave downward) $c(x_g)$. 35,36,58,59,60 Even though ternary layered intercalation compounds represent the most basic and simplified (e.g. 1D) systems for studying composition-driven lattice expansion, attempts to account for their nonlinear response have to date been markedly unsuccessful. Using the "Layer Rigidity Model." which has been developed in section III.3, we rectify this deficiency and present in this chapter a one-parameter model which accounts for the c-axis expansion of a broad range of ternary layered intercalation compounds. A healing length λ and a rigidity parameter p are used to quantify and parameterize layer rigidity.

In Safran's model of staging, ^{19,61} competition between repulsive interplanar interactions and attractive intraplanar interactions is responsible for staging. Safran and Hamann ^{62,63} attributed the long-range repulsive interaction in graphite intercalation compounds to the effective electrostatic repulsion between intercalant layers with anomalously long-range screening. In contrast to Safran and Hamann, Ohno and Kamimura ⁶⁴ claimed that this interaction is not so strong because of the extremely inhomogeneous c-axis charge distribution. They also suggested the dominance of the stronger but short-ranged elastic repulsion. The elastic deformation of the host layer by the intercalant atoms is one source of the attractive intralayer interaction in layered intercalation compounds. To model these interactions with elastic origin, many authors ^{20,65,66} treated the intercalant atoms as pairs of elastic dipoles which separate the layers. Since each one generates host layer deformation, it is favorable for two dipoles in the same gallery

to be adjacent to each other, implying an attractive intralayer interaction.

Safran¹⁹ took the simplest form for the attractive intralayer interaction as a quadratic function of the in-plane density; $U(\sigma) = -U_0\sigma^2$ where $U_0 > 0$ is an effective two-body interaction obtained in the mean-field approximation. The model Hamiltonian becomes, after in-plane averaging,

$$H = - \mu \sum_{i} \sigma_{i} - \frac{1}{2} U_{0} \sum_{i} \sigma_{i}^{2} + \frac{1}{2} \sum_{ij} V_{ij} \sigma_{i} \sigma_{j}$$
 (IV.2)

where i is a layer index, $V_{ij} = V_0 |i-j|^{-\alpha} > 0$ is the average interlayer interaction energy, μ is the chemical potential and σ_i is the fractional occupation of the ith layer, which may take continuous values between 0 and 1. Then one of the main results of Safran's model is the prediction of a limiting temperature T_m above which only stage 1 is stable. Figure IV.1 shows Safran's phase diagram plotted as a function of temperature and concentration. Note that this phase diagram is universal independent of host because the temperature is scaled by U_0 which surely depends on the host properties. 19,36

Though Safran's phase diagram was successful in predicting many features confirmed by experiment, it also showed some features including the symmetry about $\mathbf{x}=1/2$ due to the quadratic form for the in-plane interaction which were not observed in experiments. ³⁶ Several attempts have been made to modify Safran's original lattice-gas model in order to make it more realistic and physically plausible. For example, Millman and Kirczenow ^{67,68,69} introduced the concentration independent cleavage energy γ for separating the host layers and used $U(\sigma) = -\epsilon Z\sigma^2 + \gamma\theta$ where $\theta = 1$ if $\sigma > 0$ and $\theta = 0$ for $\theta = 0$, to account for the nonlinear elastic effects which are important in the intraplanar energy. The modified form of $U(\sigma)$ used by Divincenzo and Koch ⁷⁰ is $U(\sigma) = -U_0\sigma^2 + \Delta U(\sigma)$ where

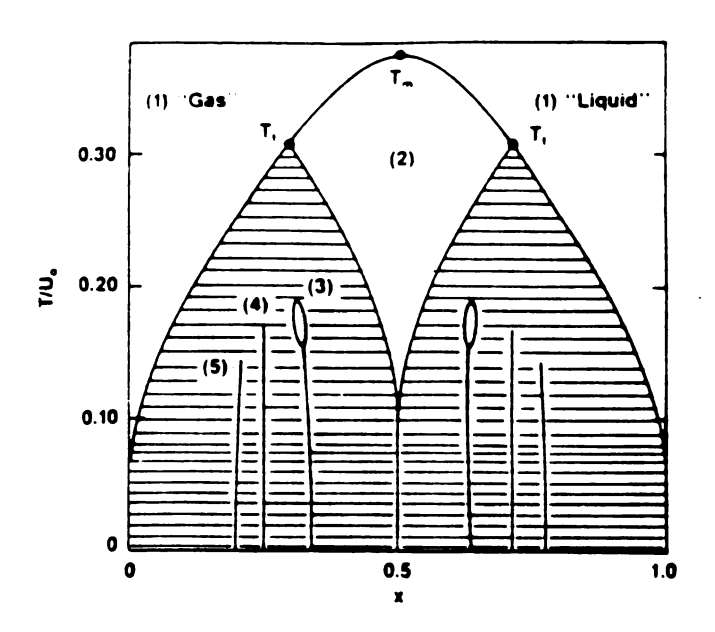


Figure IV.1 Safran's phase diagram plotted as a function of temperature and concentration. The pure-stage states and two-phase regions are denoted by the integers and cross-hatched regions, respectively. T_t is the tricritical temperature and T_m is the maximum temperature discussed in the text.

 $\Delta U(\sigma)$ is the "corrugation energy" term. Even though these Hamiltonian's produced more realistic phase diagrams, surprisingly they have not been used to account for other physical properties of intercalated layer solids.

Another modification of the lattice gas model was made by Dahn and coworkers. The model used by Dahn et al³⁵ includes nearest neighbor interactions between intercalant atoms in the same layer and interactions between atoms intercalated in the first and second neighboring layers together with a site energy \mathbf{E}_0 and the elastic energy. In calculating the elastic energy contribution, Dahn and coworkers treated the host layers as infinitely rigid undeformable planes held together by harmonic springs. In Figure IV.2 the springs of spring constant k with equilibrium length \boldsymbol{c}_{L} and spring constant \boldsymbol{K} with equilibrium length $\mathbf{C}_{\mathbf{C}}$ represent, respectively, the guest-host and the host-host interactions. Even though they constructed a reasonable phase diagram in the T-x plane (where x is the intercalant concentration) and were able to explain the voltage-charge relation, V(x), and inverse derivative of the voltage-charge relation, $-\partial x/\partial V$, of Li/Li_TiS₂ electrochemical cells from the Monte Carlo simulations of their Hamiltonian, their model could not quantitatively account for the full x-dependence of the c-axis repeat distance of any intercalated layered solid.

In an effort to improve upon the rigid layer model Jin and Mahanti³⁴ introduced a model with nondeformable layers but with additional springs which represented the finite compressibility of the guest species. Their model addressed: (a) the different conditions under which one can see Vegard's-law behavior, (b) the different compressibility ratios of the guest species and the effect on the

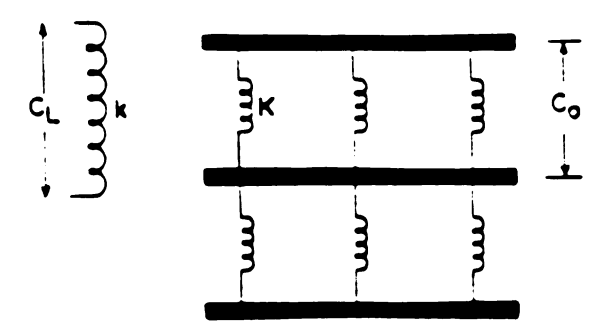


Figure IV.2 The rigid layer model used by Dahn et al. The host layers are treated as undeformable and the guest-host and host-host interactions are represented by the harmonic springs of strength k with length $\mathbf{C_L}$ and strength K with length $\mathbf{C_0}$, respectively.

composition dependence of the interlayer spacing, and (c) the interlayer correlations. Nevertheless, even though this model employed several parameters, its success was marginal when it was applied to the dual alkali graphite intercalation compounds of the type $\mathbf{M}_{1-\mathbf{x}}\mathbf{M}_{\mathbf{x}}\mathbf{C}_{8}$ for which interlayer correlation should be most pronounced in $\mathbf{d}_{n}(\mathbf{x})$. [We do not address the dual-alkali graphite intercalation compounds because the gallery composition of these materials has not yet been established and the actual form of $\mathbf{d}_{n}(\mathbf{x}_{g})$ is therefore unknown.] Moreover, their multiparameter model does not provide a satisfactory fit to the data of Figure IV.3.

Another way to model the elastic interaction is by the local deformation of the host layers. With finite layer rigidity, one can imagine that when intercalants are introduced, the gallery height between two host layers will be different from the pristine host material because the host layers are locally deformed at an occupied site. The actual composition dependence of the c-axis repeat distance will determine how these deformation is relaxed away from the locally expanded sites. This is our Layer Rigidity Model.²⁷

The essential feature of the layer rigidity model is the deformability of the host layers which in its discrete version is characterized by a rigidity parameter, p. Here we also introduce a continuum version which is characterized by a healing length, λ and we derive a relation between p and λ which provides an independent test of the model when the host elastic constants or phonon dispersions are known. In continuum theory, the intralayer (or inplane) interaction energy between intercalants, \mathbf{U}_0 , can be calculated for the commensurate intercalant system in terms of rigidity constants and the force that generates layer deformation using mean-field theory. The dependence of

the intralayer interaction upon the layer rigidity is a key to the understanding of the different staging behavior among the three different class of layered solids. Also its dependence on the deformation generating force can lead us to understand the trends with intercalant size in a given host.

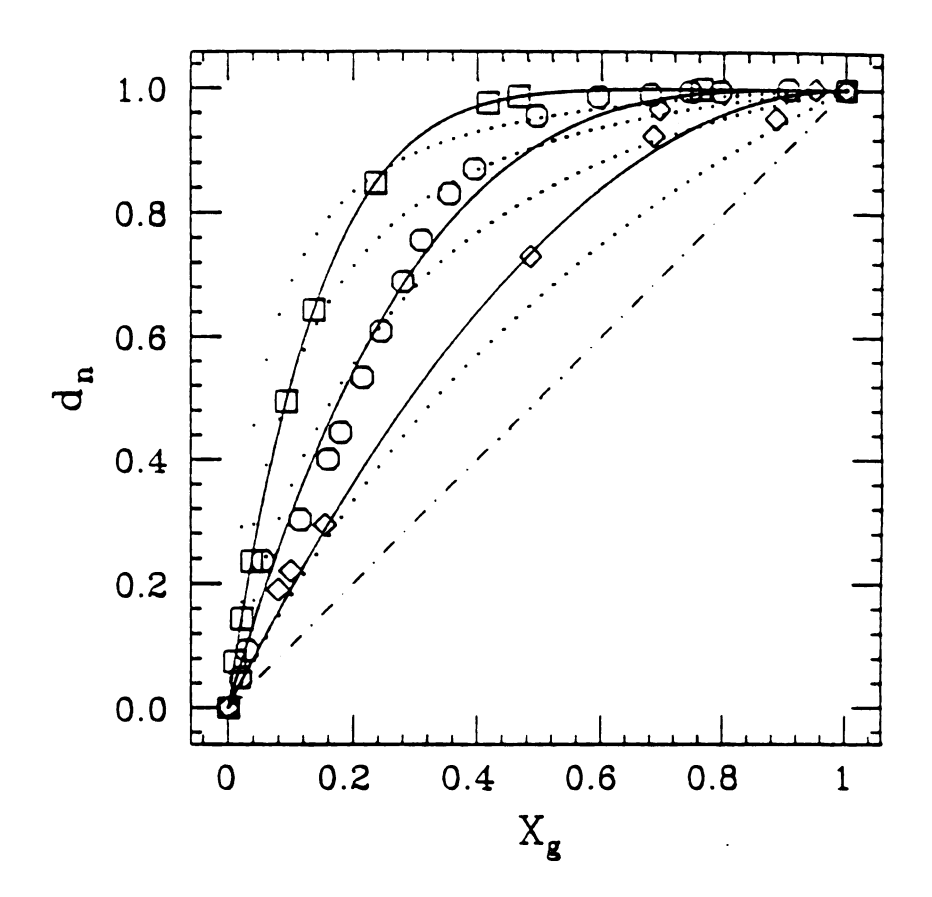
IV.2 Composition dependent C-axis Expansion

In Figure IV.3 we show the measured composition dependence of the normalized basal spacing, $d_n(x_g)$, for $Va_{1-x_g}Li_{x_g}C_6$, $^{36}Va_{1-x_g}Li_{x_g}TiS_2$, and $Rb_{1-x_g}Cs_{x_g}Vm^{27,30}$ which represent, respectively, the class I, II and III layered compounds. All three ternary layered intercalation compounds exhibit a superlinear non-Vegard's law behavior. Although these three classes of ternary intercalated layered compounds exhibit a broad range of physical properties, the graphite, TiS_2 and Vermiculite hosts possess a common structural feature: their guest sites can form a 2D triangular lattice.

In their effort to explain the c-axis expansion of ${^{Va}}_{1-x}{_g}^{Li}{_x}_g^{TiS}_2$ employing an undeformable layer with two kinds of spring Dahn and coworkers 35 obtained

$$d_n(x) = x / (\alpha + x)$$
 (IV.3)

where α = K/k, by equating the forces between the expansion of the host layers due to the intercalant which is modeled by a spring of equilibrium length c_L and strength k and the separation of the host layers due to their intrinsic interaction which is modeled by a spring of equilibrium length c_0 and strength K (hereinafter called the Rigid Layer Model in contrast of our Layer Rigidity Model). However, this



result neglected anharmonicity of the host bonding. Safran⁶¹ suggested a modification of the original rigid layer model to account for anharmonic softening of the vacancy springs in the presence of the guest springs, which implies that the intercalant has completely weakened the host-host bonds once there is local separation of adjacent layers. Then the rigid layer model yields

$$d_n(x_g) = x_g / [(1 - x_g)\alpha + x_g]$$
 (IV.4)

which satisfies the boundary conditions $d_n(0) = 0$, $d_n(1) = 1$ and gives Vegard's law behavior when $\alpha = 1$. Plots of the modified rigid layer model for several values of α are shown in Figure IV.3. It is evident from these plots that the rigid layer model fails to fit the measured $d_n(x_g)$ for any of the ternary layered intercalation compounds. This is not surprising for graphite or even for TiS₂ since their host layers are far from rigid. But the model also fails for the Rb_{1-x_g} Cs_{x_g} Vm system to which it should be most applicable given its high host layer rigidity. 13

We now discuss our layer rigidity model²⁷ introduced in section III.3. Unlike all previous models this one accounts for the data of Figure IV.3 and does so with the introduction of only one parameter. Consider a single gallery bounded by a pair of host layers. Guest ions whose relative proportions depend on x randomly decorate the sites of a 2D triangular lattice. The layers experience a pillbox-like discrete puckering over the larger B ion. The lateral extent of this puckering is specified by p which is equal to the total number of puckered lattice sites for a single B ion.

In Figure IV.3 the solid lines represent fits to the data using eq. (III.19). With the exception of the Va_{1-x} Li $_{g}$ TiS $_{g}$ system the fits are excellent and far superior to those obtained using the rigid layer

model. Even in the case of TiS₂ compounds, the deviation of eq. (III.19) from the data is small and the fit is still superior to the rigid layer model result. The rigidity parameters deduced from the fits to the data in Figure IV.3 are given in Table IV.1 and as expected increase from class I to class III ternary layered intercalation compounds.

Our layer rigidity model can account for the four functional forms of $d_n(x)$ namely linear (Vegard's law), superlinear, sublinear and sigmoidal. The linear and superlinear forms are shown in Figures III.14 and IV.3, but the sublinear and sigmoidal forms are outside the monolayer model. In section III.3, the sigmoidal form exhibited by vermiculite compounds has been attributed to the defect-site model²⁷ and in hosts with low transverse layer rigidity such as graphite to interlayer correlations.^{27,34} Examples for each functional form of $d_n(x)$ and the models applied to fit these forms are given in Table IV.2.

To show the stiffness of the host layer with respect to transverse distortions it is desirable to relate p to a healing length which is a measure of the lateral range over which a puckered layer returns to its undistorted form when the large ions are widely separated ($x_g = 0$). The healing length, λ_d , for the discrete layer rigidity model can be simply estimated from the relation $p = (\pi \lambda_d^2)/\alpha A_0$ where the numerator is the area of the puckered region, α is the ratio of the area per site of the saturated ($x_g = 1$) superlattice to the area per host site [for Li $_{x_g}$ C6 the superlattice is $(\sqrt{3}x\sqrt{3})R30^\circ$ so $\alpha = 3$]. If a_0 is the host lattice intersite distance than $\lambda_d = [1/(3.63)^{1/2}](\alpha P)^{1/2}a_0$. The values of p, α and a_0 are given in Table IV.1 where the resultant discrete version healing lengths are also given; $\lambda_d(Li_xC_6) = 3.16A$, $\lambda_d(Li_xTiS_2) = 3.35A$ and $\lambda_d(Rb_{1-x}Cs_xVm) = 7.42A$. The fact that the host layer distortions fall off slowly in the order of graphite, TiS2 and Vermiculite is

Table IV.1. Important Parameters for Several Ternary Layered Intercalation Compounds.

Stage and			Rigidity Site Parameter Ratio	Site Ratio	In Di	Healing Lengths	ing ths
structure	28.810	ardmac	L	8	(v) ⁰	(v) ^P v	$(\mathbf{v})^{2}$ $(\mathbf{v})^{p}$
Stage	-	Val-xLixG	7	e	2.46	3.16	2.45
Triangular	11	Val-x LixTiS2	3.5	1	3.41	3.35	2.60
	111	Rb _{1-x} Cs Vm	۲	-	5.34	7.42	5.77
Stage-2	111	Va2-x (H2) x KC24	4.8 (6.9)	•	J12(2.46)	•	•
	111	Va _{2-x} (D ₂) _x KC ₂₄ 5.0 (24.8) ³	5.0 (24.8)	.	JIZ(2.46)	•	

The class designation of this compound is based on the fact that the ${
m KC}_{24}$ "host layers consist of 3 atomic planes (see text).

The bracketed number is the measured value and the unbracketed number is the actual (corrected) value (see text).

This value is based on a stoichiometric K/C ratio of exactly 1/24.

Table IV.2 Four types of basal spacing variation of layered solids.

Behavior	System	Model	Comments
Superlinear	LixC6 and LixTiS2	* RL LR	Poor fit Good fit
	K(NH ₃) _x C ₂₄	RL RL+Electr. Effect LR	Poor fit Excellent fit Excellent fit
	K(H ₂ ,D ₂) _x C ₂₄	RL **Imperical(1-e ^{-αx}) LR	Very poor fit Excellent fit Excellent fit
Sigmoidal	M' _{1-x} M _x C ₈	## LR + Interlayer corr.	Good fit
	A _{1-x} B _X -Vm	*** LR + Defect Sites	Excellent fit
Sublinear	Not been observed	RL LR	Both could yield shape
Linear	M'1-xMxC8	*** Any model	Excellent fit

Where RL and LR represent Dahn's rigid-layer model and our layer rigidity model, respectively. See ref. 35 and 36 for (*), ref. 28 for (#), Ref. 74 for (**), Ref 34 for (##) and ref. 27 for (***).

consistent with the intuitive picture of layer stiffness based on the atomic arrangements of the host layer.

To more precisely quantify the influence of layer deformation on c-axis expansion we treat the host layers as an elastic continuum in the form of a deformable plate of finite thickness. For a single point-like B ion at \vec{r}_0 in a gallery of vacancies or A ions, the gallery height, $W(\vec{r} - \vec{r}_0)$, is obtained from 71,72

$$\{D\nabla^4 - K\nabla^2 + G\}V(\vec{r} - \vec{r}_0) - f_0\delta(\vec{r} - \vec{r}_0)$$
 (IV.5)

where D is the flexural rigidity, K is the transverse rigidity, G is the c-axis compressibility, and f_0 represents the δ -function like force from the B ion. The first term in eq. (IV.5) is due to the bending energy of a plate with a thickness 2H, the third term reflects the attractive interaction between two parallel plates with a equilibrium separation d and the second term is the contribution from the transverse shear modulus whose effects are most dominant in the class III compounds. The second and third terms are especially sensitive to the guest-host interaction. Each of the coefficients in the brackets in eq. (IV.5) can be expressed in terms of the effective layer thickness, 2H, the basal spacing, d, and the host elastic constants, c_{ij} . Thus

$$D = 2[(c_{11}^2 - c_{12}^2)H^3]/3c_{11}, \qquad (IV.6)$$

$$K = dc_{LL}, (IV.7)$$

and

$$G = 2c_{33}/d.$$
 (IV.8)

Equation (IV.4) can be solved to give

$$W(\rho) = \frac{f_0}{2\pi\sqrt{DG}} \int_0^{\infty} \frac{qJ_0(q\rho/l_0)}{q^4 + 2\zeta q^2 + 1} dq$$
 (IV.9)

where $\rho = |\vec{r} - \vec{r}_0|$, $\ell_0 = (D/G)^{1/4}$ gives the length scale and $\zeta = K/[2(GD)^{1/2}] \le 1$ gives the relative strength of the transverse rigidity.

For a single defect, we can define the healing length $\lambda_{_{\hbox{\scriptsize C}}}$ as the distance at which the gallery height relaxes to half its maximum value i.e. $W(\lambda_c) = 1/2[W(0)]$. From eq. (IV.9) we obtain $\lambda_c(\zeta) = Z(\zeta)l_0$ where $Z(\zeta)$ is a slowly decreasing function of ζ . In Figure IV.4 $Z(\zeta)$ is plotted versus ζ where Z(0) = 1.302, Z(0.5) = 1.276. One can obtain λ_c from ζ and ℓ_0 . These are functions, respectively of D, K, and G the first two of which can be determined from the in-plane TA dispersion of layered solids given by $\omega^2(q) \propto Dq^4 + Kq^2$. This phonon dispersion for small q was previously recognized by Komatsu in his graphite specific heat study, 71 and experimentally observed by Nicklow et al 77 and Zabel et al 78 from inelastic neutron scattering. In Figure IV.5 the phonon dispersion curve of pyrolytic graphite obtained by Nicklow and coworkers is shown. Since for graphite, K = 0 the transverse acoustic (TA) branch features an $\omega = D^{1/2}q^2$ dependence from which D can be obtained directly. Alternatively, D can be obtained from the stiffness constants as can K and G if H is known. For graphite K and G are found from the known basal spacing and reported c_{ij} 's. Using $c_{44} = 0.5 \times 10^{11} \text{ dyn/cm}^2$, $c_{33} = 3.65 \times 10^{11} \text{ dyn/cm}^2$ 10^{11} dyn/cm², and d = 3.35Å we estimate K = 931.6 °K/Å² and G = 1578 $^{\circ}$ K/ 4 . Phonon dispersion yields D = 7076 $^{\circ}$ K. From these values we get l_{0} = 1.4552, ζ = 0.1394 and $Z(\zeta)$ = 1.2934. Using $\lambda_{\rm C}(\zeta)$ = $Z(\zeta) \ell_0$ we find $\lambda_{\rm C}$ = 1.88Å in reasonable agreement with the value 2.45Å obtained from the experimental value of p (See Table IV.1 and the following discussion).

For most layered materials, neither the elastic constants nor the phonon dispersions are available. Therefore, it is useful to derive a relationship between $\lambda_{\rm C}$ and p by extending the continuum theory to the case of a dilute distribution of B ions. Using the superposition

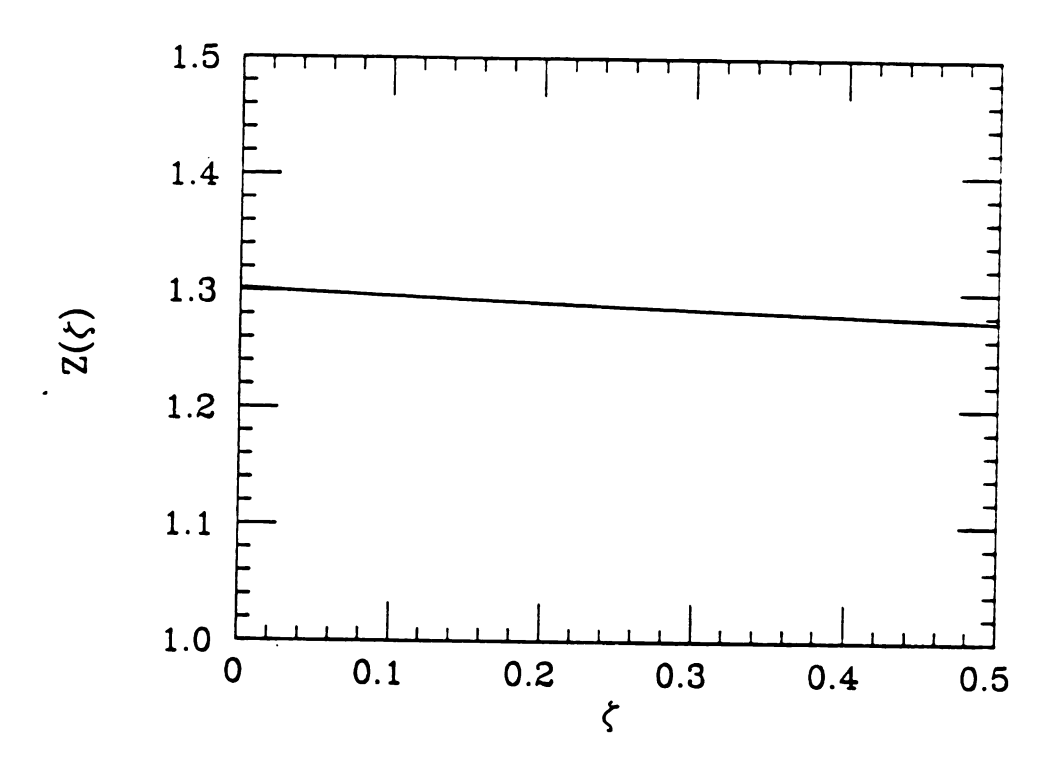


Figure IV.4 The ζ dependence of Z where $\zeta = K/[2(GD)^{1/2}] \le 1$ gives the relative strength of the transverse rigidity. $Z(\zeta)$ is a slowly decreasing function of ζ .

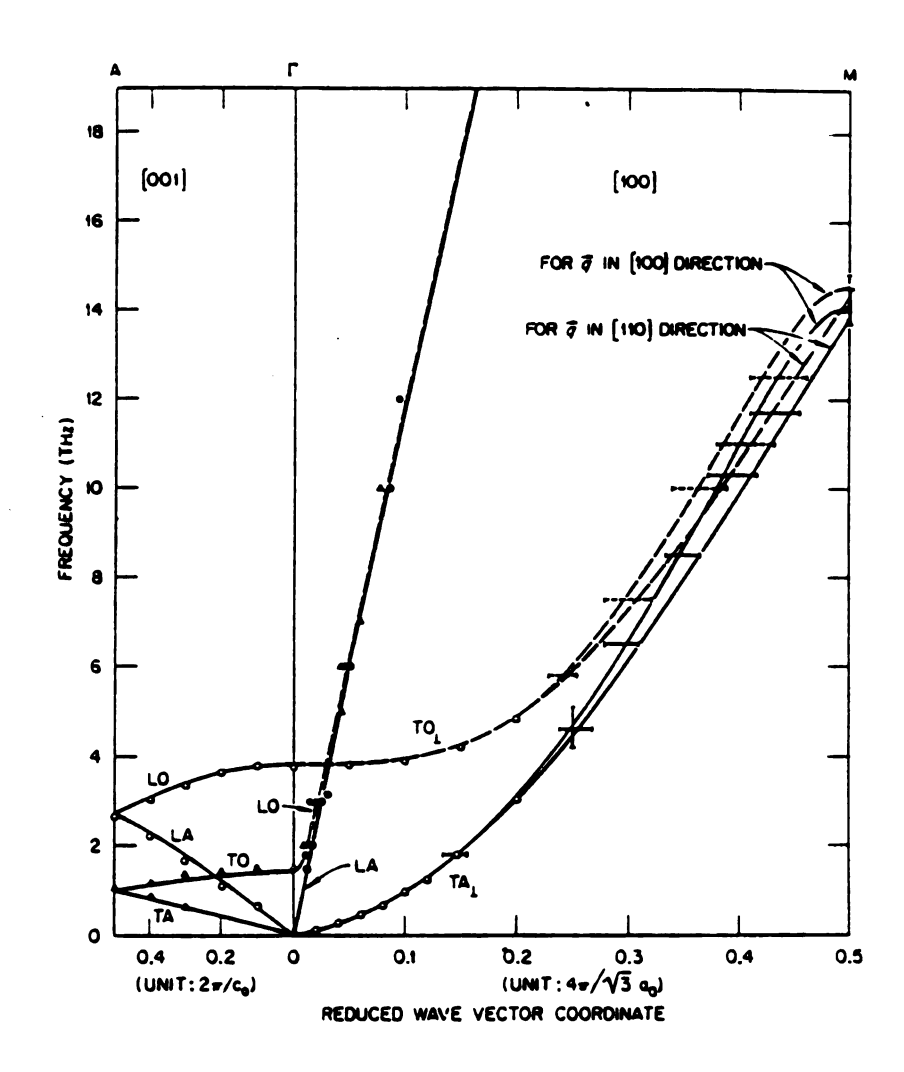


Figure IV.5 The phonon dispersion of pyrolytic graphite. ⁷⁷The TA branch shows $\omega^2(q) = Dq^4 + Kq^2$, K = 0, at small q.

principle, we can obtain the average gallery height, <W>, as a function of the concentration of $\mathbf{x}_{\mathbf{g}}$. In the limit $\mathbf{x}_{\mathbf{g}} << 1$ the result for <W> normalized by the maximum gallery height, $W(\rho = 0)$ due to a single B ion yields

$$d_{n}(x_{g}) = \alpha g(\zeta) \left[\lambda_{c}(\zeta)/a_{0}\right]^{2} x_{g}$$
 (IV.10)

where $g(\zeta)$ is given by

$$g(\zeta) = \frac{16}{\sqrt{13}} \frac{(1 - \zeta^2)^{1/2}}{1 - (2/\pi) \tan^{-1}[\zeta/(1-\zeta^2)^{1/2}]}$$
 (IV.11)

By comparing eq. (IV.10) with eq. (III.19), we have

$$\lambda_{c}(\zeta) = a_{0} \left[\alpha P/g(\zeta)\right]^{1/2}$$
 (IV.12)

The values of $\lambda_{\rm C}(\zeta)$ thus evaluated for stage-1 ternary layered intercalation compounds compare reasonably well with those of $\lambda_{\rm d}$ (see Table IV.1). Note that $\lambda_{\rm C}$ for a defect of finite size should be somewhat larger than that of a point object. Here the value of ζ is assumed to be the same as for graphite (0.14) in the cases of ${\rm TiS}_2$ and Vermiculite. The short healing length found for graphite is consistent with the results of X-ray studies of disordered alkali graphite intercalation compounds 73 which indicate that the host potential is strongly modulated in the vicinity of a guest ion.

Since the charge on the host layers in class III ternary layered intercalation compound is fixed their c-axis expansion is purely elastic. However, the success of the layer rigidity model for the class I and II intercalation compounds is an indication that charge exchange has a small effect on host layer stiffness. If this were not so, p would be composition-dependent and the data in Figure IV.3 could not be fit with a single parameter. As further evidence of the success of the layer rigidity model for systems dominated by elastic forces we address the

case of the physisorption of H, and D, into stage-2 KC, to form the ternaries $Va_{2-x'}(R_2)_{x'}KC_{24}$, $0 \le x' \le 2$, R = H, $D.^{74}$ [Here we consider KC24 to be the host material.] Although the structure of the site superlattice for this is not known, 58,74 and there appears to be two sets of guest sites 74,75 it is well established that the physisorption of H_2 or D_2 into KC_{24} does not result in measurable charge backtransfer from the host layers to the intercalate layer. 58,74 Therefore the layer rigidity model should account well for the c-axis expansion in these ternary layered intercalation compounds. That this is indeed the case is evidenced by the normalized basal spacing data shown in Figure IV.6. This data was derived from the work of Doll et al. 74 who fit d(x') with the arbitrarily chosen function $d(x') = 1 - exp(-\gamma x')$. To apply our layer rigidity model to this system we rescaled their data. In layer rigidity model the composition x is the quantity normalized by the saturation value (One may consider x as a probability to fill gallery sites.). Hence x' can be rescaled as x = x'/2 where $0 \le x \le 1$. The basal spacings are normalized as $d_n(x) = [d(x) - d(0)] / [d(1) - d(0)]$. The same functional form used by Doll et al gives a reasonable fit to d (x) (dotted lines in Figure IV.6) after the scaling. However, eq. (III.19) of the layer rigidity model gives an equally good fit for both \mathbf{D}_2 and \mathbf{H}_2 . The reason that the function chosen by Doll et al. works so well is that eq. (III.19) extrapolates to that function at small x and the two functions are very similar but do not extrapolate for $x \rightarrow 1$.

The rigidity parameter obtained from the fits to the data in Figure IV.6 are given in Table IV.1. Since the site superlattice structure is uncertain, 58,74 we cannot calculate the healing lengths. Nevertheless, the measured rigidity parameters are large in the case of D_2 . We suggest that this apparent enhancement of the rigidity parameter results from

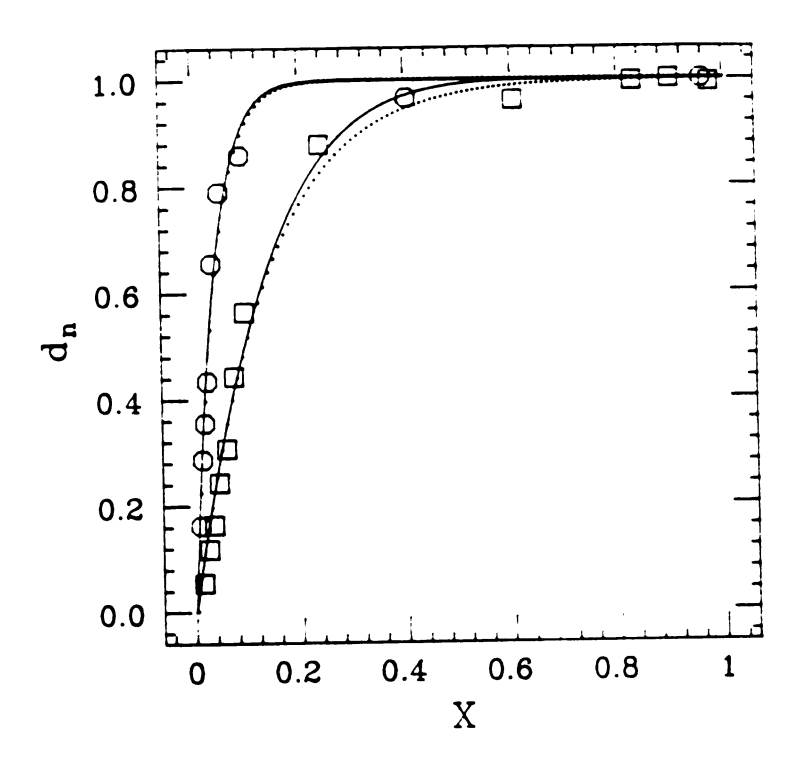


Figure IV.6 The normalized basal spacing vs. composition for $Va_{1-x}(R_2)_xKC_{24}$, 74 R = H (squares), D (circles). The solid lines are fits to the data using eq. (III.19) of the text and yield the measured rigidity parameters given in Table IV.1. The dotted lines are fits using the function $d_n(x) = 1 - \exp(-\gamma x)$ with $\gamma = 7.26$ and 25.2 for H_2 and D_2 , respectively.

the presence of two types of gallery sites, 74,75 of which only one contributes to c-axis expansion. 74 The fraction of expanding sites can be estimated from the minimum value of x at which $d_n(x) = 1$ and is estimated from Figure IV.6 to be $^{\sim}$ 0.2 and 0.7 for D_2 and H_2 , respectively. Thus the actual rigidity parameters which correspond to a rescaling (stretching) of the abscissa in Figure IV.6 are 0.2 x 24.8 = 5.0 and 0.7 x 6.9 = 4.8 (see Table IV.1). The increased rigidity of the stage-2 KC_{24} "host" relative to that of graphite is a consequence of the fact that the host "layers" in the former contain 3 interconnected planes of atoms (2 C layers and 1 K layer) whereas those in the latter are single-atomic sheets

IV.3 Layer Rigidity and Staging

In Safran's model for the staging transition, one of the main results is the existence of $T_{\rm m}$ which is the maximum temperature at which stage 2 is stable. ¹⁹ From the isomorphism of the stage-2 to stage-1 transition to that of a metamagnet in a magnetic field, Safran obtained

$$T_{m} = \frac{1}{4}(U_{0} - V_{a} + V_{b})$$
 (IV.13)

where

$$V_{a} = V_{0} 2^{-\alpha} \xi(\alpha), \qquad (IV.14)$$

$$V_a + V_b = V_0 \xi(\alpha), \qquad (IV.15)$$

and

$$\xi(\alpha) = \sum_{p=1}^{\infty} p^{-\alpha}.$$
 (IV.16)

For T < T_m, there are many single-phase pure-stage states with a restricted stable composition range and two-phase regions, while for T >

 T_m , no staged (n > 1) states are possible for all composition ranges (See Figure IV.1). After rearrangement, we have

$$T_{m} = \frac{1}{4} \left[U_{0} + V_{0} \xi(\alpha) \left\{ 1 - 2^{-(\alpha - 1)} \right\} \right]. \tag{IV.17}$$

Here U_0 , V_0 and $\xi(\alpha)$ are all positive quantities and usually $\alpha > 1$ (e.g. Safran took α = 4). Hence T_m is an increasing function of U_0 and V_0 . We can address qualitatively the relation between layer rigidity and the staging transition in terms of the elastic contributions to \mathbf{U}_0 and \mathbf{V}_0 . The elastic contributions to the attractive intralayer interaction and repulsive interlayer interaction are schematically depicted in Figure IV.7. As has been discussed by Safran, 20 it is favorable for two elastic strain dipoles in the same plane to be adjacent to each other, implying an attractive interaction. The magnitude of this attractive interaction, U_0 , decreases as the healing length λ increases. For example in the case of a perfectly rigid layer with infinite healing length, there is no elastic attractive intraplanar interaction at all. Also there is high interlayer correlation between floppy layers, 34 and dipolar strain fields in the adjacent layers will repel one another, implying a repulsive interaction, Vo. But for rigid layers, the interlayer correlation is also very small (almost zero for Vm which is seven-atomic-planes thick.). Thus there is negligible intercalant-intercalant interlayer interaction implying a very small repulsive interaction. Hence for floppy layers, \mathbf{U}_0 and \mathbf{V}_0 are both large, and for stiff layers both \mathbf{U}_0 and \mathbf{V}_0 are small. In the case of class III Vermiculite, both U and V must be very small and accordingly T_m is so low that Safran's phase boundary 19 lies well below the intercalation temperature. Therefore only the stage-1 state has been observed.

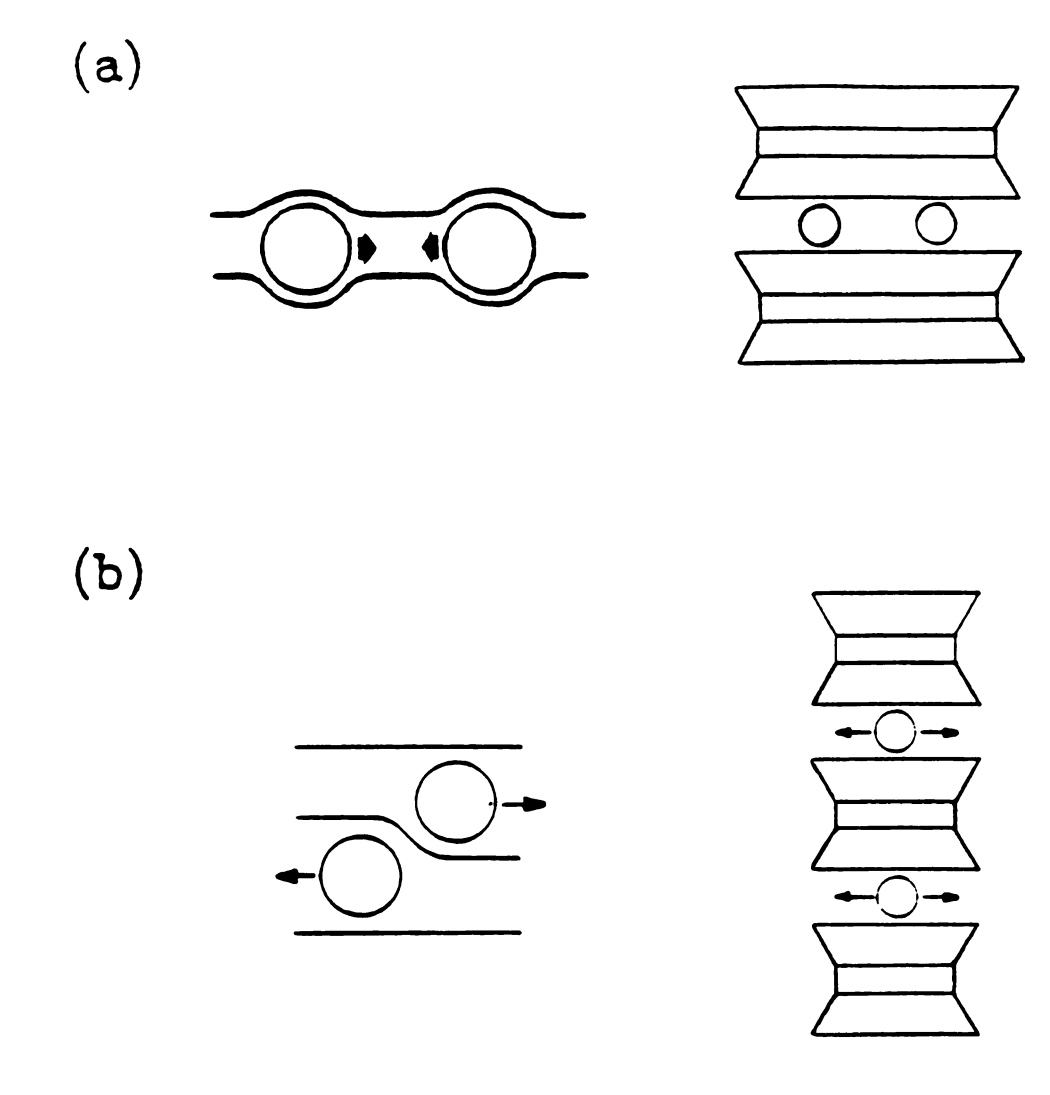


Figure IV.7 A schematic depiction of the attractive intralayer and repulsive interlayer interaction from an elastic origin.

(a) For floppy layer systems two intercalants in the same gallery favor adjacent locations, but for rigid layer systems this attractive interaction is negligible. (b) In floppy layers the high interlayer correlation favors a staggered position, but in rigid layers the interlayer correlation is negligible.

The calculation of the intralayer interaction, \mathbf{U}_0 , which depends upon the layer rigidity is straightforward in the continuum elastic theory. First in the case of a single delta-function-like elastic dipole, the elastic energy (= self energy) $\mathbf{E}_{\mathbf{g}}$ becomes

$$E_{s} = \frac{1}{4} \iint d\vec{s} \left[D(\nabla^{2}W)^{2} + K(\nabla W)^{2} + GW^{2} \right] - \frac{1}{2} \iint d\vec{s} f_{0} \delta(\vec{r}) W(\vec{r}) \quad (IV.18)$$

After integrating by parts, and using eq. (IV.5) and the boundary condition of W = 0 at infinity

$$E_{s} = \frac{1}{4} \iint d\vec{s} \ W(\vec{r}) \ \left[\ DV^{4}W - KV^{2}W + GW - 2f_{0}\delta(\vec{r}) \ \right]$$
$$= -\frac{1}{4} f_{0}W(\vec{r} = 0)$$
 (IV.19)

Now in the case of two dipoles, the elastic energy becomes

$$E = \frac{1}{4} \iint d\vec{s} \left[D\{\nabla^2 w(\vec{r}, \vec{R}_1, \vec{R}_2)\}^2 + K\{\nabla w(\vec{r}, \vec{R}_1, \vec{R}_2)\}^2 + Gw^2(\vec{r}, \vec{R}_1, \vec{R}_2) \right]$$

$$- \left\{ \frac{1}{2} f_0 \delta(\vec{r} - \vec{R}_1) + \frac{1}{2} f_0 \delta(\vec{r} - \vec{R}_2) \right\} W(\vec{r}, \vec{R}_1, \vec{R}_2) \right]$$
(IV.20)

where

$$W(\vec{r}, \vec{R}_1, \vec{R}_2) = W(\vec{r} - \vec{R}_1) + W(\vec{r} - \vec{R}_2)$$
 (IV.21)

from the superposition principle. In eq. (IV.20) the diagonal terms are the self energy for two dipoles (= $2E_s$) and the cross terms are interaction between two intercalants (= $E_{int}(\vec{R_1}, \vec{R_2})$).

Integrating by parts and using eq. (IV.5) and the boundary condition for W, we find

$$\begin{split} E_{\text{int}}(R_1,R_2) &= \iint ds \; \frac{1}{2} \; [\; W(\vec{r} - \vec{R}_1) \; \{\; DV^4 - KV^2 + G\;\} \; W(\vec{r} - \vec{R}_2) \\ &- f_0 \delta(\vec{r} - \vec{R}_1) V(\; \vec{r} - \vec{R}_2) \; - f_0 \delta(\vec{r} - \vec{R}_2) V(\vec{r} - \vec{R}_1)] \end{split}$$

$$= -\frac{1}{2} f_0 W(\vec{R}_1 - \vec{R}_2)$$
 (IV.23)

or

$$E = 2E_s - \frac{1}{2} f_0 W(\vec{R}_1 - \vec{R}_2)$$
 (IV.24)

Using eq. (IV.23), we can write the intralayer interaction part in the Hamiltonian for the intercalants forming a triangular lattice as

$$U(\sigma) = \frac{1}{2N} \sum_{i \neq j} E_{int}(\vec{R}_i, \vec{R}_j) \sigma(\vec{R}_i) \sigma(\vec{R}_j)$$
 (IV.25)

where $\sigma(\vec{R}_i)$ is an Ising-like variable which can have either 0 or 1 and the \vec{R}_i 's are triangular lattice vectors. Following Safran¹⁹ we use the mean-field approximation. After inplane averaging we find

$$U(\sigma) = \frac{1}{2N} \sigma^2 \sum_{i \neq j} E_{int}(\vec{R}_i - \vec{R}_j)$$
 (IV.26)

where σ is the average fractional occupancy of the intercalant sites, which may take continuous values between 0 and 1. From eq.'s (IV.9), (IV.23) and (IV.26) we find

$$U(\sigma) = \frac{1}{2} \sigma^{2}_{i} \Sigma_{0} \left[-\frac{1}{2} f_{0} V(\vec{R}_{i}) \right]$$

$$= \frac{1}{2} \sigma^{2} \left\{ -\frac{f_{0}^{2}}{4\pi\sqrt{DG}} \sum_{i} \Sigma_{0} \left[\int_{0}^{\infty} \frac{qJ_{0}(qR_{i}/\ell)}{q^{4} + 2\zeta q^{2} + 1} dq \right] \right\} \qquad (IV.27)$$

or

$$U(\sigma) = -\frac{1}{2} U_0 \sigma^2$$
 (IV.28)-

where

$$U_0 = \frac{f_0^2}{4\pi\sqrt{DG}} \sum_{i=0}^{\infty} \left[\int_0^{\infty} \frac{qJ_0(qR_i/l)}{q^4 + 2\zeta q^2 + 1} dq \right]$$
 (IV.29)

Because of ℓ the actual contribution of D to U can be evaluated only after the above sum is actually done, but the contribution of G is dominant and U is a decreasing function of G.

Using eq. (IV.29) we can also discuss the effect of the intercalant size difference in the same host. In eq. (IV.29) f_0 can be directly

related to the maximum displacement 72 which is well known to depend on the intercalant size. 2,3 For example the measured basal spacing increases of stage-1 heavy alkali graphite intercalation compounds (relative to the spacing in pristine graphite) are 2.002Å, 2.304Å and 2.590Å for KC_8 , RBC_8 and CsC_8 , respectively. These compounds all have the same (2x2)R0° superlattice structure. If we assume that their rigidity parameters are very similar, then the intralayer interaction energy will be larger for the bigger intercalants and accordingly $\mathbf{T}_{\mathbf{m}}$ will be higher. Unfortunately, experimental data to confirm this prediction is not available yet. Comparison between Li and the heavy alkali intercalants (e.g. Cs) is not straightforward. In LiC6, Li has a $(\sqrt{3}x\sqrt{3})R30^{\circ}$ superlattice structure and is known to sustain a strong corrugation potential which might change the rigidity parameter. Nevertheless if we apply the above argument to the comparison between Li and Cs graphite intercalation compounds, we can expect to see higher stages in Cs compounds at higher temperature. Fisher has reached the same conclusion and reported 76 that the midpoint of a (1 + 2) \rightarrow (1) staging transition in Li_{0.8}C₆ is 440K, while the corresponding transition in Cs_{0.8}C₈ occurs at 600k. Also for TiS₂ intercalation compounds, no staged (n > 1) states are found for Li, while Cs forms staged states at 300K. 18

IV.4 Summary and Concluding Remarks

In this part we have presented the Layer Rigidity Model which fits the c-axis expansion of all three classes of layered solid using only one adjustable parameter p. The rigidity parameter p is related to the healing length λ in both a discrete and continuum version. For the

continuum version we presented a continuum elastic model, which is the first successful and consistent theoretical approach to the problem of gallery expansion in intercalated layered solids. In the continuum elastic model we were able to relate the rigidity parameter p determined from the basal spacing measurements to other independently measured quantities such as the elastic constants and phonon dispersion curves. Also we provided the first successful explanation of the intriguing data for the physisorption of H₂ and D₂ into stage-2 KC₂₄.

Different staging behavior among different classes of layered solids has been discussed using Safran's phase diagram. The dependence of the elastic interlayer and intralayer interaction on layer rigidity has been discussed qualitatively. From the continuum elastic theory the mean-field intralayer interaction, U₀, was calculated to show the actual contribution of each rigidity constant. The resultant intralayer interaction showed a dependence not only on the rigidity parameters but also on the size of the intercalants. Finally we have discussed the staging transition of intercalation compounds with the same host and different intercalants.

V. A Variable-Temperature X-Ray Cryostat With an Externally Adjustable
Internal Goniometer.

V.1 Introduction

Low-temperature X-ray diffraction (LTXRD) is a very useful technique to study many interesting properties of condensed matter. Some of the LTXRD experiments mimic the usual XRD experiments that can be done at room temperature. But by lowering the sample temperature we can reduce the thermal motion of the atoms within the sample, which will improve peak-to-background ratios and also make it possible to obtain more data at high angle (or at high momentum transfer) where Debye-Waller factor effects are more pronounced at room temperature. As a result more accurate crystal-structure analysis on be done and more accurate electron-density maps can be acquired. On the other hand, there are some properties that can be observed only at low temperature. Certain structural phase transitions, thermal contraction, and the crystal structures of gases or liquids telegory to this category.

In most cases the LTXRD apparatus is built as an addition or a modification to the existing XRD system. Thus in designing an LTXRD system it is desirable to optimize the compatibility of the Low-Temperature part with the existing XRD system with minimal modification of both existing XRD system and with minimal modification of the operating procedure. With this "compatibility" in mind one also has to consider several criteria including the temperature range, the control and measurement of sample temperature, the absorption of X-rays, frost prevention, accessibility of the sample, easy and accurate alignment of the sample, and finally maximum scan range.

There is a primary difficulty in orienting a sample located inside of the cryostat. The methods which have be used to orient a sample either involve moving the entire cryostat, 86 using complicated gearing so that the sample inside the cryostat can be rotated about one or more axes 87 or using the Weissenberg geometry (moving detector). 88 Our XRD system has been designed primarily for θ -2 θ scans, so the Weissenberg geometry is not suitable. The method of moving the entire cryostat will result in misalignment between the cryostat axis and the rotation axes of the θ and 2θ circles which can cause sample misalignment. An attempt to solve this problem using either an extra supporting system or with a complicated gearing system is mechanically very demanding, and in many cases supporting bars and gearing units can cause blind regions. Also the scan range tends to be limited by the mechanical construction. In our novel LTXRD system we avoided this problem by putting the externally adjustable small goniometer inside the cryostat.

There are three different types of cooling mechanism to be used with LTXRD: gas-stream cooling, 83 conduction cooling, 84 and immersion cooling. 85 Each cooling method has its own merits and shortcomings. One has to chose the proper cooling method which can satisfy most of the above criteria. We chose to use conduction cooling. The advantages of conduction cooling are: minimal use of cryogen, relatively good thermal equilibrium for a wide range of temperature, and frost free operation. The use of a closed cycle He-cryostat allows us to achieve temperatures well below that of liquid nitrogen with minimum operating cost. Of course there are some disadvantages with the conduction cooling method but most of the disadvantages can easily be taken care of with proper design. For example, blind spots and excessive X-ray absorption are

typical problems with conduction cooling but these problems can be solved by proper window design using thin x-ray transparent materials.

V.2 Apparatus

An overall view of our LTXRD system is given in Figure V.1 and a cut-away view of the home-made interconnection parts (See the following discussion) is shown in Figure V.2. The same parts shown in both figures have common designations.

Our LTXRD system can be divided into three major components. The diffractometer: We use a computer controlled Huber 4-circle diffractometer coupled to Rigaku 12Kw rotating anode MoKa source. The four circles are the Φ -circle (G), Θ -circle (H), 2Θ -circle (I), and χ -circle (J). The cryostat: this consists of a CTI-CRYOGENICS model 22 closed-cycle He-refrigerator (A) with a cold finger (L) which can be cooled down to as low as 9.75K within 50 min in its unmodified configuration (See discussion of modifications below). Finally we employ several home-made interconnection parts (See discussion below) including a multi-purpose vacuum shroud assembly, a sample alignment assembly, a sample holder assembly, and a radiation shield (K). Among these three parts, the home made interconnection parts are the most critical.

The multi-purpose shroud assembly consists of a linear ball bearing (C), vacuum shroud (B), flange (E), and a Kapton window (D). The vacuum shroud which has a cylindrical shape forms the inner moving sleeve of the linear ball bearing. A 260° slot was machined into the the shroud and covered by a Kapton window which was attached with epoxy to form a vacuum tight seal. The flange is connected to the shroud with an

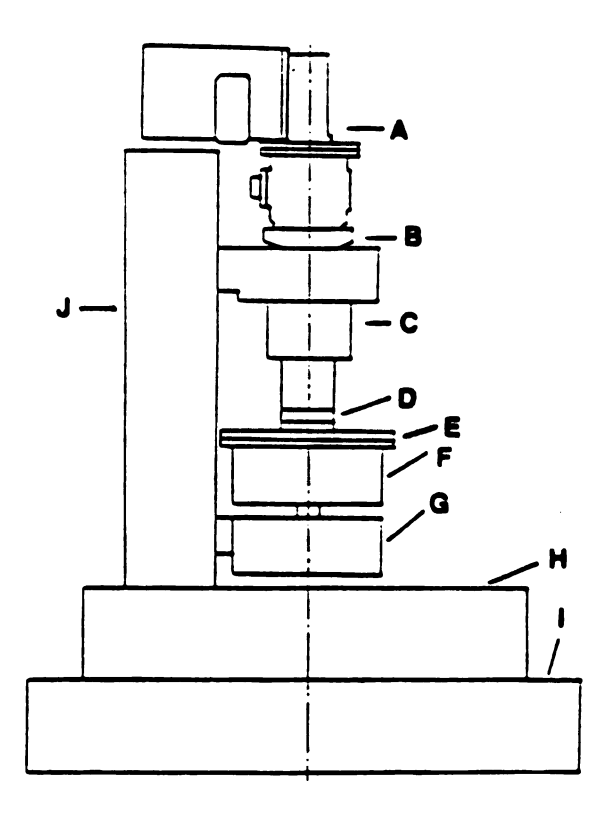


Figure V.1 An overall view of the LTXRD system: A—closed cycle He-cryostat; B—cylindrical vacuum shroud; C—linear ball bearing; D—Kapton window; E—shroud flange; F—sample chamber; G—• circle; H—• circle; I—20 circle; J——X circle

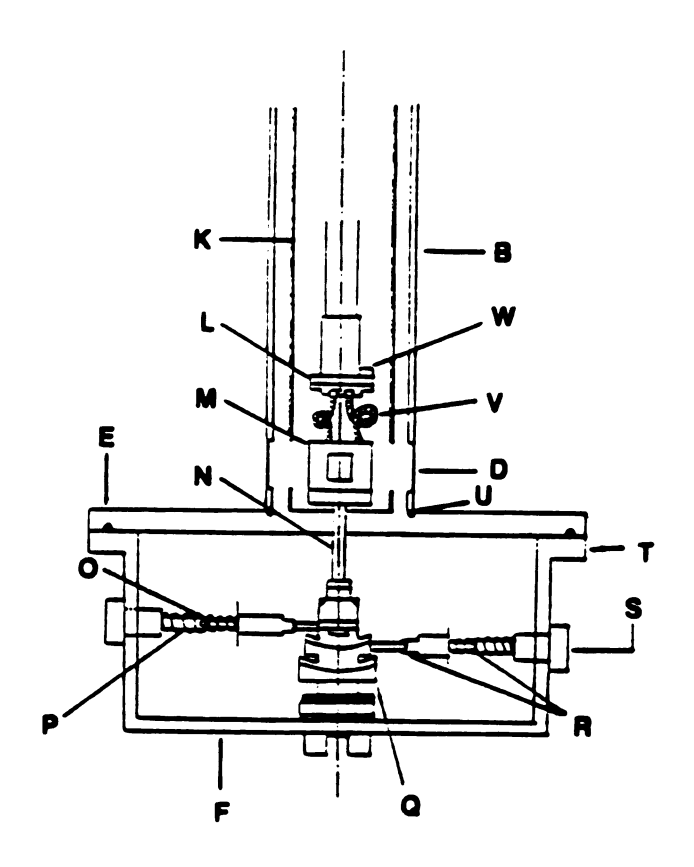


Figure V.2 An cut-away view of the home-made interconnection parts where the same parts shown also in Figure V.1 has same designation: K—raduation shield; L—cold finger; M—sample holder; N—Teflon and Vespel spacers; O—end spring; P—square cross section sliding shaft; Q—small goniometer; R—moni universal joint; S—vacuum feedthrough; T—sample chamber flange; U—O-ring; V—braided Cu wire; W—Si-diode temperature sensor.

O-ring seal (U). To maintain mechanical stability, the vacuum shroud is made of stainless steel.

The sample alignment assembly consists of a sample chamber (F), a small goniometer (Q), vacuum feedthroughs (S), and goniometer key assemblies that include two mini universal joints (R), a square cross-section sliding shaft (P), and an end-spring (O). There are 5 vacuum feedthroughs on the side wall of the vacuum chamber. Four of these are used for the key assemblies to control the small goniometer inside of the vacuum chamber from outside. The remaining one is used for a thermocouple. The sample chamber is connected to the shroud assembly with an O-ring flange (T) and also is supported by the ϕ -circle (G).

The sample holder assembly consists of a copper sample holder (M) which is attached to braided copper wire (V) connected to the cold finger (L). This sample holder can have an arbitrary shape which depends on the sample shape. It is connected to the small goniometer with Teflon and Vespel spacers (N) which are very good thermal insulators.

In our design, the 6-degrees of freedom needed to align the sample are obtained from the combination of the small inside goniometer (Q), flexible braided copper wire (V), the sliding ball bearing (C) with shroud (B) and the Φ -circle (G). The small goniometer with braided copper wire allows 4-degrees of freedom namely the x, y translations and rotations about the x and y axes. The sliding ball bearing with the cylindrical shroud permits both up and down motion (z translation) and rotation about the z axis (Φ angle). Note that the sliding ball bearing retains the cryostat in a position such that the cryostat axis and the rotation axes for the θ and 2θ circles are always coincident.

For easy sample alignment one must be able to control the inside goniometer from outside without breaking the vacuum. This can be done by

using a vacuum feedthrough (S). The major problem of controlling the inside goniometer from outside is not the vacuum seal but rather the fact that turning one goniometer key will cause a change in the position and orientation of all of the other keys thereby altering their alignment with the fixed vacuum feedthroughs. To solve this problem we designed a variable length shaft with mini universal joints. The sliding square cross sectional shaft (P) allows variable length and makes it possible to turn the key. The end spring (O) is used to prevent the turning shaft from slipping out of the goniometer key while the goniometer key is receding. The sliding shaft with mini universal joint (R) is capable of transmitting smooth rotational motions for different relative positions of the goniometer keys and the vacuum feedthroughs.

To reduce X-ray absorption a 5.5μ thick Kapton window (D) was used. The Kapton window can be easily glued to the shroud with epoxy without using a supporting post which is a usual source of a blind spot. There are several advantages of a Kapton window relative to a typical beryllium window. First, Kapton is non-toxic unlike beryllium and is easy to handle. Second, Kapton is transparent in the visible. One can see the sample inside the cryostat through the Kapton window, which makes it very easy to align the sample using a telescope in the usual way

The flange connection (E, T) between the vacuum shroud and the sample chamber allows easy access to the sample. To change the sample one need not remove the cryostat from the XRD system. One can simply expose the sample by pushing up the cryostat and attached shroud through the sliding ball bearing. After the sample change, the cryostat can be lowered again to its original position. Because of the flexible braided

copper wire the sample holder does not change its position and orientation during this cryostat's up and down motion.

For frost free operation a vacuum of 1 torr is sufficient. Also the closed-cycle refrigerator is designed to operate at a vacuum of better than 50 microns. With the 0-ring seal, vacuum feedthroughs and glued Kapton window we achieved a vacuum better than 1 micron using only a rotary pump.

The cold finger temperature was measured and controlled by a Palm Beach Cryophysics model 4075 thermometer and controller with a Si-diode sensor (W) placed on the cold finger. The sample holder which is connected to the cold finger through the braided copper wire usually operates at a slightly higher temperature than the cold finger and its temperature was measured by a copper-constantan thermocouple. The Teflon and Vespel spacer was used to keep the sample holder mechanically connected to the goniometer but thermally insulated. With this arrangement sample temperatures of 40K could be achieved with a cool down time of 60 min.

V.3 Experiment

To test the LTXRD system we studied the (00L) X-ray diffraction patterns of a highly oriented pyrolytic graphite (HOPG) sample at four different temperatures. For low temperature measurement, the temperature controller was set at 200K, 100K, and 10K respectively. The X-ray diffraction pattern was collected up to $q=8.668 \text{\AA}^{-1}$ (where the momentum transfer $q=(4\pi\sin\theta)/\lambda$) without any blind points. The basal spacing d can be calculated from the peak positions of the 00L diffraction peaks. To avoid zero-point calibration errors the slope from the plot of the

peak positions, \mathbf{q}_{00L} , versus peak index, L, was used (Q-plot). The resultant basal spacings are listed with the corresponding temperature in Table V.1.

To date experimental measurements of graphite c-spacing variation with temperature have been mostly carried out at temperatures higher than room temperature 89,90 (up to 2600°C). A comparison between the data reported by various researchers shows the dependence of actual basal spacings on the material and its stacking faults. However the c-axis expansion always exhibits a similar linear behavior with a small quadratic correction. 89,90,91 Baskin and Meyer 81 measured the interlayer spacing of graphite as a function of temperature at low temperature. They also reported the material dependence of the interlayer spacing: they measured c-spacings of 3.3538Å at 297K and 3.3378Å at 78K for single crystal and 3.3600Å at 297K and 3.3392Å at 78K for artificial graphite powder. In addition they reported a noticeable departure of temperature dependence of the basal spacing from linearity at lower temperatures (T < 78K). Steward at $e1^{92}$ attributed this leveling to the limited contraction due to the repulsion between adjacent layers. Thermal expansion of the HOPG has also been studied by Yates et al. 93, Fug et al 94, and Harrison 95. They reported a temperature dependent thermal expansion coefficient α_c which is shown in Figure V.3. For comparison we plotted our data as an average thermal expansion coefficient, α_c^{ave} , versus average temperature, T_{ave} , in Figure V.3. Average thermal expansion coefficient is defined as

$$\alpha_{c}^{\text{ave}} = \frac{d_{2} - d_{1}}{d_{1}(T_{2} - T_{1})}$$
 (V.1)

and $T_{ave} = (T_1 + T_2)/2$. Our data agrees well with reported values in the temperature range of 40K - 200K. But at higher temperature α_C^{ave}

Table V.1. Basal spacing of HOPG as a function of temperature

Temperature (K)		Basal spacing (A)	
Si-sensor	Thermocouple		
295.3	294.8	3.354+.005	
199.7	206.0	3.348+.012	
99.35	112.4	3.341+.006	
11.20	40.8	3.338+.006	

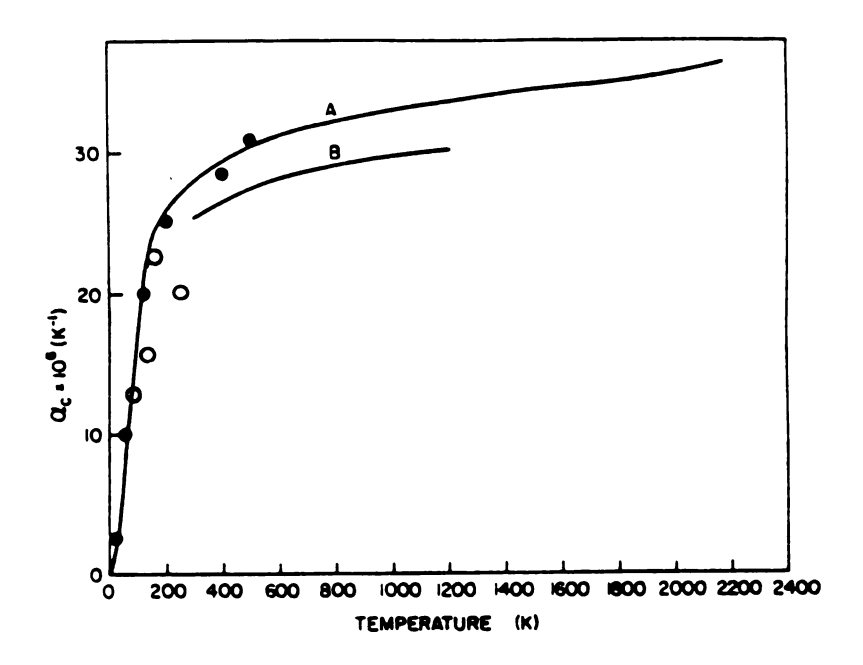


Figure V.3 Temperature expansion of highly oriented pyrolytic graphite (HOPG); from ref. 96. A from refs. 93 and 94, B from ref. 95, and open circles are our data.

shows a noticeable discrepancy. To settle this discrepancy we need to extend our measurements to the higher temperature region.

As shown in the Table V.1, there is a difference between the cold finger temperature measured with the Si-sensor and the sample holder temperature measured with the copper-constantan thermocouple. It is evident that there is a certain temperature gradient in the system and lowest obtainable temperature is raised from the unmodified configuration value. For simple and accurate sample alignment we located the goniometer in the sample chamber and the sample holder is connected to this goniometer with Teflon and Vespel spacers. Even though Teflon and Vespel are good thermal insulators the sample holder is not totally thermally insulated from the outside parts including the sample chamber wall, the shroud and the 4-circle goniometer. Heat leakage through these paths still occurs. This is the price we have to pay for the many other merits and versatility of our new design. We intend to improve the insulation and thus achieve lower temperatures at the sample holder.

Acknowledgment

We wish to thank Dr. J. Doehler for supplying us with Kapton film and Mr. T. Palazzolo for many practical suggestions. Also we appreciate Dr. Arthur Moore for supplying us with HOPG thermal expansion data.

LIST OF REFERENCES

- M. S. Whittingham and A. J. Jacobson, Intercalation Chemistry, (Academic Press, New York, 1982), p. 1.
- 2. S. A. Solin, Adv. Chem. Phys. 49, 455 (1982).
- 3. M. S. Dresselhaus and G. Dresselhaus, Adv. Phys. 30, 139 (1981).
- 4. Z. Cai and S. D. Mahanti, Phys. Rev. B36, 6928 (1987).
- Y. Y. Huang, Y. B. Fan, S. A. Solin, and J. Heremans, Solid St. Comm. <u>61</u>, 469 (1987).
- 6. S. Lee, H. Miyazaki, S. D. Mahanti, and S. A. Solin, submitted to Phys. Rev. Lett..
- 7. K. Watanabe, T. Kondow, M. Soma, T. Onishi, and K. Tamaru, Proc. R. Soc. Lond., A333, 51.
- 8. See for example, Solid State Batteries, C. A. C. Sequeira and A. Hooper ed., (Marinas Nighoff Publishes, Dordrecht, 1985).
- 9. P. B. Weisz, Science, 179, 433 (1973).
- 10. D. Gelbin, AIChE J, 25, 358 (1979).
- 11. T. J. Pinnavaia, Science, 220, 365 (1983).
- 12. See Physics and Chemistry of Materials with Layered Structures, (Reidel, Dordrecht, 1979).
- 13. S. A. Solin, J. Molec. Catalysis, 27, 293 (1984).
- 14. K. Norrish, Trans. Faraday Soc., <u>18</u>, 120 (1954).
- 15. R. E. Grim, Clay Mineralogy, (McGrow-Hill, New York, 1968).
- 16. H. Kim, T. J. Pinnavaia, S. Lee, W. Jin, S. D. Mahanti, and S. A. Solin, to be published.
- 17. G. A. Scholz and R. F. Frindt, Mat. Res. Bull., 15, 1703 (1980).
- J. Rouxel, in Intercalated Layer Material, F. Levy ed., (Reidel, Boston, 1979), p. 201.
- S. A. Safran, Phys. Rev. Lett. 44, 937 (1980).

- 20. S. A. Safran and D. R. Hamann, Phys. Rev. Lett. <u>42</u>, 1410 (1979) also see S. Ohnishi and S. Sugaro, Solid St. Comm. 36, 823 (1980).
- 21. G. W. Brandly and G. Brown ed., Clay Structure of Clay Minerals and Their X-Ray Identification, (Mineralogical Society, London, 1980).
- 22. H. P. Klug and L. E. Alexander, X-Ray Diffraction Procedures for Polycrystalline and Amorphous Materials, (Wiley, New York, 1974), p. 138.
- 23. A. W. Moore in Chemistry and Physics of Carbon, Vol. II, P. L. Walker Jr. and P. A. Thrower ed., (Marcel Dekker, New York, 1973), p. 69.
- 24. W. N. Reynolds, Physical Properties of Graphite, (Elsevier, Amsterdam, 1968).
- 25. S. K. Sinha ed., Ordering in Two Dimensions, (North-Holland, New York, 1980).
- 26. S. Lee, S. A. Solin, W. Jin, and S. D. Mahanti, in Graphite Intercalation Compounds: Science and Applications, M. Endo, M. S. Dresselhaus, and G. Dresselhaus ed., (Materials Research Society, Pittsburgh, 1988).
- 27. H. Kim, W. Jin, S. Lee, T. J. Pinnavaia, S. D. Mahanti, and S. A. Solin, Phys. Rev. Lett. <u>60</u>, 2168 (1988).
- 28. B. R. York and S. A. Solin, Phys. Rev. <u>B31</u>, 8206 (1985).
- 29. J. Ishii, T. Shimanouchi, and M. Nakahira, Inorganica Chimica Acta 1:3, 387 (1967).
- 30. B. R. York, S. A. Solin, N. Wada, R. Raythatha, I. D. Johnson, and T. J. Pinnavaia, Solid St. Comm. <u>54</u>, 475 (1985).
- 31. T. M. Thomas in Intercalation Chemistry, M. S. Whittingham and A. J. Jacobson ed., (Academic Press, New York, 1982).

- 32. R. Zallen, The Physics of Amorphous Solids, (Wiley, New York, 1983), Ch. 4.
- 33. S. A. Solin, P. Chow and H. Zabel, Phys. Rev. Lett, <u>53</u>, 1927 (1984).
- 34. W. JIn and S. D. Mahanti, Phys. Rev. B37, 8647 (1988).
- 35. J. R. Dahn, D. C. Dahn, and R. R. Haering, Solid St. Comm. <u>42</u>, 179 (1982).
- 36. J. E. Fisher and H. J. Kim, Phys. Rev. <u>B35</u>, 3295 (1987).
- 37. D. H. Fink, F. S. Nakayama, and B. L. McNeal, Soil. Sci. Soc. Amer. Proc. 35, 552 (1971).
- 38. M. B. McBride and M. M. Mortland, Clays and clay Minerals 21, 323 (1973).
- 39. D. R. Hines, N. Wada, and M. Suzuki, Bull. Am. Phys. Soc. <u>32</u>, 559 (1987).
- 40. B. E. Warren, X-Ray Diffraction, (Addison-Wesley, Reading MA, 1969).
- 41. H. P. Klug and L. E. Alexander, X-Ray Diffraction Procedure for Polycrystalline and Amorphous Materials, (Wiley, New York 1974), p. 143.
- 42. J. S. Kasper and K. Lonsdale ed., International Tables for X-Ray crystallography, (The Kynoch Press, Birmingham, 1959).
- 43. R. C. Reynolds, Am. Miner. 50, 990, 1965.
- 44. Y. Fan, S. A. Solin, H. Kim, T. J. Pinnavaia and D. A. Neumann, to be published.
- 45. A. Guinier, X-Ray Diffraction (W. H. Freeman, San Francisco 1963).
- 46. S. B. Hendricks and E. Teller, J. Chem. Phys. 10, 147 (1942).
- 47. A. L. Patterson, Phys. Rev. 46, 372 (1934).
- 48. D. M. C. MacEwan, Nature 171, 616 (1953).

- 49. D. M. C. MacEwan, Kolloidzeitschrift 149, 96 (1956).
- 50. H. P. Klug and L. E. Alexander, X-Ray Diffraction Procedure for Polycrystalline and Amorphous Materials, (Wiley, New York, 1974), p. 635.
- 51. W. Xia and M. F. Thorpe, to be published.
- 52. N. W. Ashcroft and N. D. Mermin, Solid State Physics, (Holt, Rinehart and Winston, New York, 1976), p.424.
- 53. J. R. Dahn and W. R. McKinnon, J. Phys. C, 17, 4231 (1984)
- 54. K. K. Bardhan, G. Kirczenow, and J. C. Irwin, J. Phys. C, <u>18</u>, L131 (1985)
- 55. F. S. Galasso, Structure and Properties of Inorganic Solids, (Pergamon, New York, 1970).
- 56. L. Vegard, Z. Phys. 5, 17 (1921).
- 57. J. B. Thomson, in Researches in Geochemistry, Vol. II, P. H. Abelson ed., (Wiley, New York, 1967), p. 340.
- 58. S. A. Solin and H. Zabel, Adv. Phys. 37, 87 (1988).
- 59. S. A. Solin, in Intercalation in Layered Materials, M. S. Dresselhaus ed., (Plenum, New York, 1986), p. 291.
- 60. R. Setton, in Graphite Intercalation Compounds, Vol. I: Structure and Vibrations, H. Zabel and S. A. Solin ed., (Springer, Berlin, 1989), in press.
- 61. S. A. Safran, in Solid St. Phys. Vol 40, H. Ehrenrich and D. Turnbull ed., (Academic Press, New York, 1987), p. 183.
- 62. S. A. Safran and D. R. Hamann, Phys. Rev. B22, 606 (1980).
- 63. S. A. Safran and D. R. Hamann, Phys. Rev. B23, 565 (1981).
- 64. T. Ohno and H. Kamimura, Physica B+C, 117B+C, 611 (1983).
- 65. H. Wagner and H. Horner, Adv. Phys. 23, 587 (1974).
- 66. S. A. Safran and D. R. Hamann, Physica B, 99B, 462 (1980).

- 67. S. E. Millman and G. Kirczenow, Phys. Rev. B26, 2310 (1982).
- 68. S. E. Millman and G. Kirczenow, Phys. Rev. B28, 3482 (1983).
- 69. S. E. Millman and G. Kirczenow, and D. Solenberger, J. Phys. C15, L1269 (1982).
- 70. D. P. Divincenzo and T. C. Koch, Phys. Rev. B30, 7092 (1984).
- 71. K. Komatsu, J. Phys. Soc. Japan, 6, 438 (1951).
- 72. H. Miyazaki, S. Lee, S. D. Mahanti and S. A. Solin, to be published.
- 73. S. C. Moss, R. Reiter, J. L. Robertson, C. Thomson, J. D. Fan and K. Ohshima, Phys. Rev. Lett 57, 3191 (1986).
- 74. G. L. Doll, P. C. Eklund and G. Senatore, in Intercalation in Layered Materials, M. S. Dresselhaus ed., (Plenum, New York, 1986), p. 309; G. L. Doll, Ph. D. Thesis, Univ. of Kentucky, 1987, unpublished.
- 75. J. P. Beaufils, T. Crowley, T. Rayment, R. K. Thomas and J. W. White, Molec. Phys. 44, 1257 (1981).
- 76. R. Clarke, N. Caswell and S. A. Solin, Phys. Rev. Lett. <u>42</u>, 61 (1979).
- 77. R. Nicklow, N. Wakabayashi and H. G. Smith, Phys. Rev. <u>B5</u>, 4951 (1972).
- 78. H. Zabel, A. Magerl and J. J. Rush, Phys. Rev. B27, 3930 (1983).
- 79. F. L. Hirshfeld and G. M. J. Schmidt, Acta Cryst. 9, 233 (1956).
- 80. J. B. Hastings, W. D. Ellenson and J. E. Fisher, Phys. Rev. Lett. 42, 1552 (1979).
- 81. Y. Baskin and L. Meyer, Phys. Rev. 100, 544 (1955).
- 82. L. Silver and R. Rudman, J. Chem. Phys. 57, 210 (1972).
- 83. A. Gieren, W. Hoppe and K. Fleischmann, Angew. Chem. Internat. Ed., 12, 322 (1973).

- 84. O. G. Peterson and R. O. Simmons, Rev. Sci. Instrum. <u>36</u>, 1316 (1965).
- 85. B. Roessler and G. F. Bolling, Rev. Sci. Instrum. 35, 231 (1964).
- 86. P. Coppens, F. K. Ross, R. H. Blessing, W. F. Cooper, F. K. Larsen, J. G. Leipoldt, B. Ress and R. Leonard, J. Appl. Cryst. 7, 315 (1974).
- 87. M. Atoji, Nucl. Instrum. Methods <u>35</u>, 13 (1965).
- 88. H. W. Smith and W. N. Lipscomb, J. Chem. Phys. 43, 1060 (1965).
- 89. J. B. Nelson and D. P. Riley, Proc. Phys. Soc., <u>57</u>, 477 (1945).
- 90. E. Matuyama, Tanso, 7, 12 (1958).
- 91 P. L. Walker, H. A. McKinstry and C. C. Wright, Indust. Eng. Chem. 45, 1711 (1953).
- 92. E. G. Steward and B. P. Cook, Nature 185, 78 (1960).
- 93 B. Yates, O. Pirgon and B. T. Kelly, Fourth International Conference on Carbon and Graphite, (Soc. Chem. Ind., London, 1974) p 606.
- 94. 4. Fug, H. Gasparoux and P. Delhaes, Fourth International Conference on Carbon and Graphite, (Soc. Chem. Ind., London, 1974) p 612.
- 95. J. W. Harrison, High Temperature-High Pressure, 9, 211 (1977)
- 96. A. W. Moore, in Chemistry and Physics of Carbon, vol 17, P. L. Walker, Jr and P. A> Thrower ed., (Marcel Dexxer, New York, 1981) p

APPENDICES

Reprints and preprints of published/accepted papers on this subject.

Physical Review Letters, in press

Composition Driven C-Axis Expansion of Intercalated Layered Solids:

1D non-Vegard's Law Behavior in a 2D Solid Solution

S. Lee, H. Miyazaki[†], S.D. Mahanti and S.A. Solin

Center for Fundamental Materials Research and Department of Physics and Astronomy Michigan State University East Lansing, Michigan 48824-1116

Abstract

We show that a layer rigidity model which includes the effects of elastic deformations of the host layers can account for the composition-dependence of the c-axis lattice expansion of a variety of layered intercalation compounds. Rigidity parameters deduced from this model for each of the three classes of layered solid are reflective of structurally derived rigidity as are the healing lengths computed on the basis of discrete and continuum analyses. The layer rigidity model provides the first quantitative explanation for the 1D non-Vegards law behavior of a 2D solid solution.

PACS numbers: 68.65.+g

† Permanent address: Dept. of Applied Physics, Tohoku Univ. Sendai, Japan

All crystalline solid solutions exhibit a composition-dependent unit cell volume which generally increases with the concentration of the largest constituent. When this variation is linear the system is said to obey Vegard's law . 2 Most solid solutions exhibit a more complex nonlinear behavior which has been accounted for empirically by augmenting Vegard's law with a polynomial that represents a composition-dependent mixing volume. 3 In order to gain a more fundamental understanding of the origin of non-Vegard's law behavior several authors 4-6 have found it advantageous to address systems which contain crystalline solid solutions of reduced dimensionality. For instance, there are a variety of ternary layered intercalation compounds (hereinafter called ternaries) of the form $A_{1-x_{\sigma}}B_{x_{\sigma}}L$, $0 \le x_{g} \le 1$, where B is the larger ion and x_{g} defines the composition of the ions which actually reside in the gallery and contribute to c-axis expansion. The guest species, A and B form a 2D commensurate but compositionally disordered solid solution between the host layers, L. 7-9 [Note that A can represent a vacancy (i.e., A = Va).] Because of the highly anisotropic structural and physical properties of ternaries, 7-9 the dominant change in their cell volume with intercalate composition results from c-axis expansion. The one dimensional (1D) form of Vegard's law is then

$$c(x_g) = (1 - x_g)c_A + x_gc_B$$
 (1)

where c, c_A and c_B are the c-axis repeat distances of the mixed and endmember compounds. But most ternaries exhibit a superlinear (concave downward) $c(x_g)$. Even though ternaries represent the most basic and simplified (eg. 1D) systems for studying composition-driven lattice expansion, attempts to account for their nonlinear response have to date been markedly unsuccessful. In this letter we rectify this deficiency and

present a one-parameter model which accounts for the c-axis expansion of a broad range of ternaries.

Layered solids have been classified into three subgroups on the basis of their rigidity with respect to out-of plane distortions. 10 Thus graphite is the prototypical class I layered solid whose monatomically thin layers 11 are "floppy". The three-atom-thick layers of the dichalcogenides 12 such as TiS2 are more "rigid" and render them class II status. 10 Finally, the 2:1 layered-silicate clays such as vermiculite (Vm) whose host layers are constructed from seven interconnected planes of atoms 13 are extremely "rigid" and belong in the class III grouping. 10 All of the above mentioned host systems can be intercalated to form solid solution ternaries. Although the three resultant classes of ternaries exhibit a broad range of physical properties, the graphite, TiS2 and Vm hosts possess a common structural feature: their guest sites can form a 2D triangular lattice. We will show that the c-axis lattice expansions of these "triangular" ternaries are amenable to an analysis which spans their physical diversity.

In Fig.1. we show the measured composition dependence of the normalized basal spacing, $d_n(x_g)$, for $Va_{1-x_g}Li_{x_g}^{C_6}$, $Va_{1-x_g}Li_{x_g}^{TiS_2}$, and $Rb_{1-x_g}^{Cs}x_g^{Vm^{14}}$ which represent, respectively, the class I, II and III "triangular" host systems. Here $d_n(x_g) = [c(x_g) - c(0)]/[c(1) - c(0)]$. All three ternaries exhibit a superlinear non-Vegard's law behavior.

In an attempt to explain the c-axis expansion of $Va_{1-x_g}^{Li} x_g^{TiS}_2$ Dahn et al. 4 employed a rigid layer model in which the undeformable layers are coupled by springs of spring constant k and K representing, respectively, the guest-host interaction and the vacancy or host-host interaction. Safran modified the original rigid layer model to account for anharmonic softening

of the vacancy springs in the presence of the guest springs. Then the rigid layer model yields $d_n(x_g) = x_g/[(1-x_g)\alpha + x_g]$ which satisfies the boundary conditions $d_n(0) = 0$, $d_n(1) = 1$ and gives Vegard's law behavior when $\alpha = 1$. Plots of the modified rigid layer model for several values of α are shown in Fig. 1. It is evident from these plots that the rigid layer model fails to fit the measured $d_n(x_g)$ for any of the ternaries. This is not surprising for graphite or even for TiS_2 since their host layers are far from rigid. But the model also fails for the $\operatorname{Rb}_{1-x_g} \operatorname{Cs}_x \operatorname{Vm}$ system to which it should be most applicable given its high host layer rigidity. 10

In an effort to improve upon the rigid layer model Jin and Mahanti¹⁵ (JM) introduced a model with nondeformable layers but with "additional" springs which represented the finite compressibility of the guest species. Their model also addressed interlayer correlations. Nevertheless, even though this model employed several parameters, its success was marginal when it was applied to the dual alkali graphite intercalation compounds (GICs) of the type $M_{1-x}M'_xC_8$ for which interlayer correlations should be most pronounced in $d_n(x)$. [We do not address the dual-alkali GICs because the gallery composition of these materials has not yet been established and the actual form of $d_n(x_g)$ is therefore unknown.] Moreover, the multiparameter JM model does not provide an acceptable fit to the data of Fig. 1.

We now describe our layer rigidity model which unlike all previous models accounts for the data of Fig. 1 and does so with the introduction of only one parameter. The essential feature of the layer rigidity model is the deformability of the host layers which in its discrete version is characterized by a rigidity parameter, P. Here we also introduce a continuum version which is characterized by a healing length, λ and we

derive a relation between P and λ which provides an independent test of the model when the host elastic constants or phonon dispersions are known.

In the discrete embodiment of the model which we introduced 14 to explain the sigmoidal form of $d_n(x)$ for Vm ternaries, one envisions a single gallery bounded by a pair of host layers. Incompressible guest ions whose relative proportions depend on x_g randomly decorate the sites of a 2D triangular lattice. The layers experience a pillbox-like discrete puckering over the larger B ion. The lateral extent of this puckering is specified by P which is equal to the total number of puckered lattice sites for a single B ion. Computer simulations 15 of the average gallery height, $d(x_g)$, yield a normalized basal spacing which obeys Vegard's law for P = 1 and exhibits superlinear behavior for larger values of P. These simulation results are in excellent agreement with an analytical solution of the form 14,16

$$d_n(x_g) = 1 - (1 - x_g)^p, 0 \le x_g \le 1.$$
 (2)

In Fig. 1 the solid lines represent fits to the data using Eq. (2). With the exception of the Va_{1-x} Li $_{g}$ TiS $_{2}$ system the fits are excellent and far superior to those obtained using the rigid layer model. The rigidity parameters deduced from the fits to the data in Fig. 1 are given in Table I and as expected increase from class I to class III ternaries.

It is desirable to relate P to a healing length which is a measure of the lateral range over which a puckered layer returns to its undistorted form. The healing length, $\lambda_{\rm d}$, for the discrete layer rigidity model can be simply estimated from the relation P = $(\pi\lambda_{\rm d}^2)/\alpha A_0$ where the numerator is the area of the puckered region, α is the ratio of the area per site of the saturated $(x_{\rm g}=1)$ superlattice to the area per host site [for Li $_{\rm g}$ C $_{\rm f}$ 6 the superlattice is $(\sqrt{3}x\sqrt{3})R30^0$ so $\alpha=3$]. If a_0 is the host lattice intersite distance then $\lambda_{\rm d}=[1/(3.63)^{1/2}](\alpha P)^{1/2}a_0$ (see Table I).

To more precisely quantify the influence of layer deformations on c-axis expansion we treat the host layers as a stacked set of elastic continuum in the form of the deformable plates of finite thickness. For galleries which each contain single point-like B ions at \vec{r}_0 in a sea of vacancies or A ions, the gallery height, $V(\vec{r} - \vec{r}_0)$, is obtained from 17,18

$$\{D\nabla^4 - K\nabla^2 + G\}V(\vec{r} - \vec{r}_0) = f_0\delta(\vec{r} - \vec{r}_0)$$
 (3)

where D and K are respectively the flexural rigidity and the transverse rigidity of the individual plates, and G is the c-axis compressibility of the stack while f_0 represents the δ -function like force from the B ion. Each of the coefficients in the brackets in Eq. (3) can be expressed in terms of the effective layer thickness, 2H, the basal spacing, d, and the host elastic constants, C_{ij} . Thus $D = 2[(C_{11}^2 - C_{12}^2)H^3]/3C_{11}$, $K = dC_{44}$, and $G = 2C_{33}/d$. Equation (3) can be solved to give

$$W(\rho) = \frac{f_0}{2\pi\sqrt{DG}} \int_0^{\infty} \frac{qJ_0(q\rho/l_0)}{q^4 + 2\delta q^2 + 1} dq$$
 (4)

where $\rho = |\vec{r} - \vec{r}_0|$, $\ell_0 = (D/G)^{1/4}$ gives the length scale and $\delta = K/[2(GD)^{1/2}] \le 1$ gives the relative strength of the transverse rigidity.

For a single defect, we can define the healing length $\lambda_{\rm C}$ as the distance at which the gallery height relaxes to half its maximum value i.e. $W(\lambda_{\rm C})=1/2[W(0)]$. From Eq. (4) we obtain $\lambda_{\rm C}(\delta)=Z(\delta)l_0$ where $Z(\delta)$ is a slowly decreasing function of δ with Z(0)=1.302, Z(0.5)=1.276. One can obtain $\lambda_{\rm C}$ from δ and l_0 . These are functions, respectively of D, K, and G the first two of which can be determined from the in-plane TA dispersion of layered solids given by $\omega^2(q) \propto Dq^4 + Kq^2$. Alternatively, K and G can be obtained from the stiffness constants as can D if H is known. For graphite K = 0 so the TA dispersion yields D directly and K and G are found from the known basal spacing and reported C_{ij} 's. Using this approach we find $\lambda_{\rm C}$ =

1.88 Å in reasonable agreement with the value 2.45Å obtained from the experimental value of P (see Table I and the following discussion).

For most layered materials, neither the elastic constants nor the phonon dispersions are available. Therefore, it is useful to derive a relationship between $\lambda_{_{\rm C}}$ and P by extending the continuum theory to the case of a dilute distribution of B ions. Using the superposition principle, we can obtain the average gallery height, <W>, as a function of the concentration of $x_{_{\rm C}}$. In the limit $x_{_{\rm C}}$ <1 the result for <W> normalized by the maximum gallery height, $x_{_{\rm C}}$ due to a single B ion yields

$$d_{n}(x_{g}) = \alpha g(\delta) \left[\lambda_{c}(\delta)/a_{0}\right]^{2} x_{g}$$
 (5)

where $g(\delta)$ is given by

$$g(\delta) = \frac{16}{\sqrt{13}} \frac{(1 - \delta^2)^{1/2}}{1 - (2/\pi) \tan^{-1}[\delta/(1 - \delta^2)^{1/2}]}.$$
 (6)

By comparing eq. (5) with eq. (2), we have

$$\lambda_{c}(\delta) = a_{0} \left[\alpha P/g(\delta)\right]^{1/2}. \tag{7}$$

The values of $\lambda_{\rm C}(\delta)$ thus evaluated for stage -1 ternaries compare reasonably well with those of $\lambda_{\rm d}$ (see Table I). Note that $\lambda_{\rm C}$ for a defect of finite size should be somewhat larger than that of a point object. Here the value of δ is assumed to be the same as for graphite (0.14) in the cases of TiS₂ and Vm. The short healing length found for graphite is consistent with the results of X-ray studies of disordered alkali graphite intercalation compounds ¹⁹ which indicate that the host potential is strongly modulated in the vicinity of a guest ion.

Since the charge on the host layers in class III ternaries is fixed their c-axis expansion is purely elastic. However, the success of the layer rigidity model for the class I and II ternaries is an indication that charge exchange has a small effect on host layer stiffness. If this were not so, P would be composition-dependent and the data in Fig. 1 could not be fit with

a single parameter. As further evidence of the success of the layer rigidity model for systems dominated by elastic forces we address the case of the physisorbtion of H₂ and D₂ into stage-2 KC₂₄ to form the ternaries $Va_{2-x'}(R_2)_x, KC_{24}, 0 \le x' \le 2, R = H, D.^{20}$ [Here we consider KC_{24} to be the host material.] Although the structure of the site superlattice for this has not been definitively clarified, 7,20 and there appears to be two sets of guest sites 20,21 it is well established that the physisorbtion of H_2 or D_2 into KC_{24} does not result in measurable charge backtransfer from the host layers to the intercalate layer. 7,20 Therefore the layer rigidity model should account well for the c-axis expansion in these ternaries. That this is indeed the case is evidenced by the data shown in Fig. 2. This data was derived from the work of Doll et al. 20 who fit d(x') with the arbitrary function $d(x') = 1 - exp(-\gamma x')$. The same function when normalized and rescaled from x'to x with $0 \le x \le 1$ gives a reasonable fit to $d_n(x)$ (dotted lines in Fig. 2) However, Eq. (2) of the layer rigidity model gives an equally good fit for both D, and H,. The reason that the function chosen by Doll et al. works so well is that Eq. (2) extrapolates to that function at small x and the two functions are very similar but do not extrapolate for x **→ 1.**

The rigidity parameters obtained from the fits to the data in Fig. 2 are given in Table I. Since the site superlattice structure is uncertain 7,20 we cannot calculate the healing lengths. Nevertheless, the measured rigidity parameters are large especially in the case of D_2 . We suggest that this apparent enhancement of the rigidity parameter results from the presence of two types of gallery sites 20,21 of which only one contributes to c-axis expansion. The fraction of expanding sites can be estimated from the minimum value of x at which $d_n(x) = 1$ and is estimated

from Fig. 2 to be $^-$ 0.2 and 0.7 for D₂ and H₂, respectively. Thus the actual rigidity parameters which correspond to a rescaling (stretching) of the abcissa in Fig. 2 are 0.2x24.8 = 5.0 and 0.7x6.9 = 4.8 (see Table I). The increased rigidity of the stage-2 KC₂₄ "host" relative to that of graphite is a consequence of the fact that the host "layers" in the former contain 3 interconnected planes of atoms (2 C layers and 1 K layer) whereas those in the latter are single atomic sheets.

We gratefully acknowledge useful discussions with M.F. Thorpe and T.J. Pinnavaia. This work was supported by the NSF and in part by the MSU CFMR.

References

- 1. F.S. Galasso, "Structure and Properties of Inorganic Solids", (Pergamon, New York, 1970).
- 2. L. Vegard, Z. Phys. 5, 17 (1921).
- 3. J.B. Thompson, in "Researches in Geochemistry, Vol II" ed. by P.H. Abelson, (Wiley, New York, 1967), p.340.
- 4. J.R. Dahn, D.C. Dahn and R.R. Haering, Solid St. Comm. <u>42</u>, 179 (1982).
- 5. S.A. Safran, in "Solid State Physics", ed. by D. Turnbull and H. Ehrenreich, (Academic Press, New York, 1987).
- 6. J.E. Fischer and H.J. Kim, Phys. Rev. B35, 3295 (1987).
- 7. S.A. Solin and H. Zabel, Adv. Phys 37, 87 (1988).
- 8. S.A. Solin, in Intercalation in Layered Materials", ed. by M.S. Dresselhaus, (Plenum, New York, 1986) p. 291.
- 9. R. Setton, in "Graphite Intercalation Compounds, Vol. I.: Structure and Vibrations" ed by H. Zabel and S.A. Solin, (Springer, Berlin, 1989), in press.
- 10. S.A. Solin, J. Molec. Catalysis 27, 293 (1984).
- 11. S.A. Solin, Adv. Chem. Phys. 49, 455 (1982).
- 12. E.A. Marseglia, Int. Rev. Phys. Chem. <u>3</u>, 177 (1983).
- 13. R.E. Grim, "Clay Mineralogy", 2nd Ed., (McGraw Hill, New York, 1968).
- 14. H. Kim, W. Jin, S. Lee, P. Zhou, T.J. Pinnavaia, S.D. Mahanti, and S.A. Solin, Phys. Rev. Lett. <u>60</u>, 2168 (1988).
- 15. W. Jin and S.D. Mahanti, Phys Rev. B37, 8647 (1988).
- 16. M.F. Thorpe, Phys. Rev., in press.
- 17. K. Komatsu, J. Phys. Soc. Japan 6, 438 (1951).
- 18. H. Miyazaki, S. Lee, S.D. Mahanti and S.A. Solin, to be published.
- 19. S.C. Moss, G. Reiter, J.L. Robertson, C. Thompson, J.D. Fan, and K. Ohshima, Phys. Rev. Lett. <u>57</u>, 3191 (1986).
- 20. G.L. Doll, P.C. Eklund and G. Senatore, in "Intercalation in Layered Materials", ed. by M.S. Dresselhaus, (Plenum, New York, 1986), p.309; G.L. Doll, Ph.D. Thesis, Univ. of Kentucky, 1987, unpublished.
- 21. J.P. Beaufils, T. Crowley, T. Rayment, R.K. Thomas and J.W. White, Molec. Phys. 44, 1257 (1981).

TABLE I. Important Parameters for Several Ternary Layered Intercalation Compounds.

Stage and Structure				Site Ratio	Intersite Distance	Healing Lengths	
	Class	Sample	P	α	a ₃ (A)	$\lambda_{d}(A)$	$\lambda_{c}^{(A)}$
Stage-l Triangular	I	Val-xLixC6	2	3	2.46	3.16	2.45
	II	Val-xLixTiS2	3.5	1	3.41	3.35	2.60
	III	$Rb_{1-x}Cs_xVm$	7	1	5.34	7.42	5.77
Stage-2 Unknown	II 1	Va _{2-x} (H ₂) _x KC ₂₄	4.8 (6.9)	-	√ĪĪ(2.46)³	-	-
	II.	Va _{2-x} (D ₂) _x RC ₂₄	5.0 (24.8)	-	√12(2.46)³	-	•

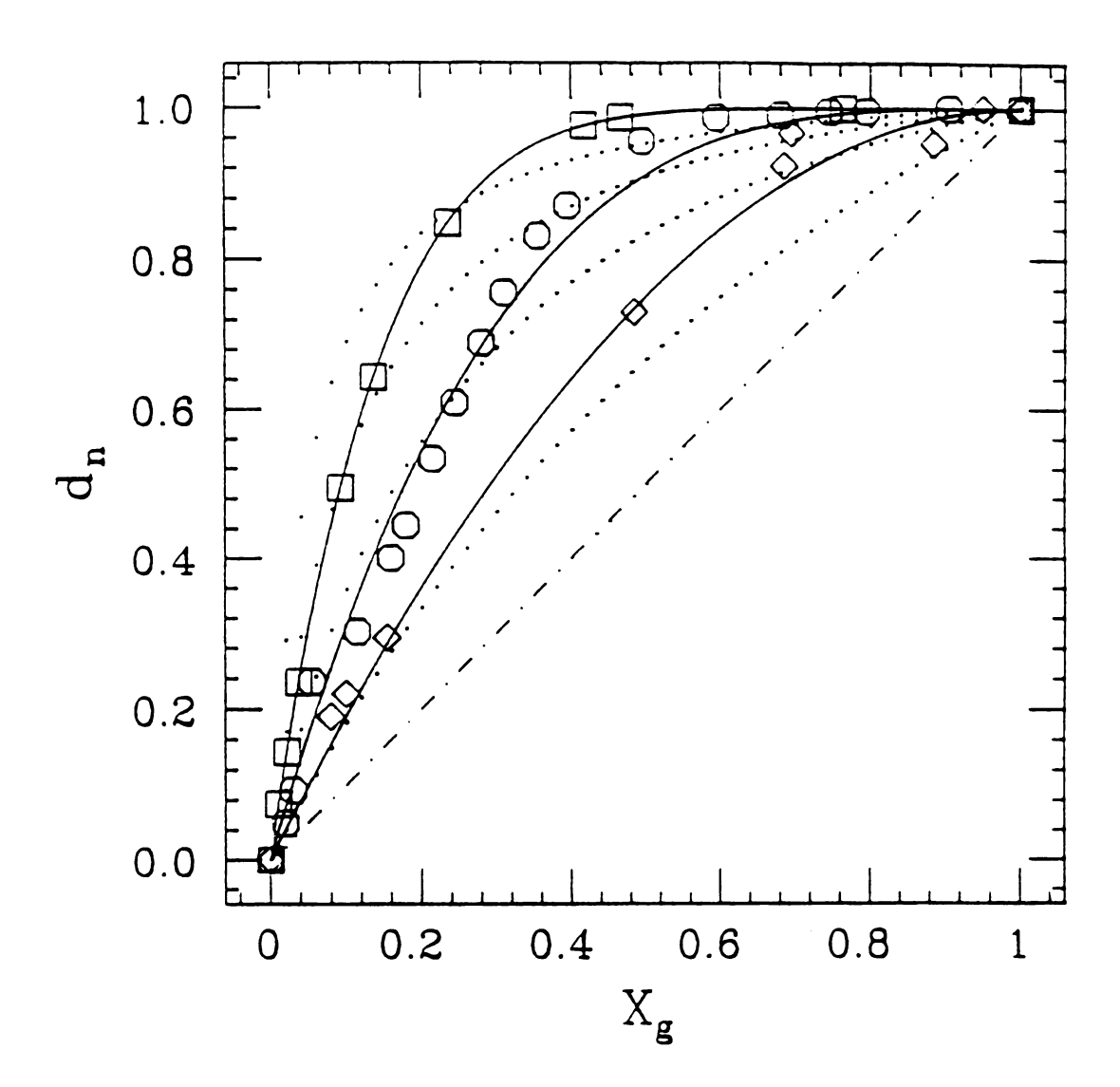
 $^{^1}$ The class designation of this compound is based on the fact that the KC $_{24}$ *host layers* consist of 3 atomic planes (see text).

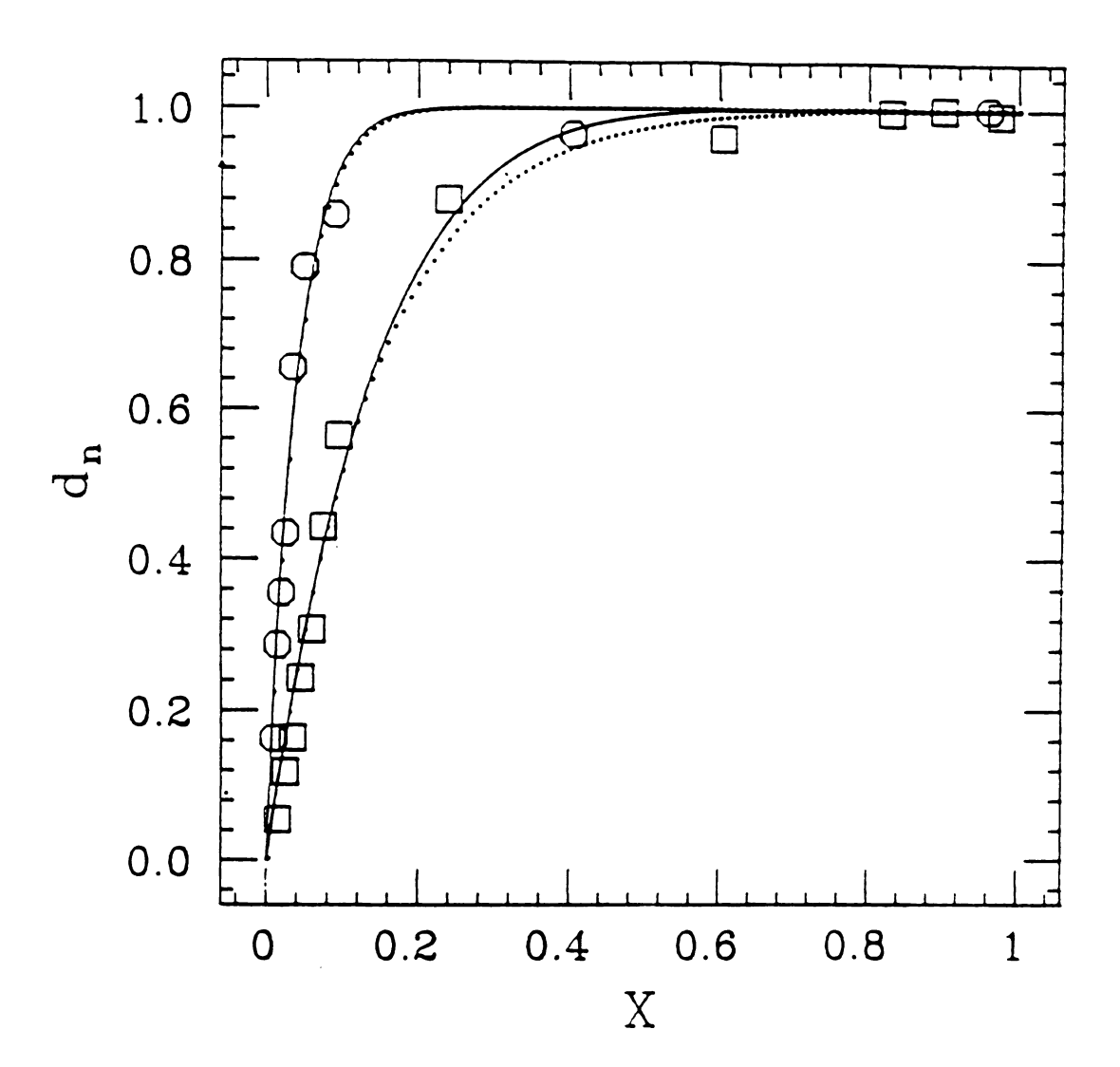
The bracketed number is the measured value and the unbracketed number is the actual (corrected) value (see text).

This value is based on a stoichiometric K/C ratio of exactly 1/24.

Figure Captions

- Fig. 2. The normalized basal spacing vs. gross composition for $Va_{1-x}(R_2)_xKC_{24}$, 20 R = H (squares), D (circles). The solid lines are fits to the data using Eq. (2) of the text and yield the measured rigidity parameters given in Table I. The dotted lines are fits using the function $d_n(x) = 1 \exp(-\gamma x)$ with $\gamma = 7.26$ and 25.2 for H_2 and D_2 , respectively.





From: Graphite intercalation
Compounds:
Science and Applications

reside and opposite

Edited by:

M. Ende, Slatestu Universey

M.S. Dressettinus, Messettinsets institute of Technology

G. Dressettinus, Messettinsets bistitute of Technology

LAYER RIGIDITY IN INTERCALATED LAYER SOLIDS

S. LEE, S.A. SOLIN, W. JIN AND S.D. HAHANTI Center for Fundermantal Materials Research and Department of Physics and Astronomy, Michigan State University, East Lansing, MI 48824-1116

INTRODUCTION

Graphite, layer dichalcogenides, and vermiculite (Vm) are prototypes of three different groups of layered solids [1]. Graphite is composed of atomically thin sheets of atoms, layer dichalcogenide compounds are often composed of three distinctive planes of strongly bonded atoms, and vermiculite layers are thick assemblies of seven planes of strongly bonded atoms. These are all considered layered compounds because the intralayer forces binding the atoms together are much stronger than the interlayer forces. As a result, foreign species can be readily intercalated into the galleries between the host layers.

One of the most interesting phenomena observed in intercalation compounds is the existence of a long-period one dimensional modulated structure along the c-exis, namely staging. The staging phenomena is characterized by stage number n which refers to the number of host layers separating two adjacent intercalant layers. In graphice intercalation compounds, high stages have been prepared, and certain intercalation compounds of transition metal dichalcogenides have been shown to form low stages; but vermiculite has been found only in a stage-1 state. In Safran's model of staging [2]; competition between repulsive interplanar interactions and attractive intraplanar interactions is responsible for staging. Because elastic interactions contribute to the interatomic forces [2,3], one can expect quite distinctive staging behavior among these layers solids with different layer rigidity with respect to transverse distortions.

layer rigidity with respect to transverse distortions.

In the first part of this paper we introduce a rigidity parameter P and a healing length A to quantify and parameterize layer rigidity. In the second part we discuss briefly why only the stage-1 state is observed in the vermiculite system.

LAYER RIGIDITY

Many studies of the staging mechanism have shown that intercalant-intercalant interactions can be mediated by the elastic strain field present in the host [3]. The first attempt to include the elastic energy in lattice gas models of intercalation systems was made by Dahn et al. [4]. In their model, they treated host layers as infinitely rigid planes held together by harmonic springs. Even though they were able to construct a reasonable phase diagram in T-x plane (where x is the intercalant concentration) and were able to recover the V(x) and -6x/6V behavior of Li/LiTiS, electrochemical cells, their model could not quantitatively account for the full x-dependence of the c-axis repeat distance of any intercalated layered solid [4,5]. It is not surprising that the perfectly rigid-layer versions of elastic models fail when applied to fluppy or moderately rigid hosts such as graphite and layer dichalcogenides [5]. But they are also qualitatively inconsistent with data derived from vermiculite hosts to which rigid-layer models should be more applicable [6,9]. Another way to model the elastic interaction is by local deformation of the host layers. Vith finite layer rigidity, one can imagine that when intercalants are introduced the gallery height between two layers will be different from the pristine host material because the host layers are locally deformed at an occupied site. The actual composition dependence of the c-axis repeat distance will be governed by the way these distortions are relaxed away from the locally expanded sites [5,9].

To understand the observed basal spacing variations a model monolayer system with finite layer rigidity has been studied by computer simulation [9]. For simplicity we assume that the intercalant ions are hard-spheres. Starting from a 2-dimensional lattice (lattice constant \mathbf{a}_0) representing a single gallery with each lattice site occupied by a small intercalant of height $\mathbf{d}(0)$, we randomly replace the small intercalants with large intercalants with height $\mathbf{d}(1) > \mathbf{d}(0)$. (In binary systems, small intercalant means an unoccupied site and $\mathbf{d}(0)$ is the pristine host repeat distance.) The

height of a cell within a healing length A from the large intercalant is also increased to d(1). A second large ion in this region does not affect already expanded cells but expands unexpanded cells within λ of its lucation. Replacement of the small intercalants continues to saturation. If we define f(x) as the fraction of cells with height d(1), then the normalized interlayer spacing $d_1(x)=f(x)$; where $d_2(x)=f(x)=f(x)$ and f(x)=f(x)=f(x) are shown in Fig. 1 for several different healing lengths λ . Using effective medium arguments [8], we can describe the normalized spacing $d_n(x)$ for a monolayer by the equation

$$d_{n}(x) = \{1 - (1-x)^{p}\}, \tag{1}$$

where P is a layer rigidity parameter given by P = 2+1 for our model; 2 is the number of neighboring sites that are puckered by the insertion of an isolated large intercalant (2-7 for a triangular lattice and 3 for a honeycomb lattice with healing length $\lambda = a_0$).

Our rigidity model can account for the four functional forms of d(x) namely linear (Vegard's law), super and sublinear and sigmoidal. Linear and superlinear forms are shown in Fig. 1, but the sublinear and algoridal forms

superlinear forms are shown in Fig.1, but the sublinear and sigmoidal forms are outside the monolayer model [9]. Several mechanisms including the relative magnitudes of host-guest and host-host interactions, interlayer correlations, and the presence of defect sites can produce sublinear behavior in d (x) but only the latter two can generate threshold effects seen in a signoidal form. The interlayer correlation mechanism is one in which large guest ions locally pucker the bounding layers so that at low x they adopt staggered lateral positions. This mechanism is relevant to host materials with low transverse layer rigidity such as graphite while a defect (non-gallery-expanding) sites mechanism is more appropriate to the more rigid layers such as vermiculite. Examples for each functional form of $\mathbf{d}_{\mathbf{n}}(\mathbf{x})$ and the models applied to fit these forms are given in table 1.

LAYER RIGIDITY AND STAGING

We have used Eq.(1) to obtain a fit to the data of Fig.2. The layer We have used Eq.(1) to obtain a fit to the data of Fig.2. The layer rigidity parameters P which give very good fits (solid lines in Fig.2) are P = 2 and P = 3.5 respectively for the super linear forms of Li C, and Li TiS, and P = 7 for the signoidal form of Cs Rb, -vm. From the definition of the layer rigidity parameter, P = Z + 1, we can determine that $\lambda(\text{graphite}) < a, (\text{graphite}) = 2.46 Å, <math>\lambda(\text{TiS}_2) = a, (\text{TiS}_2) = 3.41 Å$ and $\lambda(\text{vm}) = a, (\text{Vm}) = 5.34 Å$. The fact that host layer distortion falls off slowly in the order of graphite, TiS, and Vermiculite is consistent with the intuitive picture of layer stiffness based on atomic arrangement. As has been discussed by Safran [2,3], it is favorable for two elastic strain dipoles in the same plane to be adjacent to each other. implying an attractive interaction. The plane to be adjacent to each other, implying an attractive interaction. The magnitude of this attractive interaction, U_0 , increases as the healing length λ decreases. (For a perfectly rigid layer with infinite healing length, there is no elastic intraplanar interaction.) Also there is high interlayer correlation in the floppy layers, and dipolar strain fields in the adjacent layers will repel one another, implying a repulsive interaction. V. But for the rigid layers, the interlayer correlation is also very small (almost zero for Va which is seven atomic planes thick). Thus there is negligible intercalant-intercalant interlayer interaction implying a very small repulsive interaction (Fig. 3). Hence for the floppy layers, U and V are both large, and for stiff layers both U and V are

In Safran's model for the staging transition, the interlayer attractive interaction -U (U > 0) and interlayer repulsive interaction V contribute to the T (the maximum temperature at which stage two is stable) in the same mannel [2]; in other words T is reduced as U and V become smaller. Hence for the stiff Vermiculite layer, both U and V are small and accordingly T is low. Safran's phase boundry lies well below the intercalation temperature and, therefore, only the stage-1 state has been observed [6,9].

Our future goal is to find the relationship between the healing length A and elastic constants C, of the host material, and express U and V as functions of the healing length A.

Table I. Four types of basal spacing variation of layered solids.

Behavior	System	Hodel	Comments
Superlinear	Li C and LixTis2	RL LR	Poor fit Good fit
	K(NH ₃) _x C ₂₄	RL RL+Electr. Effect LR	Poor fit Excellent fit Excellent fit
	K(H2,D2)xC24	Faperical(1-e-ax)	Very poor fit Excellent fit Excellent fit
Sigmoidal	H _{1-x} H _x C ₈	LR + Interlayer corr.	Good fit
	A _{1-x} B _X -Vm	LR + Defect Sites	Excellent fit
Sublinear	Not been observed	RL LR	Both could yield shape
Linear	H _{1-x} H _x C ₈	Any model	Excellent fit

RL and LR represent Dahn's rigid-layer model and our layer rigidity model, respectively. See Ref. [7] for (*) and Ref. [10] for (#).

REFERENCES

- [1] S.A. Solin, in <u>Intercalation in Layered Haterials</u>, edited by H.S. Dresselhaue (Pienum, New York, 1986), pp. 145-147.
- [2] S.A. Safran, Phys. Rev. Lett. 44, 937 (1980); see also S.A Safran, Solid St. Physics Vol. 40, p. 183, ed. by H. Ehrenrich and D. Turnbull, Academic Press (1987).
- [3] S.A. Safran, and D.R. Hamann, Phys. Rev. Lett. 42, 1410 (1979); also see S. Ohrishi and S. Sugaro, Solid St. Comm. 36, 823 (1980).
- [4] J.R. Dahn, D.C. Dahn, and R.R. Haering, Solid State Comm. 42, 179 (1980).
- [5] J.E. Fisher, and H.J. Kim, Phys. Rev. B 35, 3295 (1987).
- [6] B.R. York, S.A. Solin, N. Vada, R.H. Rayathatha, I.D. Johnson, and T.J. Pinnavaia, Solid State Comm., 54, 475 (1985).
- [7] B.R. York, and S.A. Solin, Phy. Rev. B <u>31</u>, 8206 (1985).
- [8] V. Xia, and H.F. Thorpe, Phy. Rev. A (in press).
- [9] H. Kim, W. Jin, S. Lee, T.J. Pinnaveia, S.D. Hahanti, and S.A. Solin, Phy. Rev. Lett, <u>60</u>, 2168 (1988).
- [10] G.L. Doll, and P.C. Eklund, 1987 (preprint).

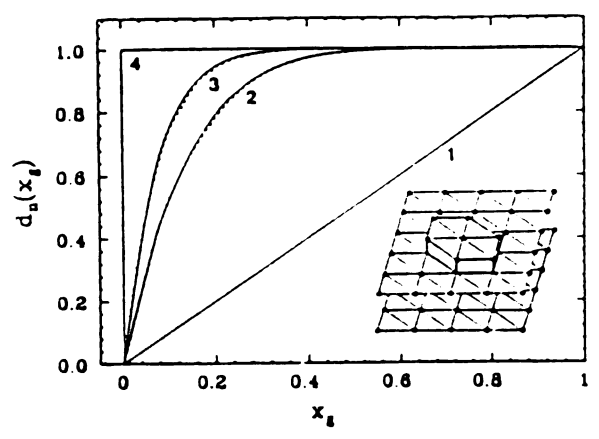
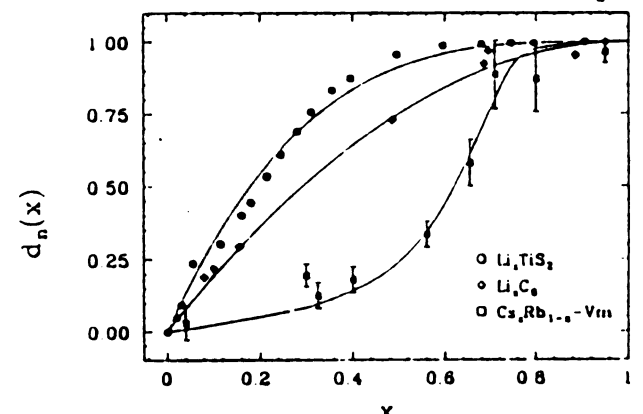


FIG. 1. Honolayer triangular lattice computer simulations (dotted lines) of the composition dependence of the normalized basal spacing of a ternary intercalation compound for several values of the healing length, λ , and rigidity parameter, P. The solid lines are from Eq. (1) of the text with (1) P=1, λ =0; (2) P=7, λ =a₀; (3) P=13, λ = $\sqrt{3}$ a₀; and (4) P==, λ ==. Inset: The puckered region of a triangular lattice with λ =a₀. Here the number of expanded sites is P=2+1=7 where 2 is the number of nearest neighbors.



 $$\rm X$$ FIG. 2. Layer rigidity model fite (see text) to basal spacing data for ${\rm Li}_{\rm x}{\rm C}_{\rm 6}, {\rm Li}_{\rm x}{\rm TIS}_{\rm 2}$ and ${\rm Cs}_{\rm x}{\rm Rb}_{\rm 1-x}{\rm -Vm}$ using P values of 2, 3.5 and 7 respectively.

FIG. 3. Interlayer correlations in layered solids: (Left panel) In floppy layers the high interlayer correlation favors a staggered position. (Right panel) In rigid layers, the interlayer correlation is negligible.

Layer Rigidity and Collective Effects in Pillared Lamellar Solids

II. Kim, (a) W. Jin, (b) S. Lee, (b) P. Zhou, (b) T. J. Pinnavaia, (a) S. D. Mahanti, (b) and S. A. Solin (b)

Center for Fundamental Materials Research, Michigan State University, East Lansing, Michigan 48824

(Received 18 November 1987)

The x dependence of the normalized basal spacing, $d_n(x)$, of pillared vermiculite (Vm) has been measured for the mixed-layer system $[(CH_1)_4N^*]_*[(CH_1)_5NH^*]_{1-\tau}$ -Vm and compared with that of $Cs_{\tau}Rb_{1-\tau}$ -Vm. Both systems exhibit a nonlinear $d_n(x)$ with approximate thresholds of $x \cong 0.2$ and 0.5, respectively. A model which related $d_n(x)$ to layer rigidity and the binding energies of gallery and defect sites yields excellent fits to the basal spacing data and to monolayer simulations if collective effects are included. This model should be applicable to other types of lamellar solids.

PACS numbers: 68.65.+g

Lamellar solids constitute a class of materials which exhibit a variety of specific properties. These properties are in large part determined by the host-layer transverse rigidity which characterizes its response to out-of-plane distortions. For example, graphite, whose monatomic amphoteric layers are "floppy" and thus collapse around intercalated guest species, does not sustain a microporous structure with large internal surface area. In contrast, layered alumino-silicate "clays," whose multiatomic fixed-charge layers are "rigid," are unique among lamellar solids in their ability to be pillared by robust intercalated guest ions which occupy specific lattice sites in the interlayer galleries. The resultant pillared clay is characterized by widely spaced host layers that are propped apart by sparsely distributed guest species whose intralayer separation can be many times their diameter. The enormous free volume of accessible interior space that is derived from such an open structure has significant practical implications in the fields of catalysis and selective adsorption (sieving).

Although it is obvious that layer rigidity and pillaring, which is a special example of the more general phenomenon of interculation, are interrelated, the pillaring mechanism has, to date, been poorly understood. For instance, none of the available elastic models account quantitatively for the full composition dependence of the the c-axis repeat distance of any intercalated layered solid.4-6 It is not surprising that the rigid-layer versions of such models fail when applied to floppy or moderately rigid hosts such as graphite' and layer dichalcogenides. But they are qualitatively inconsistent with data derived from clay hosts to which rigid-layer models should be most applicable. Accordingly, we report in this paper the first successful attempt to quantify and parametrize the relation between pillaring and layer rigidity. To accomplish this we have carried out x-ray and simulation studies of the x dependence of the basal spacing, d(x), of mixed-layer vermiculite (Vm) clays A_xB_{1-x} -Vm. $0 \le x \le 1$, where A and B are cations (assume that A is larger than B) that are judiciously chosen to elucidate the physics of pillaring. In a previous study we examined the Cs_rRb_{1-r} -Vm system for which the alkali intercalate species are best characterized as "puny" pillars since their ionic diameters are only 3.34 and 2.92 Å, respectively. Here we focus on the more robust mixed pillar system tetramethyl ammonium-trimethyl ammonium-vermiculite with effective diameters of 4.8 and 4.0 Å, respectively. We find that the pillaring process is a collective phenomenon which introduces an intrinsic nonlinearity in d(x). While our results are deduced for clay intercalation compounds (CIC's) they should also be applicable to other lamellar solids.

Vermiculite is a trioctahedral 2:1 layered silicate. Its layers are formed from a sheet of edge-connected octahedra $(M^{VI} = Mg, Al, Fe)$ which is bound to two sheets of corner-connected tetrahedra (M^{IV} =Si, Al) as shown in the inset of Fig. 1. The layers of oxygen atoms which terminate the clay layers are arranged in a kagomé lattice whose hexagonal pockets form a triangular lattice of gallery sites which here are constrained by the requirement of overall charge neutrality to be occupied by the gallery exchange cation. This occupation imposes a lateral registration of adjacent clay layers as indicated in the inset of Fig. 1. To synthesize the specimens studied here, the Mg²⁺ gallery cations which link the layers of natural Llano vermiculite were exchanged for (CH₃)₃NH + ions with ethylenediaminetetraacetate as a complexant. Subsequent exposure of pure [(CH₁)₃NH⁺]-Vm to the proper amount of (CH₃)₄N⁺ yielded a solid-solution pillared CIC

$$[(CH_3)_4N^+]_7[(CH_3)_3NH^+]_{1-7}-Vm.$$

Self-supporting sedimented films exhibited a mosaic spread of $\approx 5^{\circ}$ with the layers parallel to the substrate.

The x dependence of the (00l) x-ray diffraction patterns of $[(CH_3)_4N^+]_\tau((CH_3)_3NH^+]_{1-\tau}$ -Vm is shown in Fig. 1. The starred reflections in that figure are from a small concentration of an impurity phase whose 14.477-Å basal spacing is x independent as evidenced by the vertical line in Fig. 1. The patterns in Fig. 1 can be well accounted for by a structure-factor calculation for a 25-layer stack. We have also attempted to fit the pat-

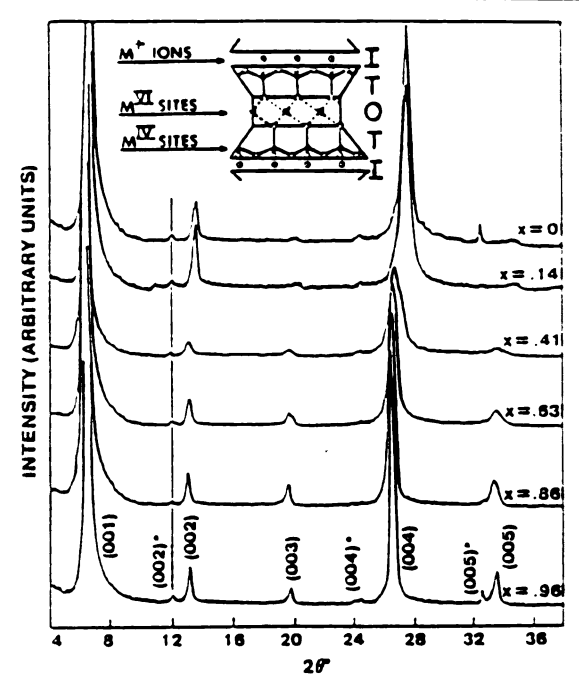


FIG. 1. Room-temperature x-ray diffraction patterns of $[(CH_1)_4N^+]_x[(CH_1)_3NH^+]_{1-x}$ -Vm excited by Cu Ka radiation (filled circles). Starred reflections are from an impurity phase. The solid vertical line shows the constant position of the (002)* reflection. Inset: Schematic structure of a 2:1 layered aluminosilicate clay with the tetrahedral (T) and octahedral (O) sheets which bound intercalated ions (1) (see text).

terns of Fig. 1 using a Hendricks-Teller (HT) model⁸ for an interstratified structure.⁷ The HT calculations yielded results which were clearly inferior to those based on a solid-solution arrangement in which all galleries have the same height. Moreover, a one-dimensional Patterson synthesis⁹ from the measured peak intensities did not show any sign of interstratification.

From the data of Fig. 1, we have determined the x dependence of the normalized basal spacing, $^6d_n(x)$ (or normalized c-axis repeat distance), of $[(CH_3)_4N^+]_{x-1}[(CH_3)_3NH^+]_{1-x}$ -Vm which is shown in Fig. 2 as filled squares. Here $d_n(x) = [d(x) - d(0)]/[d(1) - d(0)]$ where d(x) is the observed basal spacing. Also shown in Fig. 2 for comparison are corresponding results for Cs_xRb_{1-x} -Vm (Ref. 6) (open squares). Both the Cs-Rb and $(CH_3)_4N^+$ -(CH₃)₃NH⁺ systems exhibit a non-Vegard's-law (nonlinear) rapid rise in $d_n(x)$ with increasing x at "threshold" values of x_t =0.5 and 0.2, respectively.

To understand the physical origin of the observed $d_n(x)$, we have simulated a model monolayer system with finite transverse layer rigidity. For simplicity we assumed that the intercalate ions are hard spheres.

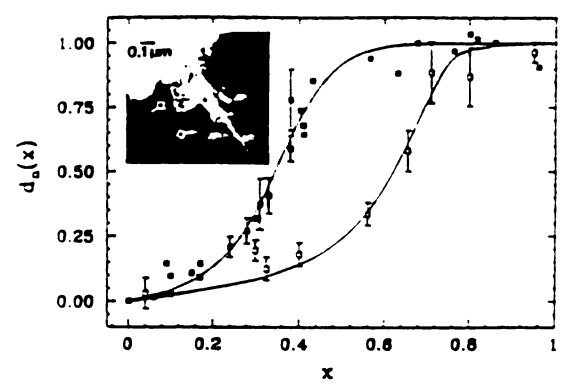


FIG. 2. The composition dependence of the normalized basal spacing of $\{(CH_3)_4N^+\}_7\{(CH_3)_3NH^+\}_{1-r}$ -Vm (filled squares) and Cs_rRb_{1-r} -Vm (open squares). The solid lines are least-squares fits to the data with Eq. (4) of the text. Inset: Bright-field scanning-tunneling electron micrograph of $(CH_3)_3NH^+$ -Vm acquired at $T=-135\,^{\circ}C$ with the electron beam normal to the layers. Note the free surface between layer edge dislocations (outline-headed arrows), the folded region (lozenges), and the microcrack (open-headed arrows). The small dotted grids are an instrumental artifact.

Starting from a two-dimensional triangular lattice of lattice constant an representing a single gallery with each lattice site occupied by a B ion of height d_B , we randomly replace the B ions with A ions of height $d_A > d_B$. The height of a cell within a healing length λ of the A ion is also increased to d_A . A second A ion in this region does not affect aiready expanded cells but expands unexpanded cells within λ of its location. The process of random replacement of the B ions continues to saturation. If we define a(x) as the fraction of cells with height d_A , then $d_n(x) = \alpha(x)$. The simulation results for $d_n(x)$ are shown in Fig. 3 for several different healing lengths. Clearly, in the floppy-layer limit $\lambda = 0$, a Vegard's-law behavior obtains whereas the initial slope $[d_n(x)]_{x=0}^{r}$ $\rightarrow \infty$ as $\lambda \rightarrow \infty$. As can be seen from Fig. 3, there is no percolation threshold even for finite λ because $d_n(x)$ depends upon all of the large ions, not only on those belonging to the infinite percolation cluster. Note that the nonlinearity in $d_n(x)$ for $\lambda > 0$ is a collective effect associated with the individual interaction between the larger ions through their distortion fields.

The sublinear x dependence and the rapid rise in $d_n(x)$ near x_t is outside the monolayer model. Several mechanisms including the relative magnitudes of host-guest and host-host interactions, interlayer correlations, and the presence of defect (d) sites can produce sublinear behavior in $d_n(x)$ but only the latter two can generate threshold effects. Since the ions of interest here are relatively incompressible we treat the guest species as hard spheres as noted above. The interlayer correlation mechanism is one in which large guest ions locally puck-

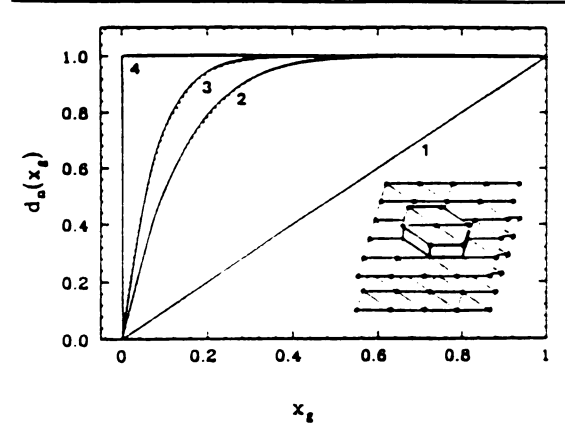


FIG. 3. Monolayer triangular lattice computer simulations (dotted lines) of the composition dependence of the normalized basal spacing of a ternary intercalation compound for several values of the healing length. λ , and rigidity parameter, p. The solid lines are from Eq. (4) of the text with (1) p=1, $\lambda=0$; (2) p=7, $\lambda=a_0$, (3) p=13, $\lambda=\sqrt{3}a_0$; and (4) $p=\infty$, $\lambda=\infty$. Inset: The puckered region of a triangular lattice with $\lambda=a_0$. Here the number of expanded sites is p=Z+1=7 where Z is the number of nearest neighbors.

er the bounding layers so that at low x they adopt staggered lateral positions, i.e., no line joining the centers of any pair of large ions in adjacent galleries is perpendicular to the silicate layer. This mechanism is relevant to host materials with low transverse layer rigidity such as graphite while the d-site mechanism is more appropriate to the more rigid layers of clays.

Sources of d sites in our specimens are shown in a scanning tunneling electron micrograph of $(CH_3)_3NH^+$ Vm (inset, Fig. 2). The region imaged consists of homogeneously intercalated areas (g sites) which are bounded laterally by layer edge dislocations and are capped by free surfaces (d sites) that bind guest species without inducing c-axis expansion. Since the clay grains have typical basal dimensions of a few micrometers, it is clear from the scale of the micrograph that these free surfaces can represent a significant fraction of the total surface available to guest species. Additional minor sources of d sites are the micrographs.

We have explored the d-site mechanism by constructing a two-site model in which the basal spacing is assumed to depend upon the gallery A-ion concentration x_g which itself is a function of the total A-ion concentration x. The functional dependence of x_g on x is determined by two parameters, f and Δ/kT , where $f = N_d/N_g$ is the fraction of ions in d sites relative to those in g sites and Δ is the effective binding-energy difference between these sites, the d sites having a lower binding energy. For simplicity we assume only one type of d site. A statistical

mechanics calculation gives

$$x_g = 1/(z+1),$$
 (1)
 $x = (1/(1+f))x_g$

$$+[f/(1+f)][1/[z\exp(-\Delta/kT)+1]],$$
 (2)

where $z = \exp[(\epsilon_g - \mu)/kT]$ is related to the fugacity and the binding energy ϵ_g of the g sites. Equations (1) and (2) can be solved to obtain $x_g = o(x, f, \Delta/kT)$ for different values of f and Δ/kT . Physically then for $x < x_t$, the A ions first preferentially displace B ions from the d sites. This reduces the gallery A-ion concentration for a given x and yields a sublinear increase in $d_n(x)$. For $x > x_t$ additionally ingested A ions enter the galleries. The result is a rapid increase in $d_n(x)$.

Using methods developed by Xia and Thorpe 10 one can obtain the following analytic solution for our monolayer simulation:

$$d_n(x_g) = 1 - (1 - x_g)^p, \quad 0 \le x_g \le 1, \tag{3}$$

where p is a layer rigidity parameter. This equation fits the simulation data extremely well as shown by the dotted lines in Fig. 3. For our lattice-gas simulation, p=Z+1 where Z is the number of neighboring sites that are puckered by the insertion of an isolated A ion (see inset Fig. 3). In the continuum limit $(\lambda \gg d_A/2)$, $p \sim (2\lambda/d_A)^2$. Using Eq. (3) and $x_g = \phi(x, f, \Delta/kT)$, we obtain

$$d_n(x) = 1 - \{1 - \phi(x, f, \Delta/kT)\}^p. \tag{4}$$

Note that the slope of $d_n(x)$ at $x \gtrsim x_t$ is governed by a combination of p and Δ/kT while x_t is determined primarily by f for large Δ/kT .

We have used Eq. (4) to obtain a nonlinear leastsquares fit to the data of Fig. 2. The parameter values which give very good fits (solid lines in Fig. 2) for the two CIC systems $[(CH_3)_4N^+]_x[(CH_3)_3NH^+]_{1-x}$ -Vm and Cs_xRb_{1-x} -Vm are $\{p=8.0, f=0.5, \Delta/kT=4.3\}$ and $\{p=7.0, f=2.2, \Delta/kT=4.1\}$, respectively. The smaller value of the rigidity parameter in the Cs-Rb system is consistent with the fact that alkali ions in CIC's can partially penetrate the bounding silicate layers. The mechanism which gives rise to this penetration is a torsional in-plane distortion 1.6 of the tetrahedral sheets which expands the hexagonal pockets that contain the guest species. Ion penetration of the clay layers causes a reduction of the apparent healing length. But the (CH₃)₄N⁺ and (CH₃)₃NH⁺ ions are much too large to penetrate the clay layer significantly, even in the presence of torsional distortions. Thus one expects the Cs-Rb-Vm system to exhibit a lower value of the rigidity parameter p. The f values deduced for the two systems also reveal interesting properties of the clay structure. For singly ionized guest species $N_j = \sigma A_j$, where σ is the layer charge density and A, is the surface area associated with j sites, j=d,g. If $A=A_d+A_g$ then $A_d=[f/(1+f)]A$ and $(A_d)_{C_1-Rb}/(A_d)_{(CH_1)_4-CH_2)_5}\cong 2$. Thus, of the surface which provides d sites for small Cs-Rb ions only about half (the portion not adjacent to edge dislocations, or derived from some microcracks or folds) can also accommodate the robust $(CH_3)_4N^+$ - $(CH_3)_4NH^+$ ions without inducing basal expansion. Finally, the difference in the Δ/kT values for the two pairs indicates that the d sites are more attractive for the larger ions. This makes physical sense because the more spatially demanding ions prefer the less constrained defect environment to the more restrictive gallery.

The layer rigidity model which we have developed here should be directly applicable to other lamellar solids such as zirconium phosphates and layered niobates which have relatively rigid lavers. It can also give insight into the behavior of intercalation compounds whose host lavers have low or moderate rigidity. For example LirC6 (Ref. 4) and LirTiS2 11 exhibit no threshold in $d_n(x)$, and therefore contain few if any d sites. Also, there are conflicting reports of a Vegard's-law $d_n(x)$ for Rb, K₁₋, C₈ prepared from single-crystal graphite 12 and a thresholdlike sublinear behavior for the same compound prepared single-crystal graphite, 13 highly oriented pyrolytic graphite, 14 or powder, 15 For clay hosts sublinear threshold behavior can be reasonably associated with d sites. But for floppy-layer hosts such as graphite there is much evidence 15 that interlayer correlations and their associated strain fields dominate the behavior. Therefore, even though the non-Vegard's-law behavior of $Rb_{\tau}K_{1-\tau}C_{R}$ (Ref. 12) has been attributed to d sites, we do not believe that the model addressed here is applicable to that compound.

Finally, we have assumed that the site binding energies in our model are independent of concentration. This assumption might be relaxed if the binding energy of the g sites drops once the galleries are initially expanded.

The resultant transfer of ions from d to g sites would then contribute to the rapid increase in $d_n(x)$ for $x \gtrsim x_i$.

We thank M. F. Thorpe for the derivation of Eq. (3). Useful discussions with H. X. Jiang and Y. B. Fan are acknowledged. This work was supported by the National Science Foundation under Materials Research Center Grant No. DMR 85-14154 and in part by the Center for Fundamental Materials Research of Michigan State University.

⁽a) Department of Chemistry.

⁽h) Department of Physics and Astronomy.

¹S. A. Solin, in *Intercalation in Layered Materials*, edited by M. S. Dresselhaus (Plenum, New York, 1986), p. 145.

²T. J. Pennavaia, Science 220, 365 (1983).

³Unlike graphite which is amphoteric, clays have a fixed layer charge. Intercalation in these materials is thus an intragallery ion-exchange process.

⁴There is one exception, K(NH₁)_xC₂₄, whose superlinear x-dependent basal spacing is qualitively distinct from that of clays but is well accounted for by a rigid-layer model which includes both elastic and electronic effects. See B. R. York and S. A. Solin, Phys. Rev. B 31, 8206 (1985).

⁵J. E. Fischer and H. J. Kim, Phys. Rev. B 35, 3295 (1987), and references therein.

⁶B. R. York et al., Solid State Commun. 54, 475 (1985).

⁷H. Kim et al., to be published.

⁸S. Hendricks and E. Teller, J. Chem. Phys. 10, 147 (1942).

⁹D. M. C. MacEwan, Nature (London) 171, 616 (1953).

¹⁰W. Xia and M. F. Thorpe, Phys. Rev. A (to be published).

¹¹J. R. Dahn, D. C. Dahn, and R. R. Haering, Solid State Commun. 42, 179 (1982).

¹²D. Medjahed, R. Merlin, and R. Clarke, Phys. Rev. B 36, 9345 (1987).

¹³P. Chow and H. Zabel, to be published.

¹⁴P. Chow and H. Zabel, Synth, Met. 7, 243 (1983).

¹⁵S. A. Solin and H. Zahel, Adv. Phys. (to be published).

From: CHEMICAL PHYSICS OF INTERCALATION
Edited by A.P. Legrand and C Flandrois
(Plenum Publishing Corporation, 1987)

LAYER RIGIDITY OF CLAY INTERCALATION COMPOUND: $[Me_{ij}N^+]_{1-x}[Me_3NH^+]_{x}-V$

S. Lee, H. Kim, S.A. Solin and T.J. Pinnavaia

Center for Fundamental Materials Research Michigan State University East Lansing, MI 48824-1116

Vermiculite is an Alumino-Silicate clays which is one of the layered materials that can form intercalation compounds [1-3]. The host layer of Vermiculite is classified as a 2:1 layered silicate due to its structure [2]. This 2:1 layered silicate is responsible for several of the distinctive properties of Vermiculite. First, unlike graphite layers which are charge neutral, 2:1 layered silicate has a negative layer charge. To compensate this the galleries of Vermiculite are occupied by cations and in turn this makes the intercalation process in CIC's (Clay Intercalation Compounds) an ion exchange process. Second, because the 2:1 silicate layers are composed of multiple, cross-linked planes of atoms, one can expect the clay layers to be relatively rigid to transverse distortions. The rigidity of the silicate layer is important not only for the study of fundamental physical properties of quasi-two dimensional systems but also for practical applications such as catalysis [4,5]. In any case, it is very important to know how rigid the layer is and what factors affect layer rigidity.

To answer the above questions we have used the following strategy. First, we prepared the ternary CIC's: $A_{1-X} B_{-V}$, $0 \le x \le 1$ with two different monovalent intercalants where the ionic radious r_A is larger than r_B . Ions A and B are randomly distributed in the gallery and the gallery height is different from that of the pristine host material. Second, we used x-ray diffraction to measure the c-axis repeat distance between two successive host layers (basal spacing). The basal spacing is in general a non-linear function of the intercalant composition x and is governed by the layer rigidity, intercalant dimensions, the difference in size and compressibility of the intercalants and the effects of inter-layer correlation.

For this study $[Me_{ij}N^{+}]_{1-x}[Me_{ij}NH^{+}]_{1-x}[Vermiculite)$ was made from Mg-Vermiculite using an ion exchange method [6], and the result was compared with the previous study of $[Cs^{+}]_{1-x}[Rb^{+}]_{1-x}[Vermiculite]$. The x-ray diffraction experiment was performed with a computer controlled Huber 4-circle diffractometer coupled to a Rigaku 12Kw rotating anode Mok α source through a vertically bent graphite monochrometer.

Department of Physics and Astronomy
Department of Chemistry

The (OOL) x-ray diffraction patterns for different compositions (x) are shown in Fig. 1 together with an insert showing a rocking curve of the (OO4) reflection. Vermiculite sample films are the mopological analog of HOPG and this rocking curve indicates a mosaic spread of ~ 5.25 which is comparable to that of graphoil [8]. From the x-ray diffraction pattern one can see many orders of peaks and these are used to determine basal spacing from a Q-plot.

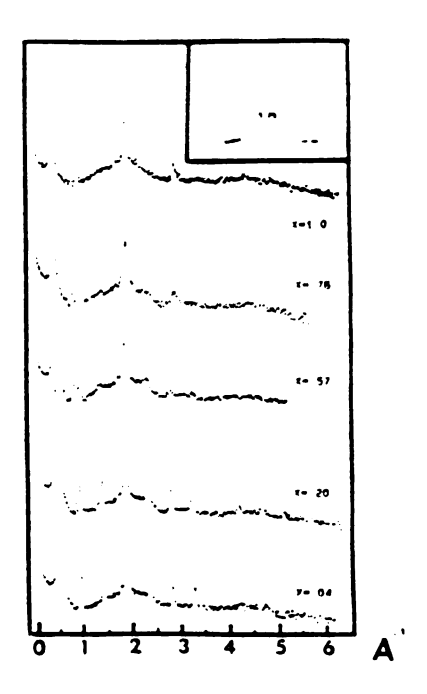


Fig. 1. X-Ray diffraction patterns of $[Me_{ij}N^{+}]_{1-x}[Me_{ij}NH^{+}]_{x}$ -V

The following discussion of the behavior of basal spacing versus composition is based on the assumption of a mixed heteroionic system, meaning ions A and B are randomly decorating a 2D Kagomé lattice in each gallery. On the other hand, it is well known that clays tend to be interstratificated which means ions A and B can segregate into different galleries in a sequence units which may be randomly stacked [1,9,10]. To make it clear which is the case, a comparison between the experimental xray diffraction patterns and the computer generated patterns is made. In generating x-ray diffraction patterns, the Lorentz-polarization factor and the layer scattering factor are considered with two different interference functions, a Bragg function and a Hendricks-Teller (HT) function [1,11]. For the Bragg interference function, 25 layers and for the HT intereference function infinite number layers are assumed. The resultant computer generated peaks based on Bragg function give a superior agreement with experimental data compared to those based on the HT function. Also no sign of basal spacings on a scale greater than 20A. characteristic of e.g. A/B/A/B stacking, has been observed. Hence one can conclude safely that the intercalants are indeed randomly distributed in the galleries.

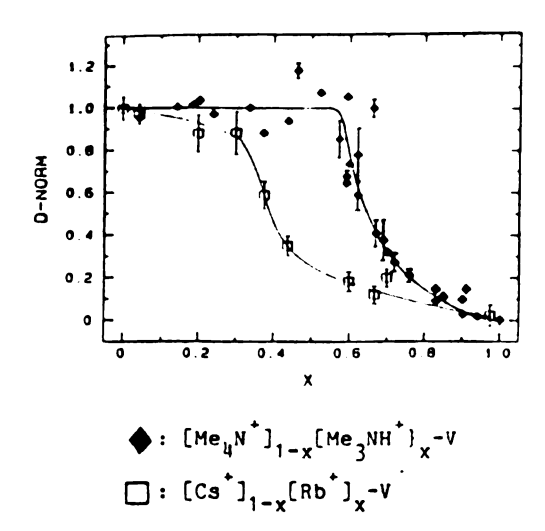


Fig. 2. Normalized basal spacing of CIC's

To compare the composition dependence of basal spacing between two different CIC's a normalized basal spacing defined as d(x) = [d(x) = d(x)]/[d(x) = d(x)/[d(x) = d(x)/[d(

To address the intercalant issue, the encapsulement parameter δ which is a measure of the degree to which the cation is enveloped by the bounding host layers [7] and the sagging limit $\Delta h_{\rm max}$ which quantifies the finite rigidity of the host layer are introduced. In Table 1, relevant parameters are listed. As one can see from the first and second columns of the table, d(M -V) increases with the height of cation M but there is a certain descrepancy between [Cs ,Rb] ions and [Me_N ,Me_NH] ions which is more vividly expressed in terms of δ in the table. In CIC's intercalants are sitting on the hexagonal pocket of an oxygene kagomé lattice and it is well known that these oxygene planes are capable of performing torsional distortions [1,7,13]. These hexagonal pockets have an undistorted size of 2.67Å and for the cations which have lateral dimensions that are less than or comparable to the pocket size these oxygene layers have a torsional distortion which increases δ . But if the cation becomes too large, the host layers cannot provide sufficient torsional distortion to accomodate them. Hence the basal spacing change from that of the pristine sample is far less sensitive to the ion size with the smaller ion set than with the larger ion set.

For finite rigidity layers we can express the sagging of the host layer from its maximum height as $\Delta h(x) = \Delta h = [1-\exp(1-L(x)/a)]$ where Δh is the sagging limit due to finite layer rigidity (i.e. for infinitely rigid layer Δh is zero), L (x) is the separation between two nearest big ions with given composition x and a is the unit length of the kagomé lattice cell. For x=0 limite (all big ion limit) we have L(0)=a and $\Delta h(x)$ becomes zero, for high x limit L>>a and Δh becomes Δh . Now compare $\Delta h(x)$ with Δr , the difference of ion radii. If $\Delta h(x)$ is smaller

TABLE 1. Relevant Parameters

	d(A)	H(A)	D(A)	5(A)	5/H(%)
[Me 4N] [Me 3NH] [Cs 3 Rb 1 Na (*)	13.34	4.2	4.8	0.20	4.76
[Me_NH]	12.70	3.2	4.0	<0	
Cs	10.57	3.38	3.38	2.15	63.6
Rb T	10.23	2.96	2.96	2.07	69.9
Na (*)	9.75	1.96	1.96	1.55	79.1

*:ref. 14

d is the basal spacing of M -V, H and D are height and diameter of cation, and encapsulement parameter is defined as $\delta = (T+H)-d$ where T=9.34(Å) is the thickness of the silicate layer. cf. D(Li)=1.36(Å) and D(Mg $^{\prime}$)=1.30(Å)

than Δr , the smaller ion does not contribute to basal spacing which will then be determined by d $_{max}$ and $\Delta h(x). If <math display="inline">\Delta h(x)$ is larger than Δr_* the layer sagging is limited by the smaller ions and the basal spacing will be affected by the presence of the smaller ions. Because $\Delta h(x)$ increases as x increases, one can expect to observe the contribution from the smaller ion at smaller x for the system which has smaller Ar. As shown in Table 1 $\Delta r[Cs^{\dagger},Rb^{\dagger}]=.42A$ and $\Delta r[Me_{\parallel}N^{\dagger},Me_{\parallel}NH^{\dagger}]=1.0A$, in addition the torsional distortion of the Kagomé lattice reduces the effective $\Delta r[Cs], Rb]$ even less than .42Å as explained in the encapsulement discussion. This is the reasons why sharp drops in basal spacing were observed near x=.4 for [Cs,Rb] system and near x=.6 for [Me,N,Me,NH] system, respectively.

ACKNOWLEDGEMENTS

Useful discussions with S. Mahanti and W. Jin are gratefully acknowledged. This work was supported by NSF-MRG Grant DMR 85-141545 and in part by the MSU Center for Fundamental Materials Research.

REFERENCES

- 1. G.W. Brindly and G. Brown (eds.): Crystal Structure of Clay Minerals and Their X-Ray Identification (Minerological Society, London, 1980).
- 2. R.E. Grim: Clay Minerology (McGraw-Hill, New York, 1968).
- 3. S.A. Solin: J. Molec. Catalysis 27, 293 (1984).
- 4. T.J. Pinnavaia: Science 220, 365 (1983)
- 5. M.S. Wittingham and A.J. Jacobson (eds.): Intercalation Chemistry Article by J.M. Thomas (Academic Press, New York, 1982).
- 6. H. Kim and T.J. Pinnavaia: unpublished.
- 7. B.R. York, S.A. Solin, N. Wada, R.H. Raythatha, I.D. Johnson, and T.J. Pinnavaia: Solid State Comm. 54 475 (1985).

 8. M.S. Dresselhaus and G. Dresselhaus: Adv. Phys. 30, 139 (1981).
- 9. D.H. Fink, F.S. Nakayama, and B.L. McNeal: Soil Sci. Soc. Amer. Proc. 35, 552 (1971).
- 10. M.B. McBride and M.M. Mortland: Clays and Clay Minerals 21, 323 (1973).
- 11. S.B. Hendricks and E. Teller: J. Chem. Phys. 10, 147 (1942).
- 12. M.S. Dresselhaus (ed.): Intercalation in Layered Materials, NATO ASI Series 148, Article by S.A. Solin (Plenum Press, New York, 1986).
- 13. M. Ishii, T. Shimanouchi, and M. Nakahirs: Inorganica Chimica Acta /1:3/, 387 (1967).
- 14. D.R. Hines, N. Wada, and M. Suzuki: Bull. Am. Phys. Soc. 32, 559 (1987).

